NEW ZEALAND IRONSANDS CATALYSIS OF THERMO-CATALYTIC METHANE DECOMPOSITION

A thesis presented for the degree of
Master of Science
in
Nanoscience
at Massey University, Palmerston North,
New Zealand

Samuel Thomas Powick

School of Fundamental Sciences
2020

Abstract

The use of hydrogen gas as an energy carrier is a proposed pathway to eliminating greenhouse gas emissions from fossil fuels. However, emissions-free production of hydrogen is more costly than traditional high-emissions hydrogen production processes such as Steam Methane Reformation (SMR). To address this, a process called Thermo-catalytic Methane Decomposition (TCMD) is being commercially developed. This process uses methane (natural gas) to produce hydrogen gas and high quality solid carbon which can be sold to offset the price of the hydrogen produced. TCMD has the potential to be cost-competitive with SMR. A key feedstock in the TCMD process is a low cost catalyst, because the carbon produced deposits on the catalyst and deactivates it. The most commercially viable choice of catalyst has been identified as iron ore, or hematite, due to its high activity and lifetime, and its low cost [13, 23]. The TCMD process could have applications in New Zealand to supply the heavy transport market, but for this to happen, a domestic source of iron ore is required for use as a catalyst. New Zealand's primary source of iron ore is in the form of titanomagnetite found in ironsands, which has different properties to hematite. As a result, this research was commissioned to evaluate the effectiveness of New Zealand ironsands as a catalyst for TCMD. The effects of temperature, flow rate, catalyst composition, and aggregate particle size on ironsand catalytic activity, lifetime, and carbon by-product quality are evaluated relative to a hematite control.

Contents

Acknowledgements

Thank you to my supervisors: Prof. Richard Haverkamp, and Assoc. Prof. Mark Waterland for reviewing this late at night while Mrs Waterland watches Grey's Anatomy without him in the next room. Also, thanks to the funding partners that made this research possible: The Energy Education Trust of NZ, and Hiringa Energy. Andrew and Cathy, thanks for continually seeing potential in me and giving me opportunities to work on things that I'm excited about.

Steve, Olaf, and Stan, thanks for a five star workshop experience and for the complimentary life advice. John Sykes and John Edwards, thanks for the consistent and patient help with instruments and fittings. Thank you to all the staff and other post-grads in the School of Fundamental Sciences, particularly Prof. Shane Telfer and his group, who trained me and let me loose on their instruments. Sam Brooke and Robert McEwen, cheers for being the motivation I needed to finish this, despite your best efforts.

Thanks to all my friends and family, for your unending encouragement and confidence in me. And lastly, thank you Hannah, for being incredibly supportive while I wrote this thing instead of helping with the wedding. I couldn't have made it this far without you. I'm done now.

Nomenclature

$\beta_{\frac{1}{2}}$	Width of the PXRD diffraction peak at FWHM
λ	Wavelength of X-ray radiation used in PXRD
θ	Bragg angle
$g_C/g_{catalyst}$	Weight of carbon in grams per weight of catalyst used in the experiment
g_C/g_{Fe}	Weight of carbon in grams per weight of iron
ATR	Auto-Thermal Reforming
Avg PD	Average particle diameter, also d_c
BEV	Battery Electric Vehicle
CCM	Crackling Core Model
Cementite	Fe_3C, also iron carbide
CSM	Cracking Shrinking Model
d	Interplane distance of graphite (002) plane
d_c	Average particle diameter, also Avg PD
FCEV	Fuel Cell Electric Vehicle
Ferrite	α-Fe, the form of iron that is catalytically active for TCMD
FWHM	Full Width Half Maximum
G	Glenbrook ironsand

g	Fractional degree of graphitisation, also GD
GC	Gas Chromatography
GD	Fractional degree of graphitisation, also g
H	Hematite control
HFCEV	Hydrogen Fuel Cell Electric Vehicle
I	Patea ironsand, unpurified
I_D/I_G	Ratio of the intensity of the D peak and the G peak in the graphite Raman spectrum. Used as a measure of carbon disorder.
IP	Magnetically purified Patea Ironsand
Iron Carbide	Fe_3C, also cementite
k	Scherrer coefficient
K_T	Equilibrium constant of the reaction at temperature T
LOI	Loss On Ignition
N	Sample size
POX	Partial Oxidation
PSA	Pressure Swing Adsorption
PSD	Particle Size Distribution
PXRD	Powder X-Ray Diffraction
Q	Quartz Tube

Rt	Retention Time
S	Stainless steel tube
SCA_t	Sustained Conversion Average over t hour(s) from the point of maximum conversion
SCD	Surface Carbide Deposition
SCM	Shrinking Core Model
SG	Specific Gravity
SMR	Steam Methane Reformation
$t_{\frac{1}{2}max}-t_{max}$	Time taken for the conversion ratio to decay from maximum to half maximum
t_{max}	Time at which the maximum conversion ratio occurs during an experiment
TCMD	Thermo-catalytic Methane Decomposition
TEL	Thermodynamic Equilibrium Limit
TGA	Thermo-Gravimetric Analysis
TGA Half-temp	The temperature at which a TGA sample loses half its mass
vol%	Volume percentage
X_{CH_4}	Conversion of methane (%)
XRF	X-Ray Fluorescence

List of Figures

List of Tables

1 Introduction

In 2017, as a consequence of greenhouse gas emissions from human activities, the average global temperature was between 0.8 and 1.2°C higher than pre-industrial levels. Between 2030 and 2052, this is likely to increase to 1.5°C, and then, if no action is taken, to 2°C. The risks to humanity and the environment are thought to be significantly higher at 2°C of global warming than at 1.5°C. Because of this, an urgent and concerted international response is required to reduce our emissions [26].

The 2016 Paris agreement aims to motivate this global response through national policy commitments. To date, 184 countries have ratified the agreement, including New Zealand, however the national commitments of each country vary widely and are currently overwhelmingly insufficient to restrain projected temperature increases. New Zealand's current policies are rated as 'insufficient' to meet its fair share of emissions reductions [11]. As part of the Paris agreement, New Zealand has committed to reducing net greenhouse gas emissions by 2030 to 11% below what they were in 1990, and in 2019, the government introduced a target of zero net emissions by 2050 (with a caveat for agricultural methane). Meeting these targets will require particular action in the agriculture, energy, and transportation sectors. Other than agriculture, energy and transportation are the largest sources of emissions in New Zealand, together contributing 39.8% of our total emissions in 2016 [34]. Almost half of emissions within the energy & transportation combined sector are from road transportation emissions, which have increased by 82.1% since 1990.

A significant reduction in the use of fossil fuels for transportation is required if New Zealand is to keep pace with the rest of the world. Eleven countries have announced bans on new internal combustion vehicles to reduce transport emissions, including Norway by 2025, Denmark and Sweden

by 2030, and France and Britain by 2040 [4]. As a result, vehicle manufacturers are moving towards the production of electric drive vehicles, in the form of either Battery Electric Vehicles (BEVs) or Fuel Cell Electric Vehicles (FCEVs). BEVs are powered by batteries charged from the electricity grid, and have the potential to be carbon-neutral if the electricity used to power them is produced sustainably from hydro-, wind, or solar power. Hydrogen FCEVs (HFCEVs) are powered by fuel cells that convert hydrogen from an on-board tank into electricity that is fed to the electric drive. HFCEVs also have the potential to be carbon-neutral if the hydrogen fuel is produced by renewable means. Manufacturers such as Nissan, Volvo, and Ford are developing BEVs, while hydrogen FCEVs are being developed by Toyota, Hyundai, and Honda.

Globally, there has been higher uptake of BEVs than HFCEVs, for two reasons. Firstly, less capital expenditure is required to run small numbers of BEVs, because they can be supported by existing electrical infrastructure that does not rely on economies of scale. HFCEVs require hydrogen production infrastructure, as well as a network of hydrogen fueling stations, which carry with them a high capital cost that has forced a high price of hydrogen at the pump in cities where this infrastructure has been built. Secondly, the price of BEVs has been lower than HFCEVs, in part due to the fact that the development of FCEVs is several years behind that of BEVs. However, particularly in a New Zealand context, HFCEVs have important advantages over BEVs. For instance, in New Zealand, most freight is transported by high-emissions diesel-fuelled trucking [34]. Heavy vehicles made up 3.7% of all vehicles in New Zealand in 2016, but contributed 25.5% of vehicle emissions that year [36], so this is an important area to target for emissions reductions. However, for heavy transport and long range applications, BEVs are limited by the cost and weight of additional battery capacity, while hydrogen tanks can simply be made larger to increase the range of the vehicle, without un-

due weight penalty. This is because hydrogen has a specific energy of 33.3 kWh/kg, compared to around 0.55 kWh/kg for Li-ion batteries [17].

In addition to fuelling trucks, hydrogen also has possible applications in marine transport, such as fuel-cell powered ferries, stationary power generation, such as the use of fuel cells as emergency power sources in remote areas, and trains. In the long term, a hydrogen-based economy could facilitate international trade of renewable energy through the export of renewably-produced hydrogen to countries such as Japan.

While in its infancy, the development of hydrogen production and fuelling infrastructure in New Zealand is gaining traction. In 2019, the New Zealand government released its vision statement for hydrogen development, stating that developing hydrogen will be a part of its upcoming renewables strategy [35]. In addition, projects by Ports of Auckland, Hiringa Energy, and Tuaropaki Trust are currently in progress to build hydrogen production and fuelling infrastructure, with varying levels of support from the government.

A significant challenge that these projects face is that emissions-free hydrogen is more expensive to produce than hydrogen produced with traditional methods. The most cost effective method for producing hydrogen is Steam Methane Reformation (SMR), which produces 95% of hydrogen in the United States and around 50% of hydrogen globally [44]. SMR produces hydrogen from methane in the presence of a nickel catalyst according to the following process:

$$\mathrm{CH_4\,(g) + H_2O\,(g)} \rightleftharpoons \mathrm{3\,H_2\,(g) + CO\,(g)}$$

$$\mathrm{CO\,(g) + H_2O\,(g)} \rightleftharpoons \mathrm{H_2\,(g) + CO_2\,(g)}$$

Across the entire process, SMR produces 0.43 mol CO_2 per mol H_2, and the overall Global Warming Potential of SMR has been estimated at 13.7 kg CO_2e per kg H_2 [39]. In comparison, a standard light vehicle emits 2.31 kg of CO_2 per kg of hydrocarbon fuel [46], and although this does not take

into account the other greenhouse gases associated with the production and use of hydrocarbon fuels, it is clear that using SMR to produce hydrogen for use as an alternative fuel is not a viable option from an emissions reduction point-of-view.

Instead, there exists an inherently cleaner process called Thermo-Catalytic Methane Decomposition (TCMD). At high temperatures and in the presence of a catalyst, methane gas decomposes into hydrogen gas and solid elemental carbon via the following scheme:

$$\mathrm{CH_4\,(g)} \quad \rightleftharpoons \quad \mathrm{2\,H_2\,(g) + C\,(s)}$$

This process still uses a fossil fuel as a feedstock, but it produces no greenhouse gases. Hazer Group, an Australian company, are in the pilot stage of commercialising a process based on TCMD, using iron ore as a catalyst. Along with being almost emissions-free, they claim to have two competitve advantages over SMR: Firstly, iron ore is significantly cheaper than the nickel catalyst used in SMR, and secondly, the carbon produced is high quality graphite that can be sold to offset the cost of hydrogen production [15, 57, 58]. Because of this, they project a 75% reduction in commodity costs over SMR, and 6 times the production rate and half the running costs of electrolysis [24].

In order to adopt TCMD in New Zealand, there are two things that must be considered. Firstly, there is uncertainty about the future of natural gas (methane) in Taranaki. In April 2018, the government banned new offshore oil and gas exploration permits, and will restrict on-shore exploration by 2021 [55]. The current natural gas reserves of Taranaki have a limited lifetime, with only about 10 years of production left, and a projected shortfall beginning this year without further development [12]. The lifetime of gas reserves doubles to 20 years with the development of reserves that are cur-

rently considered non-commercial - that is, the current gas demand means it would be un-economical to invest in expanding the gas supply. As the supply of gas decreases and the shortfall becomes apparent, this investment will happen organically. In the mid to long term, methanol production, a key source of demand, will gradually exit the market, extending the lifetime of existing reserves and leaving them available for higher value use cases. Unfortunately, this means that a new source of demand for natural gas that requires capital expenditure, such as a commercial TCMD operation, would be unable to compete with the existing petrochemical gas users that have sunk costs in existing infrastructure. Even with drastic policy changes and a high carbon price, new demand development of TCMD is unlikely to be economical [12]. The two exceptions to this are if there is a major new gas discovery in an existing field in the near future, or if the TCMD process is tied to a major biogas development. Ecogas in Rotorua has been awarded funds from the government to build an anaerobic digestion plant that would produce methane of a quantity useful for TCMD [54].

Secondly, for TCMD to be cost effective in New Zealand, it requires a source of iron oxide to use as a catalyst. The country's only domestic source of iron oxide is from ironsands, found on the west coast of the North Island. However, titanium is present in the sand in the form of titanomagnetite, $TiFe_3O_4$. Early steel manufacturers attempted to smelt the ironsands to produce iron, but the titanium in the sand prevented the use of a normal blast furnace. Instead, a new electric smelting method was successfully developed to reduce the titanomagnetite, and today over 2 million tonnes of ironsand is mined each year [45]. While the presence of titanium caused difficulties in the steel smelting process, the effect it may have on catalysis is unknown. Ironsands may perform differently to typical iron oxides when used as a catalyst for TCMD.

Hiringa Energy have commissioned this research to determine if New

Zealand ironsands could be commercially viable as a thermo-catalytic methane decomposition catalyst. It aims to understand the conditions necessary to promote the best catalytic performance of the ironsands.

1.1 Project Aims

The project aims were as follows:

1. Investigate the use of titanomagnetite (iron sands) as a catalyst for methane cracking to hydrogen and graphite and its effect on hydrogen and graphite production efficiency and quality.
2. Compare the results of the research with the control process utilising iron ore hematite catalyst Fe_2O_3.
3. Gain process knowledge in the application of iron ore catalysis in the production of hydrogen and graphite.

Its desired outcome was to successfully develop an environment in which the methane cracking catalytic performance of titanomagnetite (iron sands) is equal to that of iron ore. The environment encompassed reactor design, reaction conditions, and catalyst pre-treatment. Catalytic performance encompassed hydrogen yield, hydrogen purity, carbon yield, carbon quality, and catalyst lifetime.

These project aims were developed in conjunction with Hiringa Energy and the New Zealand Energy Education Trust, and could not easily be altered. In particular, the requirement to compare ironsand with the hematite control seemed sensible at the start of the project, because raw hematite was identified in the literature as the most commercially viable catalyst, and was actively being commercialised in Australia. However, this comparison was time consuming, and in hindsight ended up constraining other potentially beneficial avenues of investigation, such as characterising the structural changes in ironsands during TCMD.

2 Background

A review of the literature related to thermo-catalytic methane decomposition using ironsands is presented here, beginning with an overview of traditional methods for hydrogen production from methane, then covering specific detail relevant to the project.

2.1 Hydrogen Production from Methane

Methane is the most common feedstock for production of molecular hydrogen. It is favoured over other hydrocarbons because it has the highest ratio of hydrogen to carbon in its chemical composition, and because it is the most abundant fossil fuel. There are three established methods for producing hydrogen from methane: Steam Reformation, Partial Oxidation, and Autothermal Reformation.

2.1.1 Steam Reformation

Steam methane reformation (SMR) occurs via the following scheme:

$$\mathrm{CH_4\,(g) + H_2O\,(g)} \rightleftharpoons \mathrm{3\,H_2\,(g) + CO\,(g)} \tag{1}$$

$$\mathrm{CO\,(g) + H_2O\,(g)} \rightleftharpoons \mathrm{H_2\,(g) + CO_2\,(g)} \tag{2}$$

The cracking step is highly endothermic, with an enthalpy of $\Delta h_0 = 206$ kJ/mol, while the Water Gas Shift step is mildly exothermic with an enthalpy of $\Delta h_0 = -41.1$ kJ/mol. The total reaction,

$$\mathrm{CH_4\,(g) + 2\,H_2O\,(g)} \rightleftharpoons \mathrm{4\,H_2\,(g) + CO_2\,(g)} \tag{3}$$

Figure 1: A simplified schematic of the steam methane reformation process. Desulfurisation prevents sulfur compounds in the natural gas stream from poisoning the nickel catalyst inside the reformer. The reformer reacts the methane with steam to produce H_2 and CO. Heat recovery refers to the recirculation of unconverted methane back into the burner to produce steam. Next, the water gas shift reaction converts the CO from the reformer into additional H_2 using more steam. The pressure swing adsorption (PSA) system is used to separate the H_2 product from CO_2 and any other gases present in the exit stream. [44]

has an enthalpy of $\Delta h_0 = 165\ kJ/mol$ [13]. 4 moles of hydrogen and 1 mole of carbon dioxide are produced per mole of methane. The reaction occurs over a metal catalyst, normally nickel based. Figure 1 shows the standard SMR process. First, there is typically a desulfurisation step before the feed gas reaches the reforming reactor, because nickel is easily poisoned by sulfuric compounds. The methane then flows through the reforming chamber, where it is mixed with steam, heated to 850 °C and undergoes cracking according to Equation 1. The resulting methane/hydrogen/carbon monoxide mixture is cooled before reacting with more steam according to Equation 2. Finally, the exit gas stream, a mixture of hydrogen, methane, and carbon dioxide, is separated using a pressure swing adsorption system (PSA). The hydrogen produced is between 97% and 99.99% pure, and the overall conversion efficiency is between 74% and 85%. The cost to produce hydrogen from

large-scale SMR was around $2.1 USD/kg in the USA in 2019. [44, 27].

Stoichiometrically, SMR produces 5.5kg of CO_2 per kg of H_2, but the overall Global Warming Potential of the process is estimated at 13.7 kg CO_2e per kg H_2 [39].

2.1.2 Partial Oxidation and Autothermal Reformation

Partial oxidation (POX) reacts methane with oxygen according to the following scheme:

$$\mathrm{CH_4\,(g) + 0.5\,O_2\,(g)} \quad \rightleftharpoons \quad \mathrm{2\,H_2 + CO} \tag{4}$$

This has an enthalpy of $\Delta h_0 = -36\ kJ/mol$ [9], although the enthalpy of reaction changes depending on the ratio of oxygen to methane, as shown in Figure 2. The reaction becomes more exothermic as higher ratios of oxygen are added [43].

Autothermal reforming (ATR) adds a water gas shift reaction to the partial oxidation process as for SMR, giving an overall reaction of:

$$\mathrm{CH_4\,(g) + H_2O + 0.5\,O_2\,(g)} \quad \rightleftharpoons \quad \mathrm{3\,H_2 + CO_2} \tag{5}$$

This has a total enthalpy of $\Delta h_0 = -77\ kJ/mol$, and is self-sustaining. Because of this, no methane recirculation is required for heat recovery in the process, and the cost of hydrogen produced by large-scale autothermal reformation is cheaper than SMR at around $1.5 USD/kg [44]. However, there are very large capital costs associated with oxygen injection, and so this method is less favoured than SMR [13]. In addition, stoichiometrically, ATR produces 7.7 kg CO_2 per kg of H_2, more than SMR.

Figure 2: Methane decomposition reactions have a near-linear decrease in enthalpy with increasing ratio of oxygen to methane [43]. This means that large-scale process that use oxygen, such as partial oxidation or autothermal reformation, have lower energy requirements than processes without, such as SMR.

2.2 Thermo-Catalytic Decomposition of Methane

The cracking of methane into hydrogen and solid carbon has been present in the literature for a century. It was first patented in 1918, using a simple airless chamber heated to 1100 °C, and included designs for recirculated hydrogen to heat the furnace [8].

The thermal decomposition of methane into hydrogen and carbon proceeds according to the following scheme:

$$\mathrm{CH_4\,(g)} \quad \rightleftharpoons \quad \mathrm{2\,H_2\,(g) + C\,(s)} \tag{6}$$

This reaction is mildly endothermic, with an enthalpy of Δh_0 =74.85 kJ/mol [1]. This equates to 37.8 kJ/mol of H_2, compared with 41.3 kJ/mol

H_2 for Steam Methane Reformation. Equation 7 shows the Gibbs energy relationship dependence on temperature for TCMD:

$$\Delta G_0(J/mol) = 89658.88 - 102.27 \cdot T - 0.00428 \cdot T^2 - \frac{2499358.99}{T} \qquad (7)$$

The Gibbs energy is negative when T > 545 °C, meaning that theoretically methane decomposition should occur above this temperature [1]. However, to achieve an efficient hydrogen conversion rate, the temperature required is over 1200 °C [2]. To increase the conversion efficiency at lower temperatures, a metal or carbon-based catalyst is usually used.

There are no CO_2 emissions inherent in the TCMD process if the heating method is decarbonised by using hydrogen as fuel for combustion. As a result, TCMD offers complete emissions reductions over SMR and ATR for hydrogen production, which will increase its commercial competitiveness as those established processes are forced to reduce their emissions through methods such as carbon capture and storage (CCS) - something that is already happening. For example, H21 in the UK are developing a plan to decarbonise their reticulated natural gas network using an ATR process with CO_2 sequestration, beginning conversion in 2022 [20]. Figure 3 shows the H_2 and CO_2 production efficiencies per unit of CH_4 feedstock, with and without CO_2 capture and storage. It shows that TCMD is the only process than can produce hydrogen with zero emissions.

Additionally, the carbon product from TCMD has significant value and a large worldwide market, depending on the quality produced. TCMD can produce carbon nanotubes, carbon nanofibres, and other forms of high-quality graphite which are used in lithium-ion batteries and have a wide variety of potential uses, including in fuel cells [29]. A recent sharemarket evaluation of Hazer Group TCMD-produced high-purity graphite gave a projected price of US$10,000/tonne in 2021 [15].

Figure 3: H_2:CH_4 and CO_2:CH_4 production volume ratios of various processes, with and without CO_2 emissions-mitigation measures [41]. While CO_2 sequestration has the potential to reduce emissions from SMR and POX processes substantially, TCMD is the only process that can reach zero emissions. Plasma Decomposition produces no emissions, but uses large amounts of electricity which must be accounted for.

Overall, the economical viability of TCMD as a commercial process depends on the following factors:

1. Energy efficiency of the process
2. Heating method used
3. Cost effectiveness of the catalyst
4. Value of carbon product
5. Cost of regulatory requirements placed on existing SMR processes, such as CO_2 sequestration costs.

Factor (1) is favourable for TCMD due to its lower enthalpy, (5) will become increasingly favourable for TCMD as governments experience pressure to reduce emissions, and the remaining factors are all currently being researched. This research focuses on (3) and (4).

2.2.1 The Catalyst

Use of catalysts to lower the reaction temperature of TCMD and increase the rate of decomposition has been the subject of much research, as they are considered necessary for the process to be economically viable. By extension, the cost-effectiveness of the catalyst itself has a large influence on this process viability. The critical factors that determine whether a catalyst is cost-effective are:

1. Activity
2. Lifetime
3. Quality of carbon produced

Of these, the lifetime of the catalyst is the most challenging to address, because the carbon produced in the reaction deposits on the surface of the catalyst, deactivating it.

Characteristics which influence the above critical factors include:

1. Chemical composition
2. Stability and mechanical properties
3. Surface area
4. Pre-treatment
5. Particle size

For a given catalyst, the last three characteristics are variables that may be altered to influence its performance.

Catalysts for TCMD can be divided into two groups: metallic and carbonaceous. The relevance of carbon-based catalysts to this research is limited, and comes mostly from the possibility of TCMD-deposited carbon itself contributing to the reaction by catalysing further methane decomposition. As such, they will be discussed here only briefly.

Carbon-based catalysts have the advantages of being low-cost, stable, and potentially self-sustaining within a TCMD environment. Many types of

carbon have been investigated, including amorphous carbon, carbon black, graphite, and highly ordered morphologies such as carbon nanotubes and fullerenes. It was found that nanostructured carbon had low catalytic activity, but fullerene soot had high activity [3]. In general, more disordered carbon catalysts had higher activities than ordered forms [40]. Smaller particle sizes correlated with higher methane conversion rates, but over longer reaction times, partial catalyst deactivation negated this effect. Temperatures over 850 °C caused the carbon particle size to decrease, resulting in slower deactivation of the catalyst relative to lower temperatures [3]. Higher temperatures also increased the rate of methane decomposition by increasing diffusion into the smaller pores of the carbon bulk, allowing the methane to access more catalyst surface area than at lower temperatures. Catalyst lifetime was limited by deposited carbon fibre growth blocking pores, and this process occurred much more rapidly in the initial stages of a reaction. In one case, carbon deposits weighing less than a quarter of the total catalyst body caused a 97% reduction in catalyst surface area [37]. This occurs early in the reaction period (within 1-4 hrs), with the surface area vs time curve following the methane conversion curve in a $\frac{1}{x}$-like relationship [3].

Metal catalysts typically have higher activities than carbonaceous catalysts, depending on the metal used. One proposed hierarchy of metal catalyst activities for TCMD is Co, Ru, Ni, Rh > Pt, Re, Ir > Pd, Cu, W, Fe, Mo, although other reports claim the highest activities for Ni and Fe/Al combinations, with activities as high as 491 $g_C/g_{Catalyst}$ [3]. Other metals are sometimes used as promoters to improve the properties of a catalyst and balance the deposition and diffusion rates. A multi-metallic Ni+Pd catalyst on an Al_2O_3 support produced a record yield of 1498 g_C/g_{Ni+Pd} [47].

Metal catalyst deactivation occurs by carbon encapsulation and poisoning. Encapsulation with solid carbon deactivates the catalyst simply by preventing additional methane from accessing the catalyst surface. This is also

affected indirectly by sintering - structural changes in the catalyst particles themselves during the reaction, which produce more encapsulating types of carbon and increase the rate of carbon encapsulation. For example, Ni has a high activity and produces carbon fibres at temperatures below 700 °C, but above this temperature the catalyst sinters, loses surface area, and rapidly deactivates [3]. This can be prevented by supporting the catalyst particles on an inert material, so they cannot coalesce.

Poisoning deactivates the catalyst via foreign compounds binding to active sites, lowering its activity. Sulfur in the methane feedstock is the most common cause of poisoning, and is the reason that the SMR process typically includes an initial desulfurisation step.

To extend the catalyst lifetime, there are two approaches: remove the carbon from the catalyst, and slow the rate of deactivation. Separating the carbon from the catalyst is challenging because the method used must be compatible with a continuous operation of the process, as would be used in a large-scale commercial facility. Carbon can be separated using off-stream methods such as acid washing or sonication, however this can damage the catalyst and makes the continuous operation of the process difficult, especially if the catalyst has a high cost and must be recycled. The deactivation rate can be slowed by adding small amounts of water vapour, which helps by removing carbon nanoonions and other encapsulating carbon types, but carries a risk of lower carbon yields. Injecting oxidising gases like O_2, CO_2, or steam into the process can be used to remove the carbon from the catalyst particles, however, doing so produces CO_2 emissions similar to those produced by SMR, thus rendering the excercise pointless from an environmental perspective. It also degrades the carbon product, and to a varying extent, the catalyst [13], while contaminating the hydrogen exit gas stream with carbon oxides, requiring more purification [3].

2.2.2 Metal Catalyst Reaction Mechanism

TCMD follows a four step mechanism, shown in Figure 4:

1. Surface reactions
2. Dissolution
3. Diffusion
4. Precipitation

Firstly, methane adsorbs to the surface of the catalyst particle. An indicator of the rate of adsorption is the sticking coefficient (the ratio of adsorbing atoms to atoms that hit the surface in a given time) of methane for a given catalyst type. The metal used affects the orbital interactions with the depositing graphite and thus which face of the catalyst the carbon structures will deposit or grow on, and different faces of a catalyst may have different sticking coefficients [29]. For example, the Ni(1 1 0) face is the most reactive towards methane and forms the gas/metal interface, while the Ni(1 1 1) face is the least reactive towards methane and forms the metal/graphite interface [61]. Adsorption is also governed by the activation energy of methane adsorption to the catalyst [29].

Secondly, the methane is dehydrogenated repeatedly until the carbon dissolves into the catalyst crystal structure. This is thought to be the rate limiting step at temperatures between 740 and 770 °C.

Thirdly, the concentration gradient of carbon inside the catalyst particle drives the diffusion of the carbon to the other sides of the particle. This continues until the catalyst particle has become supersaturated with carbon. When Fe is the catalyst, an iron carbide (Fe_3C) phase is present, but this is not observed with Ni. However, the activities of metal catalysts, including Ni, have been shown to correlate with its carbon solubility [29]. For Fe nanoparticles formed from ferrocene, the diffusion step was the rate limiting step at temperatures between 762 and 830 °C [21].

Lastly, the carbon precipitates from the surface in different morphologies [13].

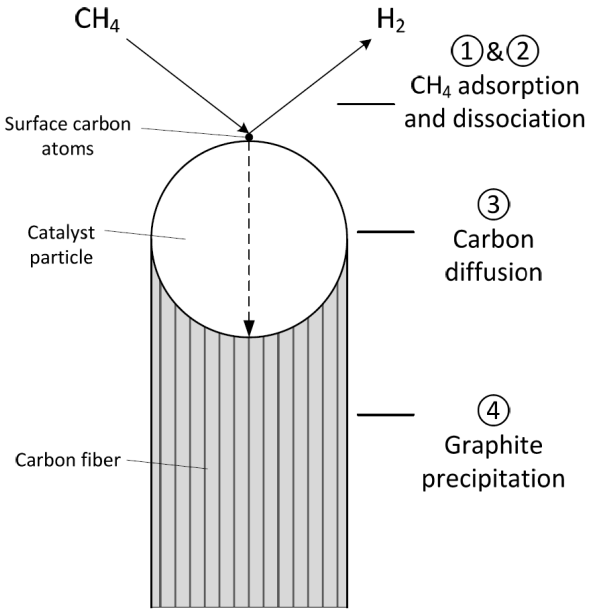

Figure 4: The four stage reaction mechanism of TCMD on a metal catalyst. Reproduced with permission from A. Cornejo [13].

Parameters of the reaction that may affect the activity, lifetime, and carbon production quality of a metal catalyst include:

1. Temperature
2. Pressure
3. Flow rate
4. Feed gas composition

These parameters must be balanced to provide conditions that allow the sustained growth of carbon fibres. This is because the rate at which carbon deposits on the surface of the catalyst and the rate at which carbon diffuses through the catalyst particles to form fibres must be balanced to prevent carbon encapsulation by structures such as carbon nanoonions. If the carbon

deposition rate is higher than the diffusion rate, the catalyst particle will be coated in carbon before it can diffuse away, and deactivation will occur. This will also cause termination of fibre growth, resulting in amorphous carbon morphologies that further encapsulate the catalyst. If, however, there is not enough carbon supplied to the catalyst, nucleation of carbon fibres will not occur [13].

Parameters can be chosen to delay deactivation by promoting metal dusting of the catalyst particles. Metal dusting is when carbon layers precipitating from the catalyst particles cause the metal to be separated from the bulk, as shown in Figure 5. This process allows the feed gas to access new surfaces of catalyst, extending the reaction lifetime. Increasing the pressure increases metal dusting. If metal dusting is high, it reduces the effect of having large catalyst particle aggregate sizes at the start of the reaction, as eventually the aggregates disperse [13].

Another factor shown to be important in the growth of carbon fibres is the curvature of the catalyst particle surface. This means that carbon fibre nucleation and growth favours smaller particle sizes. In one example, carbon fibres grew preferentially on Co catalyst particles of 10-30 nm diameter, while ignoring any larger particles [56]. Having said that, it was also observed that the metal catalyst particle morphology changed along with the type of carbon produced, moving from dense, rigid polyhedrons at low temperatures to an elongated, liquid-like state at higher temperatures [29]. This partial liquefaction increased the surface curvature of the catalyst particles, allowing carbon fibre growth on larger particles. This occurs below the normal melting point of the metal because the carbon fibre formation is exothermic [13].

A wide range of carbon morphologies have been observed as TCMD products, including single- and multi-walled carbon nanotubes, carbon nanofibres, and carbon nanoonions as shown in Figure 6. These morphologies are influenced by the reaction parameters above, along with the changes in shape of

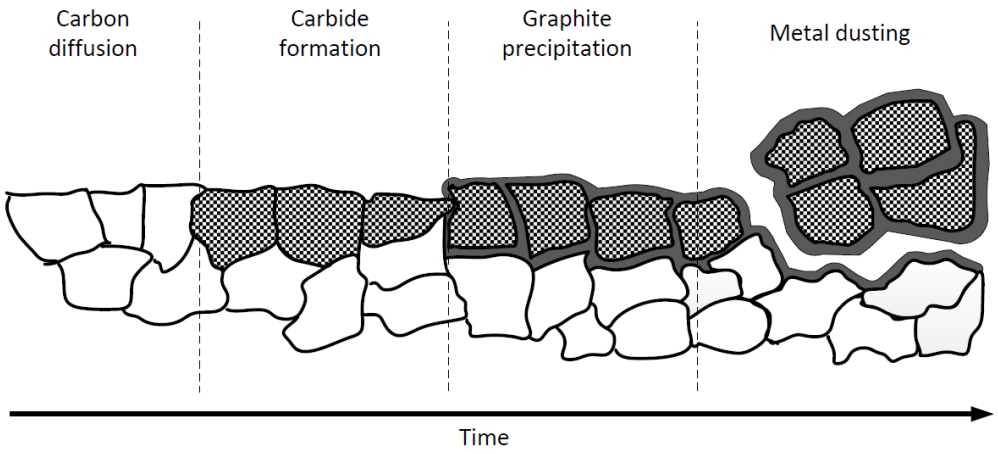

Figure 5: Schematic of metal dusting observed in TCMD. An unsupported metal catalyst, as might be used in a fixed bed reactor, initially only contacts the feed gas on one surface. As the carbon saturates the metal and begins to precipitate, the metal particle is forced away from the bulk by the graphite layer, opening up more catalytic surfaces for the methane to contact, and prolonging the reaction. *EmendationsChange1.5*Reproduced with permission from A. Cornejo [13].

the quasi-liquid catalyst particle. For example, the catalyst particle shape changes from templating the nucleation cap to templating the wall growth of a carbon nanotube [25]. This can occur differently depending on the metal used, and so different catalysts produce different carbon morphologies, as shown in Figure 7.

Carbon morphology is also known to be temperature dependent. Without a catalyst, the hardness of the carbon produced was found to increase with temperature, and the particle size to decrease [2]. Using a Ni catalyst, low temperatures around 500 °C caused the formation of full carbon nanofibres, while temperatures around 750 °C produced hollow fibres. This was attributed to a higher rate of carbon atom diffusion through the metal particles [53] and a higher nucleation rate disfavouring sites with a long diffusion path at higher temperatures [29]. Using a Co catalyst, dense carbon

Figure 6: Various carbon morphologies produced by the TCMD process [29]. Highly ordered forms of carbon are desirable products of this process and thus the catalysts and reaction conditions that produce them are favoured.

Figure 7: Representation of literature data on catalysts, preferred temperature range and carbon products related to TCMD. Catalysts: 1—Ni-based, 2—Fe-based, 3—carbon-based, 4—summary of data related to Co, Ni, Fe, Pd, Pt, Cr, Ru, Mo, W catalysts, 5—non-catalytic decomposition. Carbon products: CF—carbon filaments, TC—turbostratic carbon, GC—graphitic carbon, AmC—amorphous carbon [39].

nanofibres were again produced at around 500 °C, hollow nanofibres between 600 °C and 700 °C, and various forms of single-walled nanotubes at higher temperatures [56].

The feed gas composition also affected the morphology of the depositing carbon. Adding 0.6 vol% of hydrogen to the methane feed over a nickel-alumina catalyst at 500 °C prevented carbon nucleation entirely [28], while at lower levels, increasing hydrogen percentage shifted the carbon morphology from filament-like to bamboo-like. Hydrogen is thought to reduce the carbon deposition rate and increase the carbon removal rate, and as such is a useful tool for finding the balance required for carbon fibre growth as discussed earlier [29].

2.2.3 Reactor Design

The design of the reactor for TCMD is critical to minimising catalyst deactivation. Reactors have been trialled with fixed and fluidised catalyst beds, single chambers and multiple chambers in series at different pressures.

The simplest reactor is a stainless steel tube contained within a furnace, with a fixed quantity of catalyst loaded before heating, and gas intake and exit streams. Solid carbon must be periodically removed from this reactor to prevent the gas flow from being blocked, and this makes fixed bed reactors impractical for continuous operation [3]. It also means that accurately determining the maximum carbon yield of a given mass of catalyst may not be possible due to reactor space limitations.

Fluidised bed reactors use a continuous flow of fine catalyst particles through the reaction zone transported by a carrier gas, allowing deactivated particles to be removed and fresh catalyst to be added without halting the process. Fluidised beds are more effective at transferring heat to catalyst but require a carbon scrubber to remove particles from the exit gas feed [3]. Also, the use of a fluidised bed creates a high catalyst turnover, meaning

that the catalyst must be low cost for such a process to be economical.

Multi-chamber fluidised bed reactors have been developed that attempt to extend the lifetime of the catalyst by altering the parameters of each chamber. It has been shown that multiple reactors in series are superior to having them in parallel, depending on the design [13]. In one case, a 3-5 chamber series counter-flow reactor was designed, whereby the methane feed gas flow was opposite to the fludised catalyst bed flow. The reactor chambers were at increasing pressures, and the methane flowed from high to low pressure, while the catalyst flowed from low to high. This meant that as the catalyst deactivated, the increasing pressure would allow the methane to access deeper pores, kinetically favouring hydrogen conversion and extending the lifetime of the reaction. In the low pressure chambers, hydrogen production was more thermodynamically favoured [13].

Separation of the hydrogen from the exit gas stream can be done at lab scale using a gas chromatograph, and on a commercial scale using a pressure swing adsorption system as is used for SMR.

2.3 Iron Ore Catalysis of Thermal Methane Decomposition

The catalysis of TCMD with plain powdered iron ores such as hematite (Fe_2O_3) and magnetite (Fe_3O_4) has been studied specifically, and identified as suitable catalyst choice for a commercial TCMD process. These powdered ores are referred to as unsupported polycrystalline particles, because they are macroscopic aggregates of clusters of smaller iron crystals. Iron has a lower activity than Ni in this form, but is more stable at the higher temperatures needed for high hydrogen conversion (700-1000 °C) [13]. It is also low cost (around \$150/t), meaning much higher catalyst turnover rates can be sustained in fluidised bed reactor continuous operation than for a high

cost catalyst such as Ni (around $20,000/t). The low cost also means that chemical methods of carbon purification can be used to remove the carbon, even if the catalyst would be damaged as a result.

Cornejo [13] describes a conceptual model for TCMD using unsupported polycrystalline iron ore as a catalyst. They suggest that the mechanism of iron catalysis is similar to that displayed in Figure 4, but contains an additional intermediate step called the carbide cycle. Rather than simply diffusing through the catalyst crystal in step 3 of Figure 4 as is observed for Ni catalysts, carbon atoms saturate the Fe crystals, forming a cementite (Fe_3C) crystal [19]. This cementite crystal is stable until decomposition is triggered by a low-surface energy carbon particle depositing on the surface. The lower surface energy allows the carbon to leave its cementite form and aggregate into carbon structures, while the crystal returns to ferrite. This means that multiple cycles of carbon dissolution, cementite formation, and graphite precipitation can occur. The catalyst crystal eventually deactivates when the carbon structures on the particle prevent methane diffusing into contact with the Fe.

The method of catalyst reduction affected the performance of iron as a catalyst [13]. Reduction with methane during the reaction caused higher activity than pre-reduction with hydrogen. It is thought that there is a synergistic effect on catalyst performance when catalyst reduction and methane decomposition take place simultaneously. Hydrogen from the decomposition of methane causes reduction localised to the decomposition site. Reduction also produces water vapour, which in small amounts has been observed to reduce the production of deactivating carbon morphologies and increase the catalyst lifetime [60]. As a result, letting the catalyst be reduced within the reaction itself is beneficial. In addition, cementite formation occurs more easily in iron oxides, and pre-reduction would eliminate this possibility. However, because of the removal of oxygen from the iron oxides during the re-

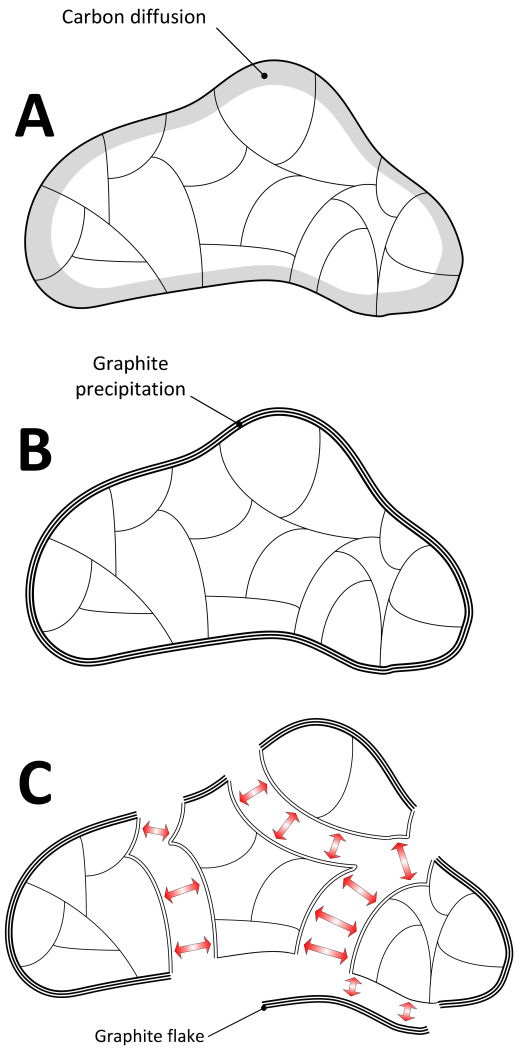

Figure 8: First cycle of polycrystalline iron particle metal dusting. **A**: SCM1 - Shrinking Core Model, first cycle. Methane dissociates and carbon diffuses into the boundary region of the reduced iron particle. **B**: SCD1 - Surface Carbide Decomposition, first cycle. Formation of graphite skin around the particle allowing saturation of crystal clusters. **C**: CCM1 - Crackling Core Model, first cycle. Precipitation of graphite along the boundary of saturated crystal clusters pushes the particle apart. Reproduced with permission from A. Cornejo [13].

action, small amounts of water vapour, CO_2, and CO were produced during reduction, which had to be purified out of the exit gas stream.

In experiments done comparing different types of iron ore, it was shown that the oxidation state of iron did not affect its hydrogen conversion rate, and any impurities in low-grade ores only served to increase its catalytic activity [13]. However, oxide catalysts must be highly uniform to produce uniform carbon morphologies [29].

The lifetime of the iron ore catalyst is determined by metal dusting [13, 19, 50]. The metal dusting process follows an iterative multi-stage process that incorporates three established models of solid-fluid reactions: The shrinking core model (SCM) [59], crackling core model (CCM) [48], and cracking shrinking model (CSM) [33]. First, the iron ore must be completely reduced to ferrite (α-Fe). Next, methane adsorbs to the surface of the particle, and as the methane dissociates, carbon atoms dissolve into the surface region of the polycrystalline ferrite, forming iron carbide (or cementite, Fe_3C), and approximately following the shrinking core model. This is shown in Figure 8A. At a certain point, the boundary region of the polycrystalline particle becomes saturated with carbon, which then precipitates as layers of graphite on the surface [19]. This is called Surface Carbide Decomposition (SCD) and is shown in Figure 8B. As this graphite layer builds up, it inhibits the diffusion of methane into contact with the iron surface. This slows the reaction rate, and thus the rate of precipitated carbon build-up on the surface. Because of this, freshly dissociated carbon is able to diffuse deeper into the particle and saturate entire crystal clusters, not just the sub-surface boundary regions. The precipitation of graphite from these saturated crystal clusters occurs along all boundaries of the crystal cluster, including those internal to the polycrystalline particle. Such precipitation forces the crystal clusters within the particle to separate, according to the Crackling Core Model, and creates graphite flakes. This step is shown in Figure 8C, and is the final stage of the

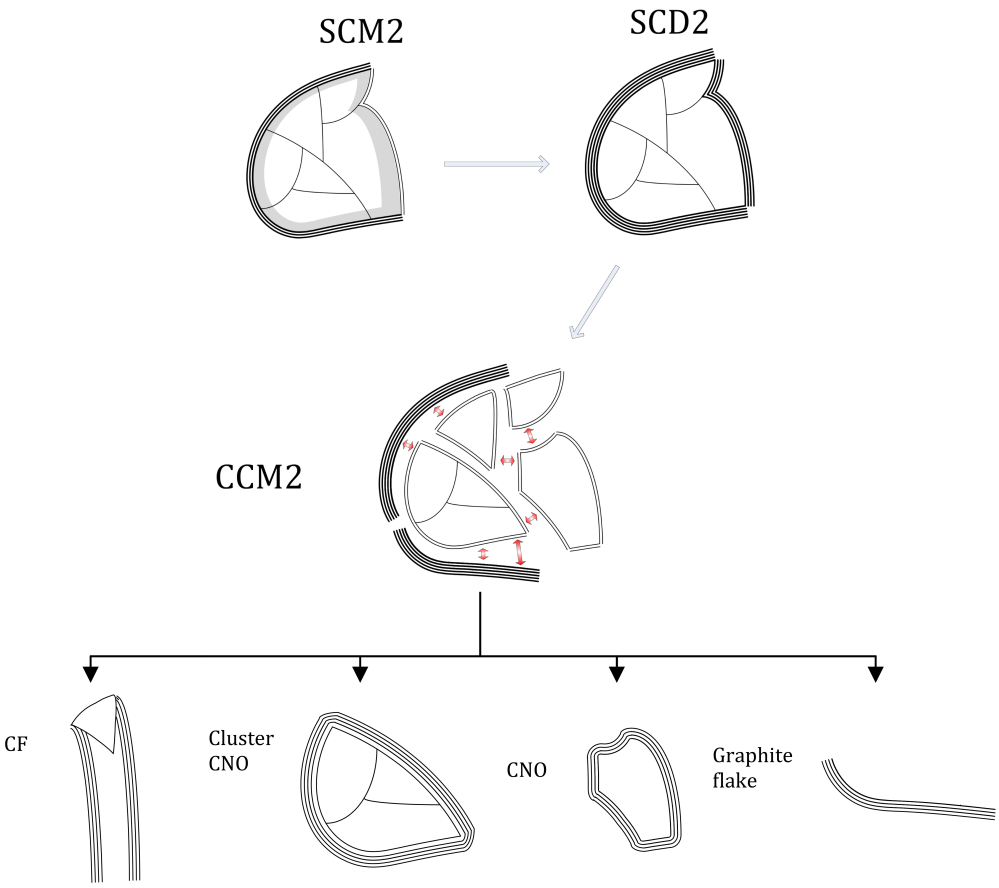

Figure 9: The second cycle of polycrystalline iron particle metal dusting. SCM2 - Shrinking Core Model, second cycle. SCD2 - Surface Carbide Decomposition, second cycle. CCM2 - Crackling Core Model, second cycle. This cycle involves the metal dusting of crystal clusters separated from the bulk in the first cycle. If dusting continues until the iron particle is split into individual crystals, then carbon fibers or carbon nanoonions will form. If deactivation occurs before dusting is complete, cluster carbon nanoonions will form. Graphite flakes are formed from the carbon shell separating during dusting. Reproduced with permission from A. Cornejo [13].

first cycle of metal dusting.

The separated crystal clusters have surfaces that are newly exposed to the feed of methane, which are again saturated with carbon according to the SCM, beginning the cycle again [13]. The second cycle of metal dusting is shown in Figure 9. The metal dusting cycle repeats until either the iron particles have dusted into single crystals, or premature deactivation occurs. Single iron crystals follow the carbide cycle as described earlier. Premature deactivation occurs when methane can no longer contact the iron surface, because the reaction kinetics provide insufficient energy for the methane to diffuse through the carbon layer. In this case, the final carbon morphology will be a cluster carbon nanoonion as shown in Figure 9. Reaction conditions can be chosen to promote metal dusting and prevent premature deactivation. Overall, the number of metal dusting cycles depends on the size of the polycrystalline iron particles, the size of the individual crystals within the particle, and the reaction conditions.

At temperatures over 900 °C, the rate of methane pyrolysis (non-catalytic methane decomposition) increases, which produces amorphous carbon that accelerates the deactivation of the iron particle [13].

2.4 Ironsands Catalysis of Thermal Methane Decomposition

This research is focused on the use of titanomagnetite from New Zealand ironsands as a TCMD catalyst. Titanomagnetite has the structure $Fe_{3-x}Ti_xO_4$, where $0 \leq x \leq 1$. It is a solid solution of magnetite (Fe_3O_4, $x = 0$) and ulvöspinel ($Fe_2TiO_4, x = 1$), with an inverse spinel cubic structure as shown in Figure 10. Titanomagnetite's structure can be restated as $xFe_2TiO_4(1\text{-}x)Fe_3O_4$ to better indicate its composition [30]. For New Zealand ironsand, x is commonly between 0.25 and 0.28 [51].

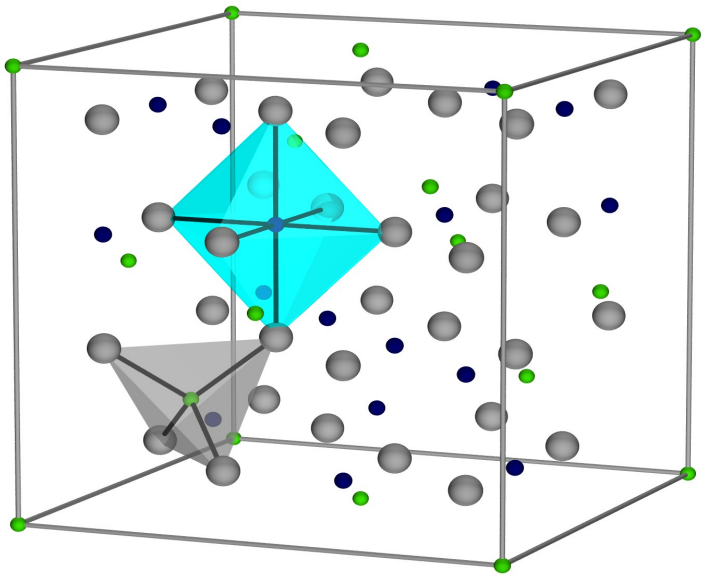

Figure 10: A schematic of the spinel cubic crystal structure unit cell. In magnetite, the grey atoms are O, the green atoms are Fe^{2+}, and the blue atoms are Fe^{3+}. In titanomagnetite, titanium is incorporated into the lattice by substituting two green Fe^{3+} atoms with a Ti^{4+} atom and an Fe^{2+} [38]. In naturally occurring titanomagnetite such as in ironsands, small amounts of other metals such as Al^{3+} and Mg^{2+} are also substituted. Image by David Schrupp, generated from data by W.H. Bragg and F.R.S. Cavendish [18]. Reproduced under Creative Commons Licence CC BY-SA 2.0 DE.

The literature does not contain information on the catalytic activity of $TiFe_3O_4$ for TCMD, but it does have information on how the titanium in the iron ore affects the formation and stability of cementite (Fe_3C), the key intermediate in the carbide cycle.

During the formation of cementite, titanomagnetite had a slower reduction rate than hematite, and was more effectively reduced when the feed gas composition included up to 30% hydrogen, while hematite performed better under methane autoreduction. This is relevant to TCMD because the reduction of the catalyst affects the methane decomposition step, as discussed earlier, and so slower reduction may delay the reaction. The slow reduction of

titanomagnetite is due to its stability and crystal structure. By pre-oxidising the titanomagnetite to titanohematite, its reduction rate was increased to almost that of hematite [30].

The overall rate of cementite formation was also slower for titanomagnetite than for hematite, even when the reduction rate had increased. This was thought to be because of unreduced titanium, magnesium, and calcium oxides within the crystal structure. CaO is a known suppressor of cementite formation, although this may be simply due to the lower availability of metal active sites due to the presence of oxygen [30].

Titanium in the iron ore increases the stability of cementite relative to pure hematite, and this stability is at a maximum between 750 and 770 °C [31]. Because cementite decomposition is an intermediate step in the TCMD process, higher cementite stability is likely to slow the reaction and cause it to require more energy to proceed.

3 Materials And Methods

3.1 Experimental Setup

Two different tubes were used as reaction vessels in experiments for this project. The first was a 500 mm long, 38 mm OD stainless steel tube, with a K-type thermocouple (Nickel-chromium, -270 °C to 1260 °C ±2.2°C) inset into one end cap, that allowed accurate temperature readings in the reaction zone at the centre of the tube. The ends of the tube were sealed with clamped Teflon gaskets for experiments at temperatures below 900°C, and copper gaskets for experiments at temperatures of 900°C or higher. The second was a 40 mm OD quartz tube, 1000 mm in length, with clamped Teflon O-ring seals for experiments at all temperatures. At low flow rates and high temperatures, the stainless steel tube seals proved less reliable, and so the quartz tube was used.

The vessel was heated using a Carbolite 1200°C Split Tube Furnace (HST Model 12/400). The catalyst was deposited in the centre of the tube using a long-handled scoop. All runs used 1.85 g of catalyst.

Cylinders of high purity methane and argon gas (99.995% and 99.99% purity respectively, BOC Gases) were linked to the setup using a Swagelock 90° ball valve to allow on-stream gas selection. The gas line then passed through a pressure gauge and a rotameter for flow control. A schematic and photo of the experimental setup are shown in Figure 11.

The rotameter was calibrated for air at 100 kPa, so the nominal flow rate was converted to the true flow rate of methane using

$$\text{Corrected Flow Rate} = \text{Nominal Flow Rate} \times \sqrt{\frac{SG_{air}}{SG_{methane}}} \qquad (8)$$

where SG_{air} and $SG_{methane}$ are the specific gravities of the respective gases at

(a) Experimental setup schematic. The gaskets on either end of the tube were clamped, and could be opened to load and unload the tube.

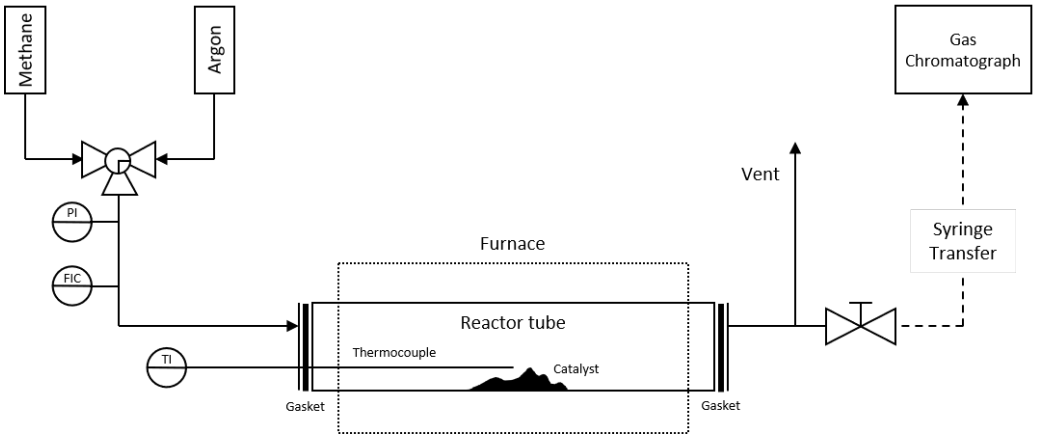

(b) Photo of experimental setup, with stainless steel reactor tube.

Figure 11

100 kPa and 18 °C ($SG_{air} = 1$ and $SG_{methane} = 0.54785$). Nominal flow rates of 0.5, 0.25, 0.05, and 0.01 L/min were used in this research, corresponding to real flow rates of 0.67, 0.34, 0.067, and 0.013 L/min respectively.

After the catalyst was loaded and the vessel sealed, the reaction chamber was purged with argon for 45 minutes at approximately 0.5 L/min, while the reaction vessel was heated to the desired temperature at a rate of 15 °C/min. When the tube was at temperature, the argon was replaced with methane at the desired flow rate. Samples were taken via a septum periodically from the exit gas stream using plastic gas-tight syringes. The interval between samples varied between 5 and 30 minutes, depending on the flow rate and purpose of the run. At the beginning of an experimental run, during the activation of the catalyst, sampling was typically done every 10 minutes for the first hour, and then every 30 minutes for the remainder of the run. The samples were analysed using gas chromatography to determine the conversion rate of methane to hydrogen. The remaining gas was then vented.

Upon completion of the experiment, the methane supply was again replaced with argon and the vessel was allowed to cool to room temperature over a period of 3-4 hours. Any carbon produced by the experiment was removed and weighed. Carbon samples were analysed using Thermo-Gravimetric Analysis (TGA), Powder X-Ray Diffraction (PXRD), and Raman Spectroscopy.

3.2 Analytical Model

This section describes the methods used to calculate the conversion of methane to hydrogen, the maximum conversion efficiency for a given temperature, and the level of graphitisation of carbon samples.

3.2.1 Methane Conversion

A gas chromatograph (GC) was used to measure the volume percentages of CH_4 and H_2 in the syringe samples from the exit gas stream of the reaction tube. To do this, the integrals of the CH_4 peak (Retention time $\approx$ 7.6 mins) and the H_2 peak (Rt $\approx$ 2.1 mins) were input into their respective standard curve equations (See Appendix A.1) to give the volume percentage (vol%). To determine the percentage conversion efficiency of methane to hydrogen (X_{CH_4}), two methods were used. The first uses only the volume percentage of hydrogen [6]:

$$X_{CH_4} = \left(\frac{\%H_2}{200 - \%H_2} \right) \cdot 100 \tag{9}$$

The second uses the volume percentages of both methane and hydrogen [16]:

$$X_{CH_4} = \left(\frac{\frac{\%H_2}{2}}{\%CH_4 + \frac{\%H_2}{2}} \right) \cdot 100 \tag{10}$$

Assuming that methane and hydrogen are the only gases present in the exit stream of the reactor, these methods produce the same result mathematically, but sometimes differences between them arise due to inaccuracies in the GC measurement. The average of both methods was used in this research in order to minimise the effects of such inaccuracies. The mathematical equivalence of these two equations is proven in Appendix C, the errors associated with GC measurements are discussed in Section 4.4.1, and an example of a gas chromatograph is shown in Appendix B.

The assumption that only H_2 and CH_4 were present in the exit stream was expected to be valid based on similar experiments in literature [6, 13, 16], and was retained in all data analysis for this project. However, as discussed in Section 4.4.1, there was evidence of water vapour in the GC exit gas samples later in the project. No correction for this was made, because the

gas chromatograph used to measure the exit gas stream was not equipped to measure moisture content. Had this problem been anticipated, a separate analytical technique or a gas chromatograph with a different detector could have been found that would have allowed quantification of these water volumes and improved the quality of a subset of the data.

Two tube reactors were used in this research: a stainless steel tube, and a quartz tube. Blank baseline runs at each temperature and flow rate were run for each tube, and these values have been subtracted from all methane conversion ratio values presented in this research, unless otherwise stated. Baseline values can be found in Appendix A.2. In the names of experimental runs, a Q indicates that the quartz tube was used, otherwise, the steel tube was used. Because of the baselining process, the tube type is a controlled variable and was ignored when calculating trends and drawing conclusions. As a result, on the same graph, some series names may contain a Q, and others may not.

3.2.2 Thermodynamic Equilibrium Limit

The Thermodynamic Equilibrium Limit (TEL) is the maximum value of X_{CH_4} thermodynamically possible under a given set of reaction conditions. To calculate the TEL of the conversion ratio of methane to hydrogen for a given temperature, the equilibrium constant of the reaction at that temperature (K_T) must be calculated. The TEL can then be expressed in terms of K_T, temperature, and pressure [14].

The equilibrium constants and thermodynamic equilibrium limits used in this research were calculated using the method outlined in the Supporting Information of Cornejo et al. [14]. The K_T and TEL values for each temperature considered in this research are displayed in Table 1.

Table 1: Equilibrium constants and thermodynamic equilibrium limits for the conversion of methane to hydrogen in TCMD. The pressure was constant at 1 bar.

Temperature (°C)	K_T	TEL
800	21.849	91.9%
850	34.331	94.6%
900	51.988	96.4%
950	76.194	97.5%

3.2.3 Characterisation of Carbon/Catalyst Particles

To determine the level of graphitisation of the carbon produced in this research, four indicators were used: mass-loss temperature, graphitic degree, crystal size, and disorder.

The 50% mass-loss temperature of carbon in TGA is an indication of the graphitisation of the sample. TGA measures the thermal stability of a carbon sample by heating it under air and observing the 50% mass-loss temperature. An example of a TGA curve can be found in Appendix B. Amorphous carbon is more easily oxidised than ordered graphite, resulting in mass loss at lower temperatures during TGA. Amorphous carbon typically has a 50% mass-loss temperature of below 450 °C. Above 550 °C indicates well graphitised carbon [5, 22]. However, the reliability of TGA 50% mass-loss temperatures as a precise predictor of graphitisation is uncertain, and may not be useful for distinguishing between samples with small mass-loss temperature differences. For the remainder of this research, the temperature at which a TGA carbon sample has lost half its mass is referred to as the TGA half-temp.

The graphitic degree of a sample is calculated using Powder X-Ray Diffraction (PXRD) data. PXRD measures the x-ray diffraction spectrum of the carbon/catalyst particle and uses it to calculate structural information about the crystals in the sample. First, the position of the graphite 002 peak in the

PXRD spectrum is used to calculate the interplanar spacing d according to Braggs Law:

$$d = \frac{\lambda}{2sin\theta_{002}} \tag{11}$$

where λ is the radiation wavelength, and θ_{002} is the (002) reflection angle. The layer spacing is then compared to that of ideal graphite to determine the fractional degree of graphitisation g :

$$g = \frac{(3.440 - d)}{(3.440 - 3.354)} \tag{12}$$

where 3.354 is the ideal layer spacing of a single crystal of graphite without defects, and 3.440 is the layer spacing of turbostratic carbon (carbon with crumpled or randomly folded layers) [7]. The higher the fractional degree of graphitisation, the more graphitic the carbon sample is.

The average crystal size of the carbon/catalyst particles (called PXRD Average Particle Diameter or Avg PD in this work) can also be calculated from PXRD data, using diffraction peak broadening and the Scherrer formula:

$$d_c = \frac{k\lambda}{\beta_{\frac{1}{2}} \cos\theta} \tag{13}$$

where d_c is the average diameter of a carbon/catalyst sample crystal, k is the Scherrer coefficient (approximately equal to 1), λ is the is x-ray radiation wavelength (1.5405 Å), $\beta_{\frac{1}{2}}$ is the Full Width at Half Maximum (FWHM) of the diffraction peak in radians, and θ is the Bragg angle of the peak maximum [49]. The Scherrer formula may produce different values when different diffraction peaks are used, due to anisotropy of the sample particles. However, it is useful as a comparative measure of graphitisation, as larger crystal sizes tend to indicate higher graphitisation of the sample. In this research, the (002) peak was used to calculate all crystal size values. An example PXRD spectrum collected as part of this research is shown in Appendix B.

Because the FWHM is used to calculate crystal size, it is affected by peak broadening caused by the presence of amorphous carbon or other materials with low crystallinity. Graphitic degree, on the other hand, uses the Bragg angle, and is not affected by the presence of these materials. As a result, these two indicators of carbon quality sometimes diverge for the same sample. In these cases, the graphitic degree is taken as an indicator of the core graphite within the shell of amorphous carbon, while the crystal size measurement encompasses the disorder of the amorphous carbon and gives a better average indication of the graphitisation of the entire sample [13].

Disorder in the carbon sample implies that it is less graphitic, and Raman spectroscopy can be used to estimate this. The Raman spectrum of graphite contains two key peaks: The D band, at 1341 cm^{-1}, and the G band, at 1568 cm^{-1}. The intensity of the D band is an indication of disorder, as it is produced by the vibrations of atoms with dangling bonds, such as those in defects in the lattice. No D peak is present in defect-free, highly ordered pyrolitic graphite. The intensity of the G band is produced by vibrations of sp^2 bonded atoms in the graphite lattice, and is high in highly ordered graphite. The ratio of the intensities of the D and G peaks (I_D/I_G) is often used to indicate the level of disorder in a carbon sample, where a low ratio corresponds to a low level of disorder [32, 52]. An example of a Raman spectrum collected in this research can be found in Section B.

Raman spectroscopy has limitations that affect the reliability of its predictions of carbon disorder. Carbon strongly absorbs visible light, meaning most sub-surface scattering is re-absorbed by the sample. As a result, the scattering received by the detector is predominantly from the surface of the sample. While the sample particles were mixed, they were not ground or crushed before characterisation, so the measures of disorder produced by Raman analysis are only representative of the surface carbon. In addition, Raman spectroscopy has a small focal point of less than 50 microns, which

gives a small collection volume and is therefore subject to sub-sampling inaccuracies. Several spectra were typically averaged to account for this, but it may still affect the results.

3.3 Instrumentation

Gas samples were analysed using a Shimadzu GC-2014 Gas Chromatograph with an Alltech CTR I Concentric Packed Column (Category 8700) and a Thermal Conductivity Detector. Nitrogen was used as the carrier gas. Syringe samples were manually injected into the chromatograph.

All TGA measurements were carried out using an Alphatech Systems TGAQ50 instrument, platinum sample holders, and alumina sample pans. The carbon-coated catalyst particles were heated from room temperature to 850°C at 10°C/min in a linear temperature ramp, with an air flow rate of 0.4 L/min.

All Powder X-ray Diffraction measurements were carried out on a Rigaku Spider X-ray diffractometer with Cu Kα radiation (Rigaku MM007 microfocus rotating-anode generator), monochromated and focused with high-flux Osmic multilayer mirror optics, and a curved image plate detector.

All Raman Spectroscopy measurements were made using a home-built Raman microscope based on an Olympus IX70 inverted fluorescence microscope with 532 nm diode laser excitation. Excitation was spectrally filtered using an OptiGrate Volume Bragg bandpass filter, then directed to the sample by an Iridian Spectral Technologies Raman edge filter. Excitation was focused onto the sample with a NA = 0.65 (40x magnification) objective. Typical excitation power at the sample was < 2 mW (to avoid sample damage). Raman scattering was collimated with the same objective and residual Rayleigh scattering was removed with an additional Iridian Spectral Technologies Raman edge filter before being focused in free space to the 50 micron

slit of a Princeton Instruments FERGIE spectrometer.

The major oxide compositions of ironsands used in this research were determined using X-Ray Fluorescence. All XRF measurements were carried out by SpectraChem Analytical, CRL Energy Ltd. Samples were oven dried at 110 °C under air, and then heated to 1000 °C in air for 1 hour to oxidise them. Weight changes from this process are displayed in relevant tables as a percentage Loss On Ignition (LOI). Samples were prepared using borate fusion before XRF analysis.

Particle size distribution measurements were made using a Malvern Mastersizer 3000.

3.4 Materials

The raw materials used in this research are as follows:

- Patea ironsand (I): Raw ironsand taken from the beach at Patea, in the Taranaki region.
- Magnetically purified Patea Ironsand (IP): Patea ironsand, hand purified using a magnet.
- Glenbrook ironsand (G): Ironsand from the Glenbrook sand mine at the Waikato Heads. This sand was pre-purified using the industrial magnetic concentrators at the mine.
- Hematite control (H): 99.4%, <5 μm, Milton Adams. Every effort was made by the university to obtain hematite with a size distribution closer to that of the ironsand, but at the time, this was the only commercially available hematite at high purity.

The composition of each type of ironsand is shown in Table 2. After magnetic purification, the iron oxide content of the Patea ironsand increased from 52.0% to 80.5%. The iron oxide and corresponding elemental iron content of each material are listed in Table 3. In ironsand, the iron oxide present

is magnetite, or Fe_3O_4, which has 2.4% more Fe by weight than the hematite control, Fe_2O_3.

The XRF analysis in Table 2 shows that purified Patea and Glenbrook ironsands contain about 7.5% titanium. However, XRF does not show the way in which the titanium is incorporated into the magnetite lattice as ulvöspinel, as discussed in Section 2.4. Normally XRD analysis would to obtain this kind of structural information. However, magnetite and ulvöspinel have the same spinel cubic crystal structure, making it impossible to resolve the difference with the available laboratory XRD instrument [51].

The XRF analysis also shows that calcium, silicon, and magnesium oxides were removed during magnetic purification. For example, unpurified Patea Ironsand contained 22.54% SiO_2, which decreased to 4.37% after purification. This shows that these elements were not incorporated into the magnetite lattice, but were instead present as separate oxide crystals. The fact that the percentage of titanium increased with purification shows that it was in fact incorporated into the iron oxide lattice as titanomagnetite.

Particle size distribution data for Patea ironsand and hematite is shown in Table 4.

Oxide	Patea (I)	Pure Patea (IP)	Glenbrook (G)
Fe_2O_3	51.97	80.46	83.75
MnO	0.54	0.65	0.63
TiO_2	4.81	7.44	7.77
CaO	8.62	1.51	0.73
K_2O	0.14	0.08	0.03
SO_3	< 0.01	< 0.01	< 0.01
P_2O_5	0.29	0.37	0.12
SiO_2	22.54	4.37	2.63
Al_2O_3	4.31	3.94	3.69
MgO	7.57	3.48	2.99
Na_2O	0.41	0.21	0.07
V_2O_5	0.34	0.54	0.58
LOI	-1.57	-2.94	-3.07
SUM	99.97	100.11	99.93

Table 2: XRF major oxides analysis showing the composition of ironsands used in this research. Values are expressed as weight percentages. LOI is Loss On Ignition, a measure of the mass change when the sample was heated before analysis.

Catalyst Type	% Iron Oxide	% Fe by Weight
Patea Ironsand (I)	51.97%	36.35%
Pure Patea (IP)	80.46%	56.28%
Glenbrook (G)	83.75%	58.58%
Hematite (H)	100.00%	69.94%

Table 3: Iron content of catalysts used in this research.

Catalyst	D_{10}	D_{50}	D_{90}	$D_{4,3}$	$D_{3,2}$
I	157	265	446	286	245
IP	35.4	180	296	182	44.0
G	15.7	128	202	124	25.8
H	0.426	0.984	2.78	60.9	2.01

Table 4: All values are in units of μm. Particle size distribution data of catalysts used in this research. D_x values indicate that x% of particles had a diameter lower than the given value. $D_{4,3}$ refers to the volume moment mean diameter. $D_{3,2}$ refers to the surface area moment mean diameter.

4 Results and Discussion

The goal of this research was to investigate the effect of as many variables as possible on the performance of ironsands for TCMD, and compare them to the hematite control. This meant constructing an experimental matrix of the highest priority variable combinations that would be manageable in the time allotted. With the exception of reaction pressure, which was rejected for technical reasons, catalyst type, temperature, flow rate, and catalyst particle size were identified as being the most useful parameters of a commercial process. Experiments covering all combinations of these variables were planned, but as the work went on, and there were repeated setbacks related to experimental equipment, it became clear that the experimental matrix would not be completed. The final variables considered are listed here:

- Catalyst type:
  - Hematite (H), Unpurified Patea Ironsand (I), Purified Patea Ironsand (IP), and Glenbrook ironsand (G)
- Temperature:
  - 750, 800, 850, 900, and 950 °C
- CH_4 flow rate:
  - 0.67, 0.035, 0.067, and 0.013 L/min
- Particle Size:
  - Natural size distribution, and <100 μm

It would have been beneficial to test additional particle sizes. In addition, the characterisation of catalysts in this research would have benefited from optical microscopy and SEM images. In hindsight, this should have been prioritised over other types of characterisation from the beginning, but it was not. In part, this was due to the fact that this research was commissioned by an industry partner, and the comparison of ironsand with hematite was a key deliverable included by them. Had there been less focus on compar-

ison with hematite, the project might have focused more strongly on the characterisation of the ironsand itself.

To provide insight into the decision making process and the flow of experimental work, a timeline is given here:

- A short test run with hematite at 850 °C and 0.67 L/min CH_4 flow rate was carried out to prove that the experimental setup worked.
- 4-5 hour, 0.67 L/min runs of unpurified Patea ironsand (I) and hematite (H) were carried out at 850 °C and 950 °C as a preliminary test of temperature effects, and then additional runs at 750, 800, and 900 °C for both H and I were done to finish off this section of the experimental matrix.
  - 800 °C was confirmed as the activation temperature for the reaction, so no further experiments were carried out at temperatures lower than 850 ^{c}ircC.
- Glenbrook sand (G) was obtained and tested at 0.67 L/min and 850 °C. This sand performed much better than I and H under these conditions, which incentivised the magnetic purification of the Patea ironsand.
- Purified Patea Ironsand (IP) was tested under the same conditions.
- IP was then sieved to <100 μm to investigate particle size effects at 0.67 L/min and 850 °C. There was no significant difference in activity observed, so the priority of this variable was lowered.
- Following this, IP was used to begin exploring flow rate effects at 850 °C, by stepping down the flow rate gradually during a single run and measuring the changes in methane conversion ratio.
  - During these experiments, problems with the seals at low flow rates for the stainless steel tube caused delays while a quartz tube was obtained.
  - Additional flow meters also had to be obtained during this time.
  - 0.013 L/min was found to be the lowest flow rate that was unaf-

fected by mass transfer issues in the new quartz tube.

- At 0.013 L/min, IP was used to attempt a full deactivation run overnight in the quartz tube. The maximum allocated time for a single run on the shared furnace was 24 hours, including heating and cooling, allowing approximately 20 hours for deactivation. At this flow rate, the catalyst had not deactivated in time. This was attempted twice before the decision was made to raise the flow rate.
- Further flow rate studies were carried out to try and find a flow rate that would allow deactivation in the 20 hr period while not sacrificing methane conversion too much.
- A flow rate of 0.067 L/min was decided upon for complete deactivation runs, and deactivation of both IP and H was observed within 18 hours at this flow rate and 850 °C.
- A time consuming complete deactivation temperature study was then carried out, with 18 hr H and IP runs at 0.067 L/min and 850, 900, and 950 °C.
- A 0.013 L/min, <100 μm IP run was done.
- Throughout this time, duplicate runs were performed where time allowed.

The results of each experiment are described in terms of dependent variables, which are loosely split into two categories: "Catalyst Activity and Decay", and "Carbon Quality". These two categories are used to structure the results section.

The Catalyst Activity and Decay section encompasses variables that provide information on how effectively the reaction produced hydrogen. This includes conversion ratio data, along with time data documenting the times of various points of interest, such as the time of maximum conversion ratio, or time until loss of activity of the catalyst. It also includes carbon and hydrogen yield values.

The Carbon Quality section encompasses variables that describe the level of graphitisation of carbon produced in the reaction. These variables are obtained from carbon characterisation data.

Both sections draw upon raw data included in two key summary tables. The first, Table 5, contains raw data from each experimental run, with replicate runs displayed individually. The second, Table 6, contains data from all experimental runs, relative to each run's respective control. Replicate runs were averaged before the control value was subtracted to produce the values in this table.

Table 5: Summary of all results obtained in this research. Missing values are explained below, after their respective column headings. A: Max Conversion Ratio(%); B: t_{max} (min); C: SCA_1 (%), value missing due to insufficient samples after late maximum; D: $t_{\frac{1}{2}max} - t_{max}$ (min), low flow rate runs had no $t_{\frac{1}{2}max}$ value due to slow decay; E: Carbon yield (g C / g Fe); F: Mass carbon (g); G: TGA Half-temp; H: PXRD Graphitic Degree; I: PXRD Avg Particle Size (nm); J: Raman D/G Ratio, could not acquire a value from HQ850 or I850 runs, as no G peak was present. The I950 duplicate run was mishandled and its carbon was not characterised by any method.

Table 5: Summary of Results

Catalyst Type	Tube Type	Temp. (°C)	t_{total} (hrs)	Flow (L/min)	Size (nm)	A	B	C	D	E	F	G	H	I	J
H	S	800	4	0.67	Normal	8.5	120		120	1.67	1.60	570	0.865	142.6	0.215
I	S	800	4	0.67	Normal	4.7	55	91.2	95	3.70	1.31	615	0.484	142.8	0.453
G	Q	850	5	0.013	Normal	73.2	210	90.7		1.69	1.06	620	0.836	193.8	0.325
G	Q	850	5	0.013	Normal	79.0	180	94.8		1.68	1.05	614	0.836	188.5	0.158
H	Q	850	4.5	0.013	Normal	65.6	180	91.0		1.00	0.73	584	0.996	222.8	
H	S	850	7	0.013	Normal	69.0	60	85.5	360	1.99	2.02	571	0.836	156.4	0.239
IP	Q	850	5	0.013	<100 μm	70.4	180	95.8		1.59	0.85	620	0.880	187.1	0.477
IP	Q	850	5	0.013	<100 μm	58.2	210	80.6		1.50	0.75	612	0.923	187.4	0.258
IP	Q	850	4.5	0.013	Normal	73.1	180	94.8		1.79	1.05	623	0.793	191.7	0.445
IP	Q	850	20	0.013	Normal	66.1	180	76.7		6.97	6.45	610	0.851	190.8	0.274
IP	S	850	8	0.013	Normal	80.1	240	91.0		4.15	3.52	607	0.880	205.4	0.186

Continued on next page

Catalyst Type	Tube Type	Temp. (°C)	t_{total} (hrs)	Flow (L/min)	Size (nm)	A	B	C	D	E	F	G	H	I	J
H	Q	850	18.5	0.067	Normal	41.5	90			3.07	3.42	612	0.865	148.0	0.372
H	Q	850	18.5	0.067	Normal	37.6	45	83.3		3.21	3.60	610	0.909	153.0	0.242
IP	Q	850	18.5	0.067	Normal	70.9	90	67.6		4.96	4.36	622	0.880	204.0	0.280
IP	Q	850	18.5	0.067	Normal	63.5	90	81.7		5.41	4.83	626	0.793	165.2	0.282
IP	Q	850	15.5	0.067	Normal					4.92	4.31	623	0.778	159.6	0.276
IP	S	850	4	0.34	Normal	35.7	35	45.3	20	2.86	2.17	616	0.602	163.8	0.322
G	S	850	5	0.67	Normal	18.8	35	36.0	20	3.09	2.59	618	0.573	145.8	0.318
H	S	850	5.5	0.67	Normal	11.9	45	47.7	45	2.01	2.05	570	1.024	186.7	0.228
I	S	850	5	0.67	Normal	11.0	30	42.1	30	4.37	1.76	585	0.631	147.5	
IP	S	850	4	0.67	<100 μm	19.7	45	43.6	15	2.70	2.00	610	0.602	155.2	0.378
IP	S	850	4.5	0.67	Normal	18.4	45	45.7	15	2.95	2.26	622	0.602	153.8	0.353
H	Q	900	19	0.067	Normal	30.3	60	72.3		3.44	3.89	643	0.365	98.0	0.932
H	Q	900	19.25	0.067	Normal	47.1	45	58.1	60	3.38	3.82	669	0.880	146.2	1.199
IP	Q	900	18.5	0.067	Normal	59.7	45	31.7	30	9.42	9.00	617	0.793	156.4	0.268
IP	Q	900	18.5	0.067	Normal	29.1	45	71.1		7.44	6.93	625	0.865	187.0	0.312
H	S	900	4	0.67	Normal	13.6	15	46.4	20	1.81	1.79	610	0.836	181.9	0.264
I	S	900	4	0.67	Normal	18.4	20	24.2	10	6.03	2.88	614	0.513	141.5	0.348
IP	Q	950	20.5	0.013	Normal	56.2	80	93.8		5.57	4.99	632	0.938	229.3	0.224
H	Q	950	18.5	0.067	Normal	51.1	30	33.9	30	7.36	8.97	695	0.793	106.1	1.386

Continued on next page

Catalyst Type	Tube Type	Temp. (°C)	t_{total} (hrs)	Flow (L/min)	Size (nm)	A	B	C	D	E	F	G	H	I	J
H	Q	950	18.5	0.067	Normal	56.8	30	28.9	30	5.37	6.39	684	0.793	110.4	1.300
IP	Q	950	18	0.067	Normal	32.2	30	37.1	90	12.36	12.06	681	0.807	171.1	0.859
IP	Q	950	18.5	0.067	Normal	26.1	30	19.6	45	11.44	11.11	680	0.851	199.0	0.896
H	S	950	4	0.67	Normal	17.2	15	42.5	30	1.81	1.79	637	0.907	153.5	0.962
I	S	950	4	0.67	Normal	16.0	15	67.2	75	7.36	3.77				
I	S	950	4	0.67	Normal	22.4	10	41.9	45	7.60	3.93	662	0.719	181.7	0.765
IP	S	950	4	0.67	Normal	26.3	10	52.5	60	6.60	6.06	659	0.880	217.3	0.535
IP	S	950	4	0.67	Normal	26.3	10	52.5	60	6.60	6.06	659	0.880	217.3	0.535

Table 6: Control-relative Dependent Variable Results Summary															
Catalyst Type	Tube Type	Temp. (°C)	t_{total} (hrs)	Flow (L/min)	Size (nm)	A	B	C	D	E	F	G	H	I	J
I	S	800	4	0.67	Normal	-3.8	-65		-25	2.03	-0.29	45.2	-0.381	0.2	0.237
G	Q	850	5	0.013	Normal	10.4	15	1.8		0.69	0.32	33.3	-0.159	-31.7	0.003
IP	Q	850	5	0.013	<100 μm	-1.4	15	-2.8		0.55	0.07	32.5	-0.094	-35.5	0.129
IP	Q	850	20	0.013	Normal	0.4	0	-14.3				26.8	-0.145	-32.0	0.035
IP	Q	850	4.5	0.013	Normal	7.5	0	3.8		0.79	0.32	39.7	-0.203	-31.0	0.206
IP	S	850	8	0.013	Normal	11.2	180	5.5		2.16	1.50	35.7	0.044	49.0	-0.053
IP	Q	850	18.5	0.067	Normal	27.7	23			2.05	0.99	12.6	-0.070	25.7	-0.028
G	S	850	5	0.67	Normal	6.9	-10	-11.7	-25	1.08	0.54	48.6	-0.452	-40.9	0.090
I	S	850	5	0.67	Normal	-0.9	-15	-5.6	-15	2.35	-0.29	15.4	-0.393	-39.2	
IP	S	850	4	0.67	<100 μm	7.8	0	-4.1	-30	0.68	-0.05	40.1	-0.422	-31.5	0.150
IP	S	850	4.5	0.67	Normal	6.5	0	-2.1	-30	0.93	0.21	52.2	-0.422	-32.9	0.125
IP	Q	900	18.5	0.067	Normal	5.7	-8	-13.8	-30	5.02	4.11	-34.8	0.207	49.6	-0.775
I	S	900	4	0.67	Normal	4.8	5	-22.2	-10	4.22	1.09	4.2	-0.323	-40.4	0.083
IP	Q	950	18.5	0.067	Normal	-24.8	0	-3.0		5.54	3.90	-9.6	0.036	76.8	-0.465
I	S	950	4	0.67	Normal	2.0	-3	12.0	30	5.66	2.06	25.0	-0.188	28.3	-0.197
IP	S	950	4	0.67	Normal	9.0	-5	10.0	30	4.78	4.27	22.0	-0.027	63.9	-0.427

Table 6: Values shown are the differences of the ironsand value and the hematite control value for a given run. Red colour coding indicates the ironsand performed worse than the control, while green indicates better performance. A: Max Conversion Ratio (%); B: t_{max} (min); C: SCA_1 (%); D: $t_{\frac{1}{2}max} - t_{max}$ (min), some runs had no $t_{\frac{1}{2}max}$ value; E: Carbon yield (g C / g Fe); F: Mass carbon (g), one run had a longer runtime than the control; G: TGA Half-temp; H: PXRD Graphitic Degree; I: PXRD Avg Particle Size (nm); J: Raman I_D/I_G Ratio.

4.1 Catalyst Activity and Decay

To determine if New Zealand ironsand in TCMD is more effective at producing hydrogen than the hematite control, gas chromatography data was collected from the exit gas stream of the reaction. Each sample produced a conversion ratio value at the time the sample was taken. Figure 12 shows an example of what this looked like at different flow rates, over a period of 5 hours.

The TCMD process has three distinct phases, as can be seen in Figure 12:

1. Activation - The time period before the conversion ratio reaches maximum
2. Stable Conversion - The period where the conversion ratio remains at or near the maximum value
3. Deactivation - The period where the conversion ratio decreases to zero.

The activation phase is controlled by the reduction of the iron oxide to elemental iron (ferrite) by methane. As the reduction proceeds, more active sites become available for the methane to adsorb to, and its decomposition accelerates. The stable conversion phase and the deactivation phase are controlled by the metal dusting cycle described in Section 2.3. Metal dusting requires that the methane be able to diffuse through the growing graphite layer, decompose, and saturate the crystals within the iron particle with carbon. If this occurs, then the carbon will precipitate within the particle, initiating the dusting process. If the graphite layer becomes too thick for the methane to diffuse to the surface of the iron particle, the particle will be deactivated before it has dusted completely. As a result, the stable conversion period will only persist as long as conditions allow the diffusion of methane to the surface of the iron particle.

Different methods of representing these phases numerically will be used

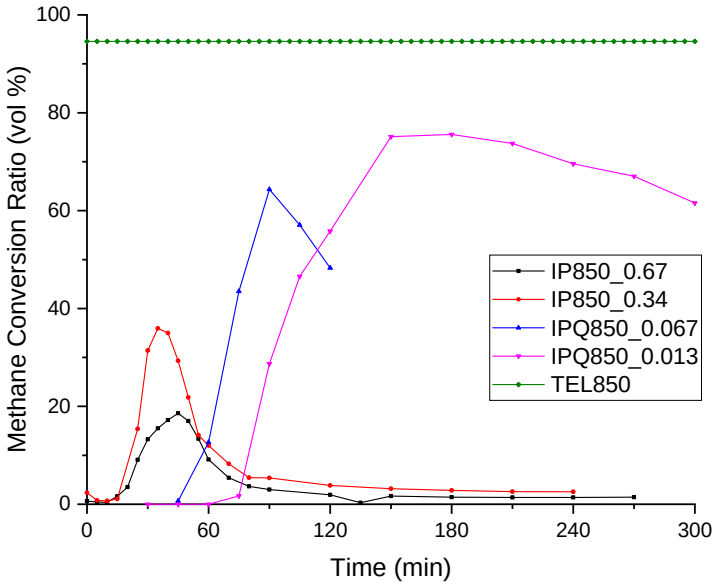

Figure 12: Vol% of CH_4 converted to H_2 at 850 °C over time, by flow rate. IP refers to purified Patea Ironsand, and the CH_4 flow rate in L/min is delimited by an underscore. The experiments were performed in the steel tube reactor, unless the quartz tube is specified by a Q in the series name. TEL850 refers to the Thermodynamic Equilibrium Limit (the maximum conversion %) at 850 °C.

later in this section, so it is important to have an understanding of what the raw data typically looked like. Depending on the flow rate and other factors, the three reaction phases had different durations, and often did not have clear delineations. For example, for the runs shown in Figure 12, at a high flow rate (0.67 L/min), the activation and deactivation phases were pronounced, while the Stable Conversion phase was non-existent. However, at low flow rates (0.013 L/min), the deactivation phase was prolonged, and although not shown on this graph, complete deactivation could take over 20 hours. An ideal catalyst has a long period of stable conversion, and a slow deactivation.

This section uses two metrics for evaluating the activity of the catalyst,

and two metrics for evaluating the decay of that activity. The first metric of activity is the Maximum Conversion Ratio, which is the highest percentage of methane converted to hydrogen at a single moment during a run. For example, in Figure 12, the max conversion ratio for each run is the conversion ratio at the highest point of the curve. The second metric of activity is simply the yield of carbon extracted from the reaction tube at the end of the run. The carbon yield is dependent on the cumulative volume of methane converted across the entire run, so it is a measure of total or cumulative activity.

The first metric of decay is $t_{\frac{1}{2}max} - t_{max}$, which is the time it takes for the conversion ratio to drop from max to half-max. This quantity is equivalent to the Half Width Half Maximum (HWHM) for conversion ratio curves that approach Gaussian, such as those in Figure 12 at 0.67 L/min. The second metric of decay is the Sustained Conversion Average (SCA_t), which is a measure of how the conversion ratio is sustained relative to its maximum value, in a given time period after that maximum value was reached. It is calculated using the following formula:

$$SCA_t = \left(\frac{\overline{X}_{CH_4,t}}{X_{CH_4,max}} \right) \cdot 100 \tag{14}$$

where t is the time elapsed in hours from the time of maximum conversion ratio, $\overline{X}_{CH_4}$ is the mean conversion ratio of CH_4 to H_2 over time period t, and $X_{CH_4,max}$ is the maximum conversion ratio. SCA_t is expressed as a percentage of the maximum value. The higher the value, the lower the decay in catalyst activity, because the average conversion ratio value approaches the maximum. The value of t used in this research was always 1 hour.

It is important to note that the SCA_t metric has limitations, and there was some debate about how best to define it. Because it is constructed by normalising the mean conversion of a run to the maximum for the same

run, the SCA_t will be higher for a run that has consistently low activity, and lower for a run that has a high initial peak which then decays rapidly. This makes SCA_t values meaningless when it comes to comparing catalytic activity. For example, in Figure 12, the SCA_1 value for the red IP850_0.34 run was lower than the SCA_1 value for the black IP850_0.67 run. If the intention had been to define another metric of catalytic activity, the mean conversion ratio ($\overline{X}_{CH_4,t}$) would have been used instead, without any normalisation to the maximum value. However, SCA_t was intended to be a useful measure of decay, not activity. SCA_t immediately provides information on the decay profile, but must be interpreted in conjunction with the max conversion value to allow the absolute activity of the catalyst to be inferred. $\overline{X}_{CH_4,t}$ gives an indication of activity over a given time from max, but must be interpreted in conjunction with the max conversion value to allow the decay profile to be inferred. It was for this reason that SCA_1 was used as a metric of decay.

However, the usefulness of SCA_1 for comparing decay trends was also limited by the data itself. Low sampling rates, particularly for 950 °C runs and 0.067 L/min runs, meant that there were often few or no data points for the hour following the conversion maximum. Any metric that sought to compare these runs with other runs that had richer data in the hour following the maximum was therefore very unreliable. Had there been a larger number of data points following the maximum conversion ratio for all runs, the SCA_1 metric would certainly have proven more useful for comparing the decay of the catalyst under different conditions. Ideally, an auto-sampler and on-stream GC instrument would have been used to create a high resolution conversion ratio plot. In that case, the SCA_1 metric would have provided more reliable information on catalyst decay, and could have been supplemented by SCA_3 and SCA_{10} values for a richer perspective.

To quickly test whether $\overline{X}_{CH_4,t}$ would add additional value as an activity metric, $\overline{X}_{CH_4,1}$ was plotted against the max conversion ratio for each run

(Figure 13a). $\overline{X}_{CH_4,1}$ was quite strongly correlated to the max conversion ratio, with an R^2 value of 0.84. This suggested that there would be limited marginal utility in including $\overline{X}_{CH_4,1}$ as an additional metric of catalyst activity. The correlation between SCA_1 and max conversion ratio is shown in Figure 13b for comparison, with an R^2 value of 0.34.

To evaluate the overall lifetime of the catalyst, a complete deactivation run of Patea ironsand was initially attempted at 0.013 L/min. However, after 20 hrs, the conversion ratio was still 35.6%. As a result, the flow rate was increased by a factor of 5 to 0.067 L/min. Experiments at this flow rate were run for approximately 18.5 hrs. Figure 19 on Page 63 shows a set of complete deactivation runs at 850 °C. Because the gas sampling was done manually, there was a long period overnight where no samples were taken. This caused some metrics of catalyst evaluation to be unreliable or subject to increased error at this flow rate. For example, the sampling period at the beginning of runs at 0.067 L/min was often shorter than for runs at other flow rates, meaning normal metrics of decay like $t_{\frac{1}{2}max} - t_{max}$ weren't always calculable. However, the main purpose of these runs was to weigh the carbon produced and calculate the total yields of C and H_2 from the deactivated catalyst.

Figure 14 compares the hematite control run, H850, with four different types of ironsand, at a CH_4 flow rate of 0.67 L/min. As these runs were all at the same flow rate, the shape and timing of the conversion ratio curves was similar, but it was apparent that the Purified Patea Ironsand (IP850, IP850<100 μm) and the Glenbrook ironsand (G850) had a higher catalytic activity than the hematite control in these conditions. The difference between the maximum conversion ratio of each ironsand run and the maximum conversion of the hematite control is referred to as the control-relative max conversion value. Control-relative values for max conversion ratio and several other key dependent variables are displayed in Table 6. Errors and uncertainty pertaining to all measurements are discussed in Section 4.4.

(a) Correlation between the mean conversion ratio for 1 hour after maximum, and the maximum conversion ratio across all runs. $R^2 = 0.84$.

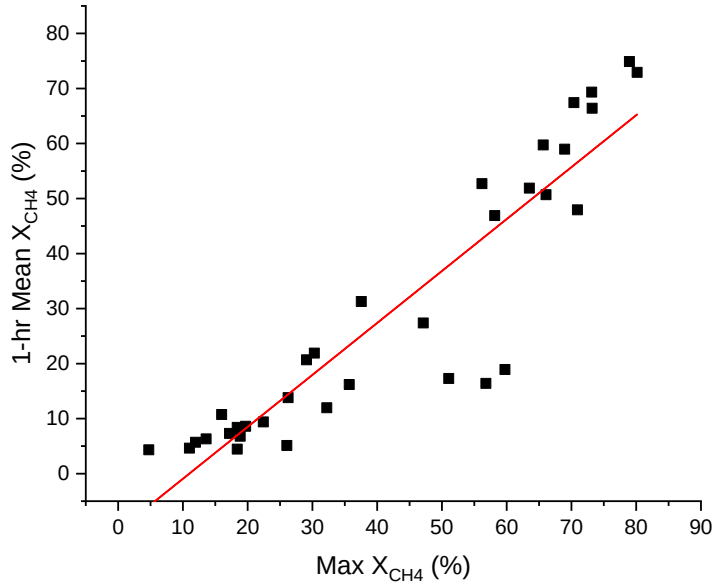

(b) Correlation between the 1 hour sustained conversion average and the maximum conversion ratio across all runs. $R^2 = 0.34$.

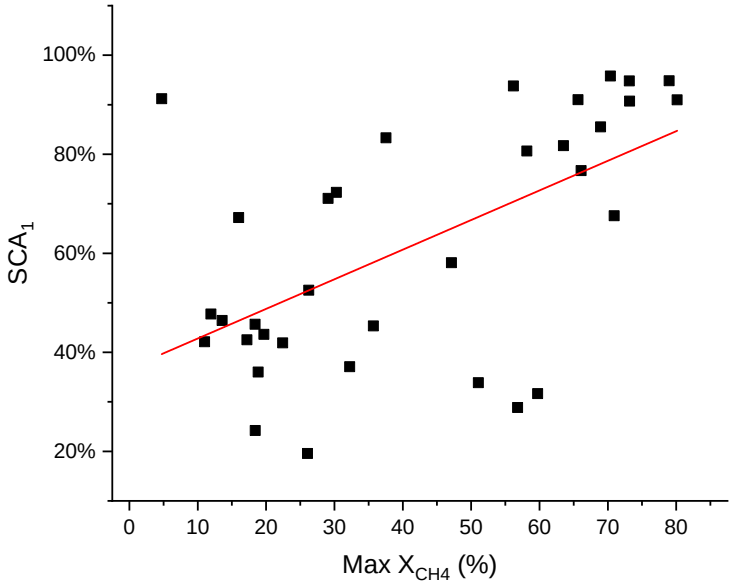

Figure 13

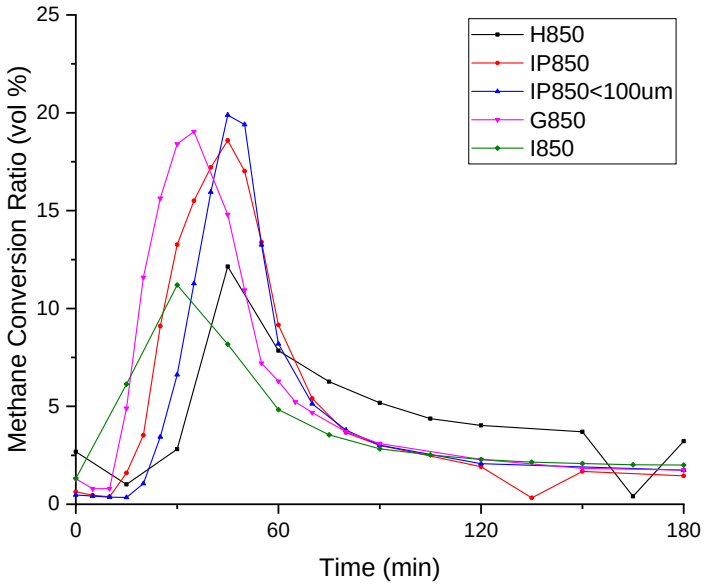

Figure 14: Vol% of CH_4 converted to H_2 at 850 °C over time, by catalyst type. H is the hematite control, IP is Purified Ironsand, G is Glenbrook ironsand, <100 μm refers to the particle size distribution of the sand, and the CH_4 flow rate was 0.67 L/min. The experiments were performed in the steel tube reactor.

4.1.1 Temperature Effects

4.1.1.1 Results

Four temperatures were investigated in this research: 800 °C, 850 °C, 900 °C, and 950 °C. These experiments were done to learn about the behaviour of the ironsands and hematite at different temperatures, with particular interest in any differences in temperature trends between them.

In the literature, 800 °C was identified as being the point below which there is insufficient energy for metal dusting to occur [13]. To confirm this, a run at 750 °C was done, and no reaction was observed. At 800 °C, conversion ratios were low, and the activation of the catalyst took much longer than at higher temperatures, as can be seen with the H800 series on Figure 15. As a

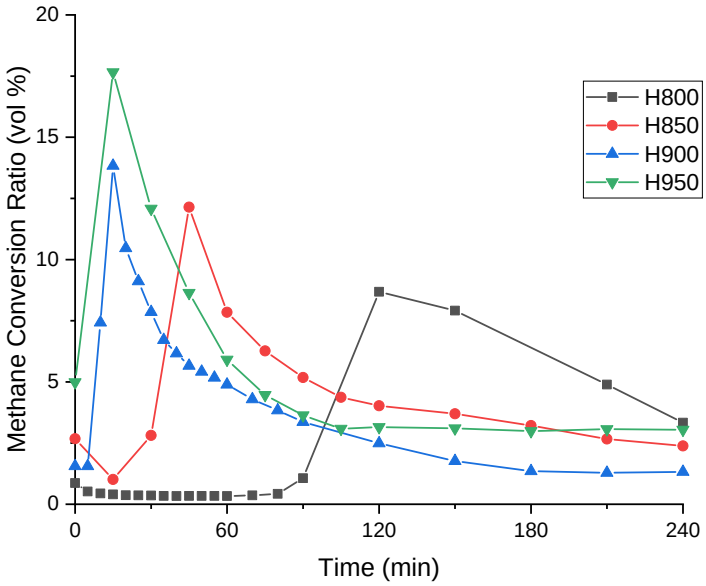

Figure 15: Vol% of CH_4 converted to H_2 of hematite runs, by temperature. 0.67 L/min CH_4 flow rate. H refers to the hematite control. Experiments were performed in the steel tube reactor.

result, no further runs were performed below 850 °C.

Interestingly, on average, an increase in temperature did not always correspond to an increase in maximum conversion ratio. Overall, the highest mean max conversion ratio was 44.4% at 850 °C, but controlling for flow rate and catalyst type (comparing only values with the same flow rate and catalyst type) showed that 850 °C was not a maximum for all conditions. Figure 16a shows how temperature affected the max conversion ratio of each individual catalyst type and flow rate. By comparison, literature max conversion ratio values for hematite at 0.010 L/min were typically around 80% [13]. At low flow rates IP showed a decreasing maximum conversion ratio with increasing temperature. The other runs shown all had higher maximum conversion ratios with increasing temperature.

At 850 °C, ironsand catalysts have a mean max conversion ratio that is 7.61% higher than that of the control. This drops to 5.26% at 900 °C, and at

(a) Maximum conversion ratio trends with temperature.

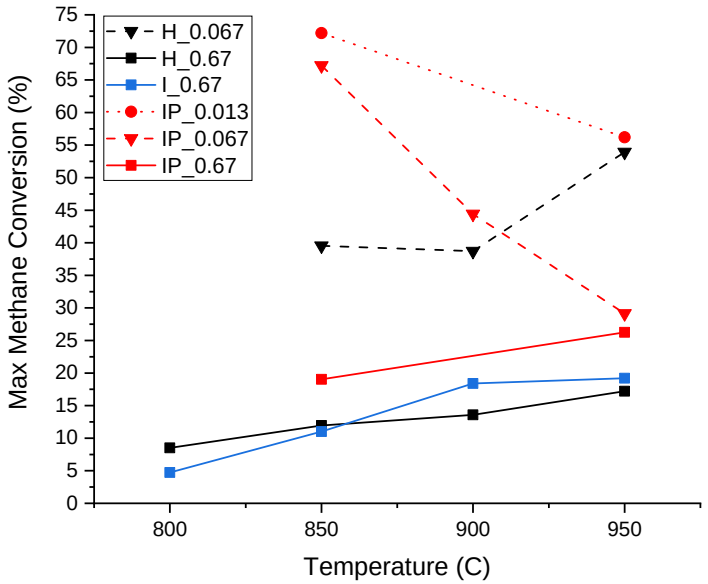

(b) t_{max} trends with temperature.

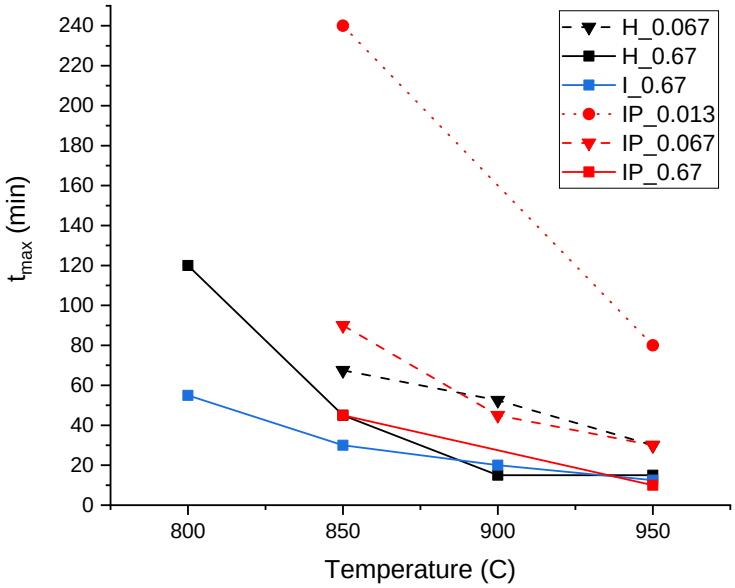

Figure 16: H refers to hematite, I refers to Patea ironsand, IP refers to purified Patea ironsand, and the flow rate in L/min is delimited by an underscore. Only sets of runs that spanned multiple temperatures are shown.

950 °C, the ironsand max conversion ratio mean dropped below the control, with a difference of -4.58%. While absolute conversion ratios for both the ironsand and control increased with temperature, on average, the ironsand increased less than the control. This suggests that increasing temperatures are more favourable to the activity of the control than that of the ironsand.

When this result is broken down by flow rate, it is found that it only holds for runs at 0.067 L/min, where the IP mean relative max conversion ratio at 850 °C was +27.7%, but dropped to -24.8% at 950 °C. At 0.67 L/min, IP at 850 °C had a relative max conversion ratio of +7.1%, and at 950 °C, +9.0%. This suggests that the flow rate could have a significant effect on the optimum temperature for catalytic activity of ironsand, although the results are affected by a low sample size (N).

On average, as the temperature was increased, the maximum conversion value occurred earlier in the run. This holds for each flow rate and for all catalyst types. t_{max} for several different catalyst types and flow rates is plotted against temperature in Figure 16b. t_{max} was lowest at 950 °C for all runs. This was due to the reduction of the iron oxide to elemental iron in the catalyst by CH_4, which proceeds faster at higher temperatures. When averaged across all runs, and taken relative to the control, t_{max} for the ironsand was 21 min later than for hematite at 850 °C, but almost the same at higher temperatures.

Temperature also affected the decay of the catalyst, although there was wide variability in this relationship. Figure 17b shows that temperature trends in $t_{\frac{1}{2}max} - t_{max}$ varied with flow rate and catalyst type. At 0.67 L/min, decay was fastest for both I and H (no data for IP). At 850 °C and 900 °C, ironsand at 0.67 L/min was -25 mins and -10 mins quicker than the control respectively to reach half-max conversion ratio, while at 950 °C the sand lasted longer than the control with a value of +30 mins. Other flow rates did not reach half-max within the sample period, so had missing values that

(a) Conversion ratio data for SCA_1 against temperature.

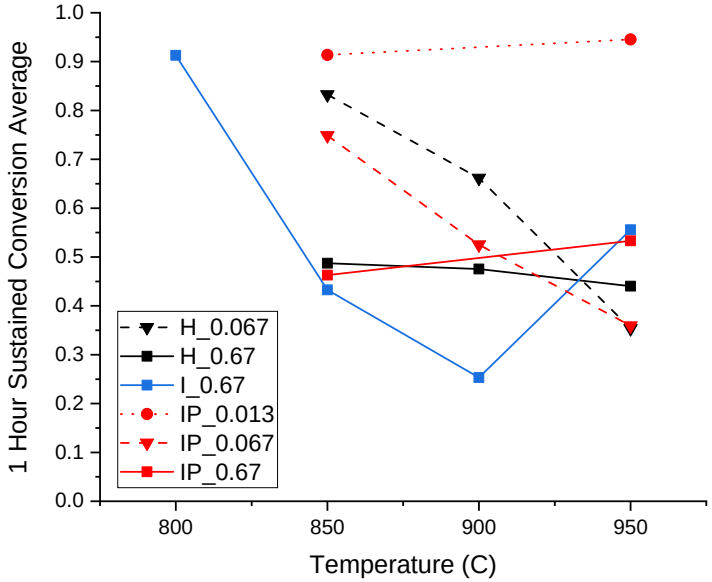

(b) Time for the conversion ratio of a run to decrease from maximum to half its maximum, plotted against temperature.

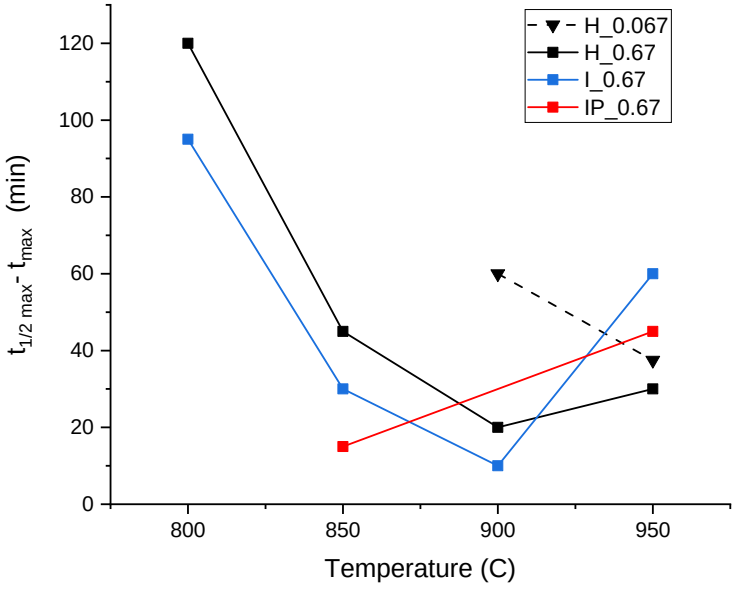

Figure 17: H refers to hematite, I refers to Patea ironsand, IP refers to purified Patea ironsand, and the flow rate in L/min is delimited by an underscore. Only sets of runs that spanned multiple temperatures are shown.

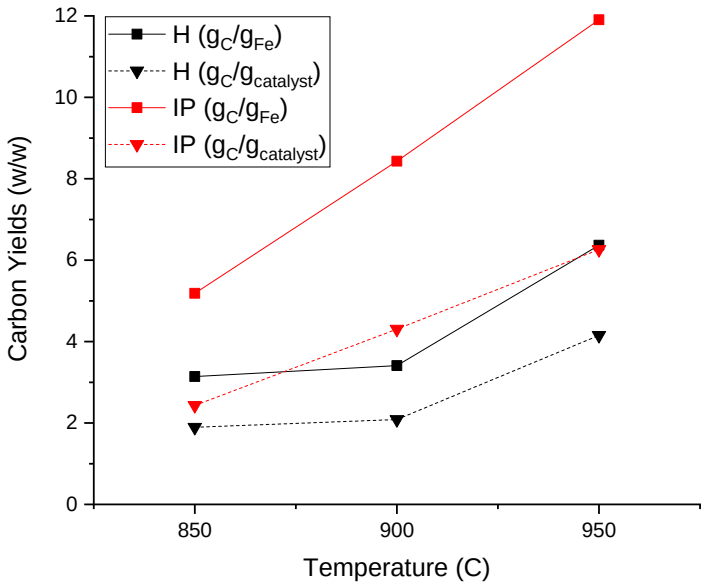

Figure 18: Two measures of carbon production are displayed by temperature: carbon yield per mass of catalyst ($g_c/g_{catalyst}$), and carbon yield per mass of elemental iron in the catalyst (g_C/g_{Fe}). All runs were run to deactivation (18.5 hrs) with a CH_4 flow rate of 0.067 L/min. H refers to the hematite control, IP refers to purified Patea ironsand. Each value is the mean of two duplicates.

prevented them from being compared. For means of I runs only and IP runs only, control-relative $t_{\frac{1}{2}max} - t_{max}$ values increased with temperature for both.

Figure 17a shows that temperature trends in SCA_1 also varied with flow rate and catalyst type. On average, for IP at 0.013 L/min, SCA_1 increases slightly with temperature. For IP at 0.067 L/min, SCA_1 decreases strongly with temperature. For IP at 0.67 L/min, SCA_1 increases with temperature. The mean absolute SCA_1 value is highest at 850 °C and lowest at 900 °C. Breaking this down by catalyst type shows a different trend for each: the highest SCA_1 values for H, I, and IP were at 850 °C, 950 °C, and 850 °C respectively, while their lowest values were at 950 °C, 900 °C, and 900 °C. When the average was taken of all runs at a given flow rate, 0.013, 0.067, and

Table 7: End-of-run conversion ratios of runs at 0.067 L/min, averaged over 1.5 hours, and presented relative to the control. IP refers to purified Patea ironsand.

Table 7: Control-relative Conversion Averaged from 17 to 18.5 hrs		
Sand type	Temperature (°C)	Avg Conversion (%)
IP	850	1.06
IP	900	8.71
IP	950	0.07

0.67 L/min had best SCA_1 values at 950 °C, 850 °C, and 950 °C. However, the SCA_1 values at 850 °C and 0.067 L/min may be artificially high due to low sampling rates (see Figure 19).

Mean control-relative SCA_1 values tentatively suggest that ironsand decays more quickly than the control at 900 °C (SCA_1 of -18.01%), while decaying more slowly at 950 °C (SCA_1 of +6.34%). This trend was the same for each individual catalyst type, and also at 0.067 L/min, where 900 °C had a control-relative SCA_1 of -13.83%, and improved to -3.02% at 950 °C.

Table 7 shows the end-of-run conversion ratio of 0.067 L/min runs using IP as a catalyst, after 18 hours, relative to the control. Each run was duplicated and the mean of the two runs used. For most runs, the catalyst had completely deactivated, but in one run at 900 °C, the ironsand was still converting methane at around 15%.

Figures 19 to 21 show conversion ratio values over time for the complete deactivation runs at 0.067 L/min. Carbon yields from these runs are shown in Figure 18, with a maximum value of 12.36 g_C/g_{Fe} (18 hrs, 0.067 L/min). By comparison, literature yields for complete deactivation of hematite (19 hrs, 0.010 L/min CH_4 flow rate) ranged from 7 to 10 g_C/g_{Fe} [13]. Averaged across all runs, carbon yields increased with temperature for both ironsand and control, and at all temperatures, the ironsand yields were higher than those of the control. Across the means of each individual flow rate and catalyst type,

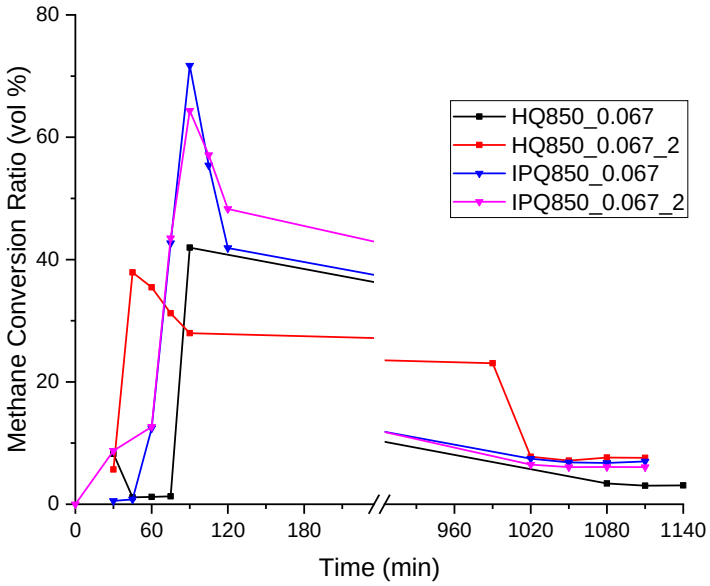

Figure 19: Vol% of CH_4 converted to H_2 at 850 °C over time. 0.067 L/min CH_4 flow rate. IP refers to Purified Ironsand, H is the hematite control, and _2 denotes a duplicate of the other run with the same name. The experiments were performed in the quartz tube reactor.

yields increased with temperature. The overall control-relative mean also showed an increase with increasing temperature. Amongst the completely deactivated runs at 0.067 L/min, the difference between the ironsand and control was highest for $g_C/g_{catalyst}$ at 900 °C with a value of 4.11, and highest for g_C/g_{Fe} at 950 °C with a value of 5.54 (Table 6). In both cases the lowest value was 850 °C. At 0.67 L/min, both $g_C/g_{catalyst}$ and g_C/g_{Fe} increased with temperature relative to the control. This was also the case for I and IP catalyst individual means at that flow rate.

The effects of temperature on catalyst activity and decay are summarised briefly here.

- The activation temperature of the reaction was confirmed to be between 750 °C and 800 °C.
- Max conversion ratio increased with temperature for all catalyst types

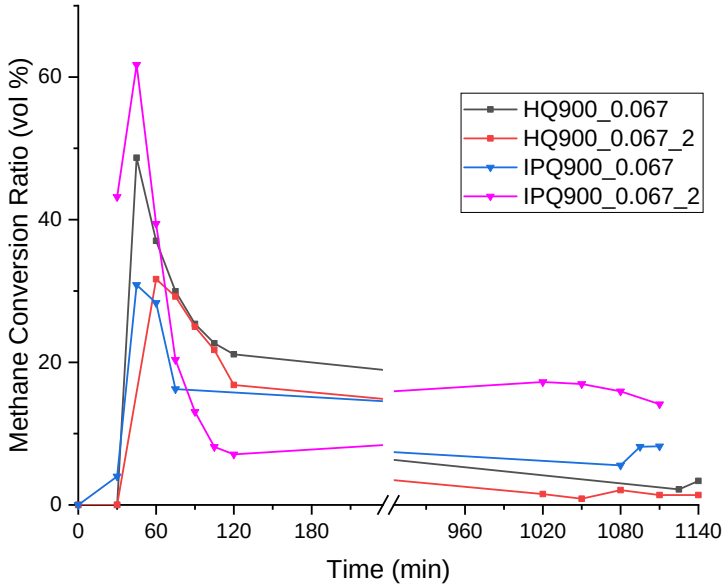

Figure 20: Vol% of CH_4 converted to H_2 at 900 °C over time. 0.067 L/min CH_4 flow rate. IP refers to Purified Ironsand, H is the hematite control, and _2 denotes a duplicate of the other run with the same name. The experiments were performed in the quartz tube reactor.

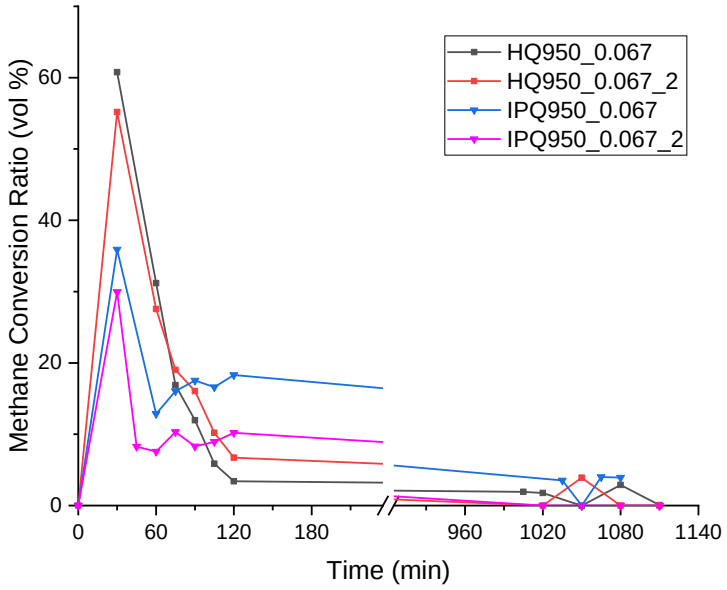

Figure 21: Vol% of CH_4 converted to H_2 at 950 °C over time. 0.067 L/min CH_4 flow rate. IP refers to Purified Ironsand, H is the hematite control, and _2 denotes a duplicate of the other run with the same name. The experiments were performed in the quartz tube reactor.

and flow rates except IP at 0.067 L/min.

- Control-relative max conversion ratios:
  - Decreased with increasing temperature at 0.067 L/min.
  - Increased with increasing temperature at 0.67 L/min.
- Catalyst activation occurred earlier at higher temperatures.
- Control-relative t_{max} was higher at 850 °C, but negligible at higher temperatures.
- $t_{\frac{1}{2}max}-t_{max}$ had unclear trends, although 900 °C showed the fastest decay for I and H at 0.67 L/min.
- Control-relative $t_{\frac{1}{2}max}-t_{max}$ was highest (had the slowest decay) at 950 °C and lowest at 850 °C.
  - Control-relative $t_{\frac{1}{2}max}-t_{max}$ for I and IP increased with temperature.
- SCA_1 was highest on average at 850 °C and lowest at 900 °C.
- SCA_1 for:
  - IP 0.013 L/min increased slightly with temperature.
  - IP 0.067 L/min decreased strongly with temperature.
  - IP 0.67 L/min increased with temperature.
  - H decreased with temperature at all flow rates.
- Control-relative SCA_1 showed faster decay at 900 °C and slower decay at 950 °C. All means of individual catalyst types followed this trend.
- Carbon yield increased with increasing temperature. This held for means of individual flow rates and catalyst types.
- Control-relative carbon yields were higher than the control at all temperatures.
  - Control-relative carbon yields for 0.067 L/min were highest at 900 °C.

4.1.1.2 Discussion

Carbon yields for all runs increased with temperature for all catalyst types and flow rates. This was due to a combination of increasing activity of the catalyst and increasing lifetime of the catalyst at higher temperatures. Yields were comparable to

It was expected that an increase in temperature would also result in higher maximum catalyst activity. Higher temperatures raise the diffusion of methane through the carbon layer, and increase the diffusivity of carbon within the iron particle. The former increases the rate of the dissociation step (Step 2 on Figure 4), while the latter increases the rate of the carbon diffusion step (Step 3 on Figure 4). These are normally the rate limiting steps of the TCMD reaction, so raising the temperature should have raised the reaction rate and observed catalyst activity. The fact that IP did not exhibit this behaviour at low flow rates was unexpected, and requires further investigation to confirm its validity. The 0.067 L/min IP runs were replicated once, and even taking into account the differences between these replicates, the max conversion ratios of these runs still appeared to reduce with temperature. However, the complete deactivation carbon yields of these 0.067 L/min IP runs after 18.5 hrs increased with temperature. The activity of the catalyst at higher temperatures must therefore have been sustained at higher ratios throughout the overnight unsampled period. At high temperatures, then, the maximum activity of the IP must have been limited by the morphologies of carbon being produced, but not enough to prevent metal dusting from occurring. The diffusion of methane through the graphite layer was most likely the rate limiting step that caused the observed decrease in maximum conversion ratio. An additional possibility is that the reduction of the iron particle was limited by the graphite layer, so that the number of active sites available at any one time was lower at higher temperatures.

SCA_1 as a measure of catalyst decay was inversely correlated to carbon yield at 0.067 L/min. This means that while IP and H had higher decay with increasing temperature according to their SCA_1 value, their final deactivated carbon yields were higher. This is the opposite of what the metric was intended to predict, and is due to a combination of low sample rates, lack of overnight sampling preventing a SCA_3 value being used instead, and large drops in conversion ratio immediately after the maximum conversion ratio was reached.

At all temperatures, carbon yields were on average higher than the control, but in particular, the complete deactivation runs at 0.067 L/min showed large differences in carbon quantity between IP and H. This is a positive result, as it suggests that the differences in composition between the ironsand and the hematite are beneficial to carbon production, and thus to catalyst activity and lifetime.

The difference between the carbon yields of ironsand and the hematite control increased with temperature at 0.67 L/min and 0.067 L/min. This suggests that there is a fundamental difference in the metal dusting behaviour of the two catalysts due to their compositions. This research was not a metal dusting study, but it would be useful to investigate this specifically to determine the reason for the different temperature interactions.

Overall, increasing the temperature caused higher carbon yields for all catalyst types and flow rates, but improved IP yields more than it improved H yields. Higher temperatures also caused higher maximum conversion ratios for all except IP at 0.067 L/min.

4.1.2 Flow Rate Effects

4.1.2.1 Results

Studying a range of methane flow rates was intended to provide information on how the catalysts would perform as part of an industrial process. It was also necessary to vary the flow rate simply to obtain complete deactivation data and find the catalytic activity limits of the sand.

An example of the effect of flow rate on hydrogen production in TCMD can be seen in Figure 12. On average, lowering the flow rate while keeping the initial mass of the catalyst constant increased the methane conversion ratio. This trend holds for all individual means of temperature, runtime, and catalyst type.

There is a limit to the number of moles of CH_4 a given quantity of catalyst can convert to H_2 per minute. As a result, any flow of CH_4 above the maximum possible rate of conversion is wasted, and artificially lowers the observed vol% conversion ratio. If the flow of CH_4 drops below the maximum capacity of the catalyst, no further increase in conversion ratio will be observed. However, Figure 22 shows that maximum rates of H_2 production decreased for lower flow rates. This is because, while low flow rates gave a high conversion ratio, the volume of CH_4 interacting with the catalyst was much lower.

The advantage of low flow rates was that the catalyst had a much longer stable period of high conversion. This resulted in higher total H_2 yields by the time the catalyst had deactivated. Figure 23 shows total, end-of-run H_2 yield values for complete deactivation runs at 850 °C. These yield values were calculated from the mass of carbon weighed out at the end of the run. Despite the higher maximum H_2 production rates at 0.67 L/min, higher overall yields of carbon were obtained over a longer duration at 0.067 L/min. Mean produced carbon mass was 2.91 g for 0.67 L/min runs, and 6.52 g for

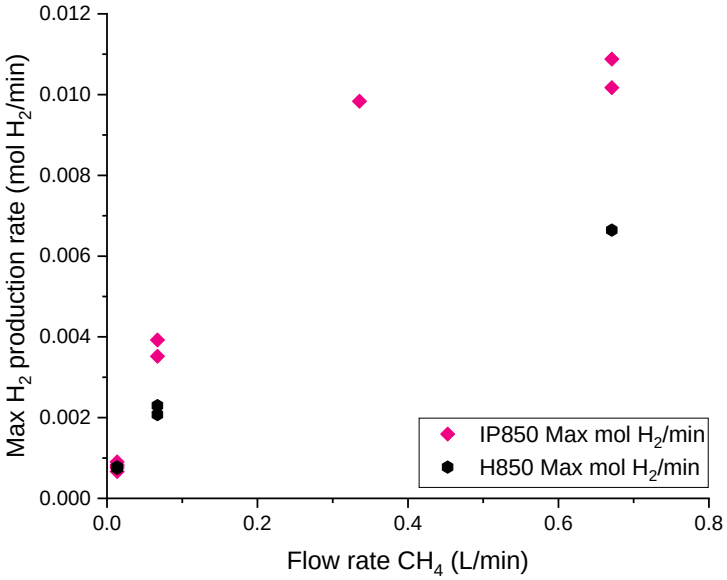

Figure 22: Maximum H_2 production rate of Purified Patea Ironsand and Hematite control at 850 °C, plotted against flow rate.

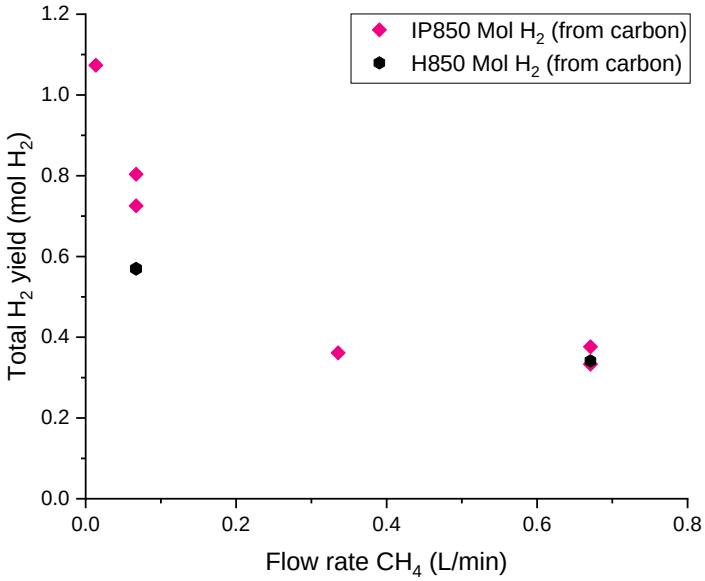

Figure 23: Total H_2 yields of Purified Patea Ironsand and Hematite control at 850 °C, plotted against flow rate. Runs that were not completely deactivated are excluded, with the exception of one 0.013 L/min run which is included as it was still active after 20.5 hrs.

0.067 L/min runs. This shows that lowering the flow rate increased the total yield of the catalyst. Relative to the control, 0.67 L/min had a carbon mass of +0.96 g, and 0.067 L/min, +3.23 g. At all temperatures, 0.067 L/min had a higher control-relative carbon mass than 0.67 L/min. This suggests that lowering the flow rate improves the carbon production of ironsand more than it does for hematite.

Experiments at 0.67 L/min were run to deactivation in a period of 4-5 hrs, and 0.067 L/min were run to deactivation overnight for a duration of 18.5 hours, but runs at 0.013 L/min were not. The IP 950 °C runs at 0.013 L/min (20.5 hr duration) and 0.067 L/min (18.5 hrs) produced 4.99 g and 11.58 g of carbon respectively (Table 5). However, the 0.013 L/min run in this case still had a conversion ratio of about 40% after 20.5 hrs, so once run to deactivation it may have resulted in a higher yield.

On average, runs at all flow rates had higher maximum conversion ratios than their respective hematite controls. 0.013 L/min performed the best relative to the control with a mean difference of +5.64%, while 0.067 L/min performed the worst, with a mean difference of +2.87%. Table 6 shows the individual runs that make up these means, and Figures 20 and 21 show examples of hematite runs with higher maximum conversion ratios than the ironsand at 0.067 L/min. These runs are responsible for lowering the relative mean at this flow rate. When the global mean was segmented by temperature, 0.067 L/min performed the best relative to the control at 850 °C and 900 °C, while 0.67 L/min performed the worst at those temperatures. At 950 °C, 0.067 L/min had a lower max conversion ratio than the control by -24.8%, while 0.67 L/min remained the same as the previous two temperatures at $\approx$ +5%.

Decreasing flow rate caused an increase in time to maximum (t_{max}) from 49.2 mins at 0.67 L/min on average to 90.4 mins at 0.013 L/min. Despite several outliers, this trend holds across temperatures and catalyst types.

Next, control-relative t_{max} data is considered. At 0.013 L/min, the ironsand took significantly longer on average to reach its maximum value than the control (45 mins). The other flow rates had smaller average differences. Table 6 shows that three of the runs at 0.013 L/min were slower to reach maximum than their controls, while the remaining two were identical to the controls (differences of 0). A single run, IP850_0.013, took 180 mins longer to reach maximum than the control. This run was not replicated and so this value may be subject to error, as discussed in Section 4.4. However, even disregarding this value, it is clear that lower flow rates resulted in longer t_{max} values than the control. This held true for each individual temperature and catalyst type mean. One thing that could cause this discrepancy is a difference in reduction times between the ironsand and the control. Reduction of the iron oxides in ironsand to elemental iron activates it as a catalyst for TCMD, so it must occur first. If this was slow, less of the iron from the sand would have been active and available to convert methane to hydrogen [30]. This effect would be more pronounced at low flow rates.

Next, the effect of flow rate on the deactivation phase of the catalyst was considered. On average, $t_{\frac{1}{2}max}-t_{max}$ increased with decreasing flow rate. This held true for all temperatures except 950 °C, where 0.67 L/min had a higher $t_{\frac{1}{2}max}-t_{max}$ value than 0.067 L/min (0.013 L/min lacked data at that temperature). This was also the case for H and IP means. However, this was skewed by the fact that 0.013 L/min and 0.067 L/min runs sometimes did not reach $\frac{1}{2}max$ within the sample period, causing missing values which can be seen in Table 5. This source of error also makes relative mean values for $t_{\frac{1}{2}max}-t_{max}$ unreliable for those flow rates, so they cannot be compared. At 0.67 L/min, the ironsand had a control-relative $t_{\frac{1}{2}max}-t_{max}$ of -9.4 mins.

On average, SCA_1 increased as the flow rate decreased. 0.013 L/min had a mean SCA_1 of 90.4%. 0.067 L/min and 0.67 L/min were very similar in mean SCA_1, with values of 50.2% and 49.2% respectively. When these

means were broken down, the general trend held for all temperatures and catalyst types. Control-relative means for SCA_1 were lower for all flow rates. 0.013 L/min was the highest, with -1.21%, 0.067 L/min was the lowest, with -8.42%.

A brief summary of the effects of flow rate on catalytic activity and decay is given here.

- Max conversion ratio increased with decreasing flow rate.
- Control-relative max conversion ratio was highest at 0.013 L/min and lowest at 0.067 L/min.
- The control-relative max conversion ratio
  - at 0.067 L/min was highest at 850 °C and 900 °C, and significantly lower at 950 °C.
  - at 0.67 L/min was lowest at 850 °C and 900 °C, and showed no difference at 950 °C.
- Carbon yields were higher for lower flow rates under all conditions.
- Control-relative carbon yields were higher for low flow rates, at all temperatures.
- t_{max} increased with lower flow rate, at all temperatures and across all catalyst types.
- Control-relative t_{max} values were higher at low flow rates.
- $t_{\frac{1}{2}max} - t_{max}$ increased with decreasing flow rate, except at 950 °C, where 0.67 L/min was higher than 0.067 L/min.
- SCA_1 increased with lower flow rates, although 0.013 L/min was considerably better than the other two flow rates.
- Control relative SCA_1 means were negative for all flow rates, with 0.013 L/min the least negative, and 0.067 L/min the most negative.

4.1.2.2 Discussion

Methane max conversion ratios and carbon yields increased with decreasing flow rate. This is because, at low flow rates, the residence time of methane in the reactor was sufficient to allow metal dusting to occur, while at a high flow rate, it was not. In both cases, the methane adsorbed to the surface of the catalyst particle and formed cementite in the surface region until the region was saturated, precipitating graphite. At low flow rates, this initial graphite shell was enough to slow the diffusion of methane to the surface, allowing time for carbon to diffuse deeper into the iron crystal. This led to saturation of the whole crystal and then to metal dusting (See Section 2.3). However, at a high flow rate, there was less time for the methane to diffuse across the graphite shell. This meant that a graphite shell thickness that might have allowed or even promoted metal-dusting at a low flow rate, instead caused deactivation of the catalyst at a high flow rate. Very little metal-dusting occurred at 0.67 L/min, resulting in low carbon yields and a rapid decay of conversion ratio, as shown on Figure 12.

4.1.3 Catalyst Composition and Particle Size Effects

Different sand types were compared to see if differences in composition influenced their performance. This was to inform potential future commercial decisions about the where to source the ironsand from, and to determine the importance of magnetic purification.

Ironsand from two sources was used in this research: Patea ironsand, and Glenbrook ironsand. As shown in Table 3, unpurified Patea ironsand (I) contained 52.0% Fe_2O_3 and 4.8% TiO_2, purified Patea ironsand contained 80.5% Fe_2O_3 and 7.44% TiO_2, and Glenbrook ironsand contained 83.8% Fe_2O_3 and 7.77% TiO_2. The iron oxide values are given as % of hematite due to pre-oxidation that was required before the XRF analysis could be done.

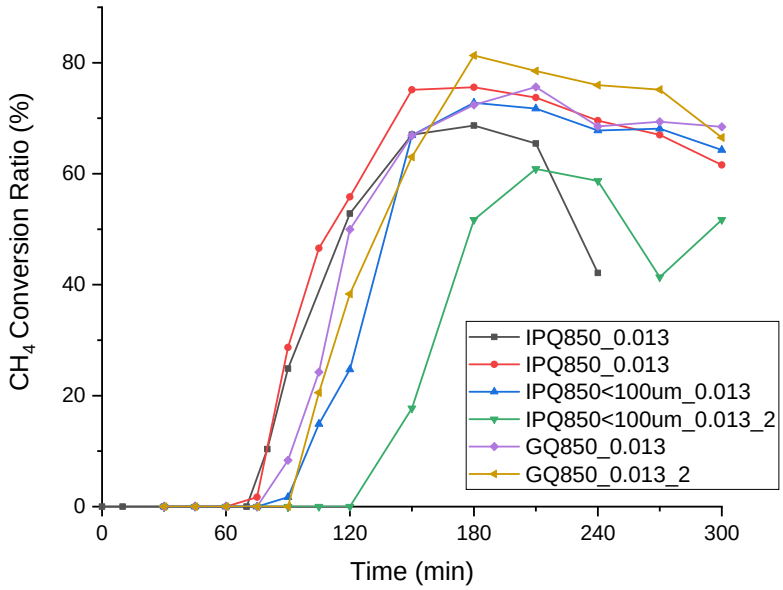

Figure 24: Vol% of CH_4 converted to H_2 at 850 °C over time, by catalyst type. IP is Purified Ironsand, G is Glenbrook ironsand, <100 μm refers to the particle size distribution of the sand, and the CH_4 flow rate was 0.013 L/min. The experiments were performed in the quartz tube reactor.

Figure 14 (Page 56) provides a comparison of the different catalyst types at 850 °C and a 0.67 L/min. At this flow rate, Glenbrook ironsand had a higher maximum conversion ratio than IP, but after adjusting for the 3.3% difference in iron oxide content, this difference disappeared. This was also the case for carbon yield and for all variables at 0.013 L/min. The Glenbrook sand reached max conversion 10 minutes faster and decayed to half-max 5 minutes slower than the purified Patea ironsand, but its SCA_1 was 0.10 lower.

A comparison between the Glenbrook and purified Patea ironsands at 0.013 L/min is shown on Figure 24. Averaged across two duplicates, there is no significant difference between the conversion profiles of the two types of sand. The carbon yields after 5 hours are also the same.

Overall, there is no significant difference between the Glenbrook and puri-

fied Patea sands that is not explainable by correcting for the small difference in iron content.

The difference between the purified and unpurified Patea ironsand was much greater than for the Glenbrook sand. As expected, the lower iron content in I resulted in far lower maximum conversion ratios than IP. At 0.67 L/min, the max conversion ratio of I was 7.4% lower than IP at 850 °C, and 7.0% lower at 950 °C. At 850 °C, t_{max} was shorter for I, it decayed to half maximum slightly slower, but had an SCA_1 3.5% lower than IP. At 950 °C, the unpurified Patea ironsand had a $g_C/g_{catalyst}$ of 2.08, while the purified ironsand had a $g_C/g_{catalyst}$ of 3.27. However, the mass of iron per weight of catalyst was considerably lower in the unpurified sand. This meant that the g_C/g_{Fe} value for I (7.48) was higher than that of IP (6.60). This shows that, at 0.67 L/min, the weight percentage of iron did not have a proportional effect on carbon yields. However, because of the lower maximum conversion ratios of I, use of I in experiments was stopped and no experiments were run with it at lower flow rates.

A 100 μm sieve was used to reduce the size distribution of a sample of purified Patea ironsand. Figure 24 shows the effects of this at 0.013 L/min and 850 °C. The <100 μm ironsand had a lower max conversion ratio and lower carbon yield after 5 hours than ironsand with an unaltered PSD under the same conditions (Table 5). t_{max} was 45 min shorter for the <100 μm sand, but there was no appreciable difference in catalyst decay (-0.03 in SCA_1). At 0.67 L/min and 850 °C, the <100 μm ironsand had a slightly higher maximum conversion ratio (shown in Figure 14), and showed no difference in t_{max}, decay or carbon yield.

Every effort was made to obtain hematite of a larger size, but unfortunately the university could find no high-purity source. As a result, no empirical information was obtained about the performance of hematite with a larger aggregate size. This limited the effectiveness of hematite as a baseline

comparator in this research.

A brief summary of the effects of carbon composition and aggregate particle size is given here.

- Glenbrook sand showed no significant difference to IP.
- At 0.67 L/min, I had a higher g_C/g_{Fe} despite producing a lower carbon mass.
- At 0.013 L/min and 850 °C, <100 μm IP had:
  - Lower max conversion than normal IP.
  - Shorter t_{max} by 45 mins than normal IP.
  - -0.03 SCA_1 compared with normal IP.
  - Lower carbon yield than normal IP.
- At 0.67 L/min and 850 °C, <100 μm IP had:
  - Slightly higher max conversion than normal IP.
  - The same t_{max}, decay, and carbon yield as normal IP.

4.2 Carbon Quality

To evaluate the quality of the carbon produced in this research, the carbon was characterised using Raman Spectroscopy, PXRD, and TGA. A high TGA half-temp value indicates a higher thermal stability of the carbon, which tends to indicate a more graphitic sample. A high PXRD graphitic degree (GD) value indicates that the layer spacing of the carbon sample approaches that of ideal graphite. A high PXRD average particle diameter (Avg PD) indicates that the average size of the crystal regions within the carbon sample is large, meaning that the carbon is more graphitic. A low Raman I_D/I_G ratio indicates that the carbon sample has low disorder, and is therefore a higher quality graphite lattice. These characterisation methods are discussed in detail in Section 3.2.3. In this section, these characterisation techniques are used to evaluate the effects of temperature, flow rate, catalyst type, and

aggregate particle size on carbon quality.

4.2.1 Temperature Effects

4.2.1.1 Results

The temperature of the reaction chamber had a significant effect on the graphitic nature of the carbon produced by an experiment. The effect of temperature on the global mean values of each individual metric of carbon quality is considered first, accompanied by figures displaying trends in all subcategories of data that contained comparable measurements at more than one temperature. Subcategories that contained measurements at only one temperature, such as runs done with Glenbrook ironsand, are not displayed, but are still included in global means. Next, these global means are broken down into catalyst type and flow rate effects, to understand the influence these factors have on the optimum temperature for carbon quality. Lastly, the effect of temperature on the quality of carbon relative to the control is discussed.

Figure 25 shows how the TGA half-temp of carbon from a subset of runs increases with temperature. The mean TGA half-temp across all runs, not just those shown on the graph, was 603.8 °C at 850 °C, 625.1 °C at 900 °C, and 660.0 °C at 950 °C.

Figure 26 shows how the graphitic degree of carbon varies with temperature. The mean GD across all runs was 0.78 at 850 °C, 0.70 at 900 °C, and 0.85 °C at 950 °C. The minimum at 900 °C suggests that the carbon produced at this temperature is less graphitic.

Figure 27 shows a trend in hematite towards lower crystal sizes at higher temperatures, while the ironsand runs show an increase at 950 °C. Avg PD values averaged across all runs again identify 900 °C as a minimum for carbon quality. The mean PD across all runs was 172.5 nm at 850 °C, 154.3 nm at

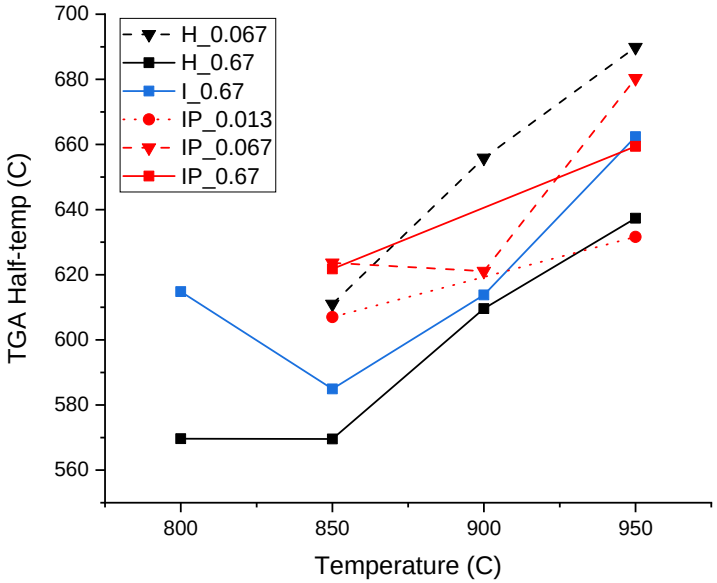

Figure 25: TGA half-temperature of runs with different flow rates and catalyst types, by temperature. I refers to Patea ironsand, IP refers to purified Patea ironsand, H is the hematite control, and the flow rate in L/min is delimited by an underscore.

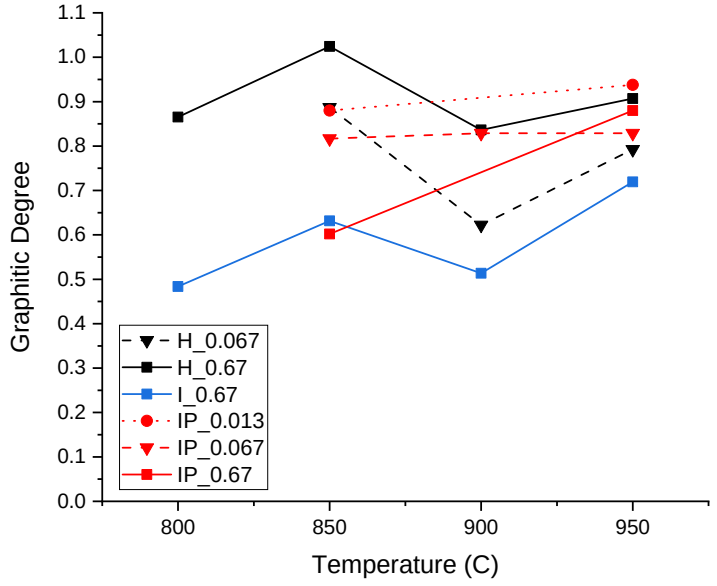

Figure 26: PXRD Graphitic Degree of runs with different flow rates and catalyst types. I refers to Patea ironsand, IP refers to purified Patea ironsand, H is the hematite control, and the flow rate in L/min is delimited by an underscore.

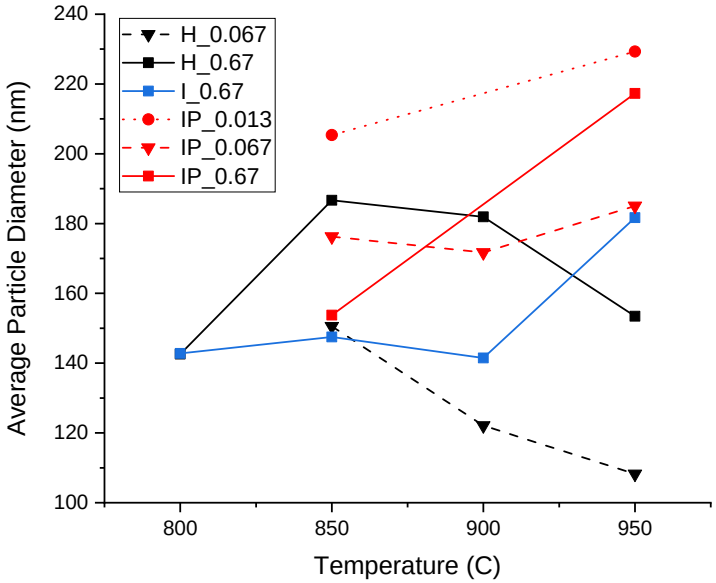

Figure 27: PXRD Average particle diameter of runs with different flow rates and catalyst types. I refers to Patea ironsand, IP refers to purified Patea ironsand, H is the hematite control, and the flow rate in L/min is delimited by an underscore.

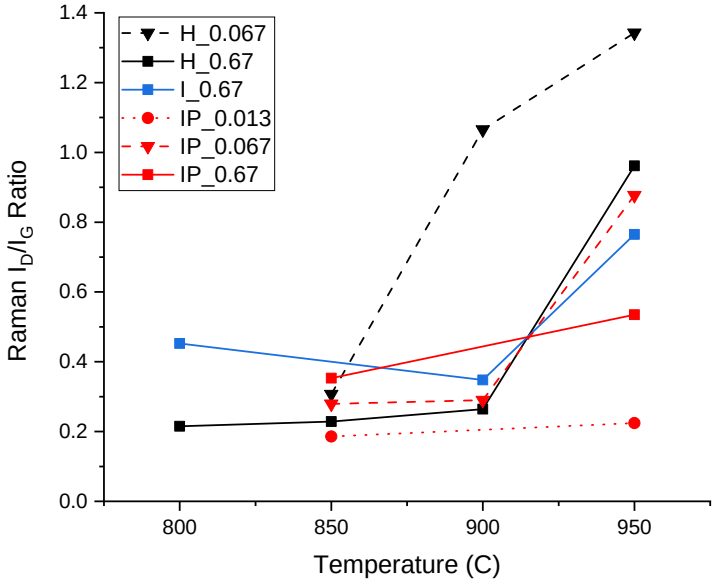

Figure 28: Raman I_D/I_G ratio of runs with different flow rates and catalyst types. A low value is favourable. I refers to Patea ironsand, IP refers to purified Patea ironsand, H is the hematite control, and the flow rate in L/min is delimited by an underscore.

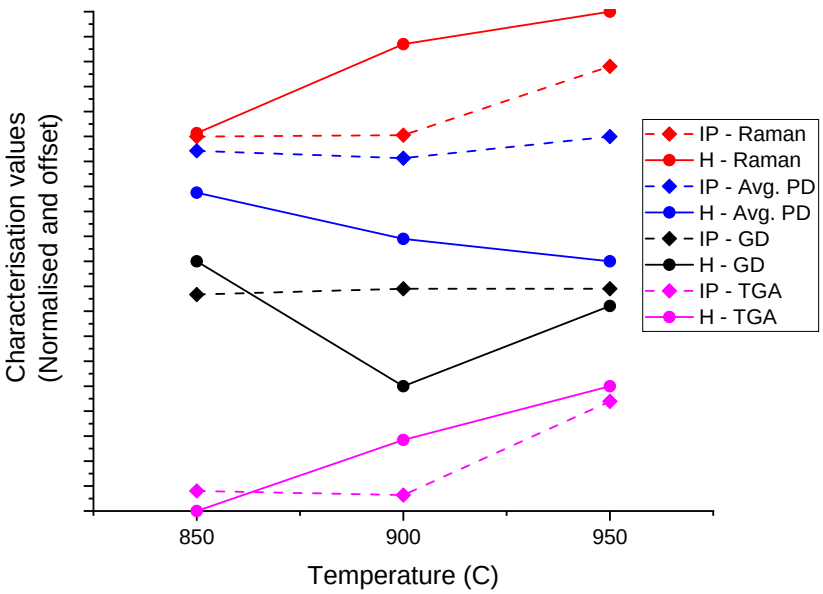

Figure 29: Trends in 0.067 L/min H and IP carbon characterisation values by temperature. Values are normalised to 1 and offset by 1. For all metrics except Raman I_D/I_G ratio, a higher value indicates improved carbon quality.

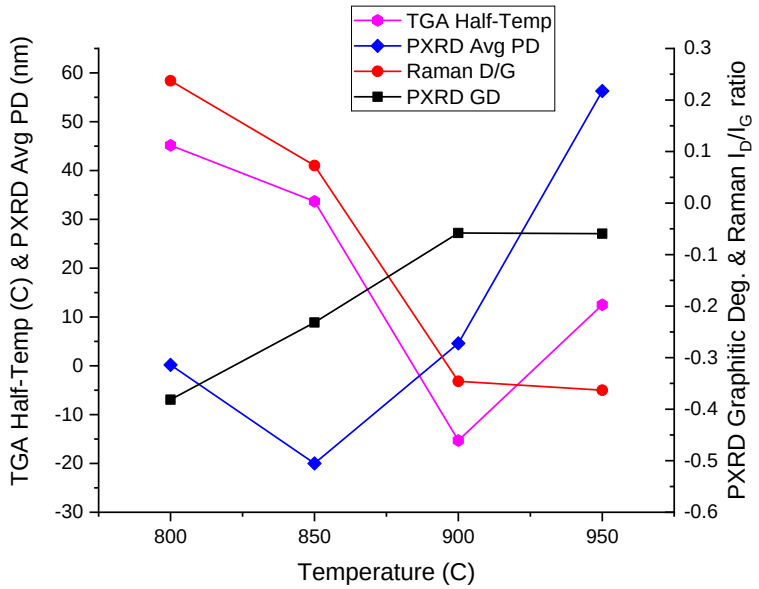

Figure 30: Mean control-relative carbon characterisation data by temperature. For all metrics except Raman I_D/I_G ratio, a higher value indicates improved carbon quality. Note: these values are not absolute, they are useful only for comparing ironsand to the control.

900 °C, and 184.6 nm at 950 °C.

Figure 28 shows a general increase in disorder with temperature, with particularly high Raman I_D/I_G ratios at 950 °C. The mean I_D/I_G ratios across all runs confirmed this, with a value of 0.29 at 850 °C, 0.49 at 900 °C, and 0.75 at 950 °C. At 0.067 L/min, the I_D/I_G ratio was lowest at 850 °C for both H and IP. At 900 °C, the IP value remained low, but the H value increased sharply. At 950 °C, the IP also increased sharply, while the H value remained high.

When the global mean is split out by catalyst type, the same result is found for the I and IP catalysts: 950 °C favoured by all except Raman. For H, TGA favoured 950 °C, but the other three metrics favoured 850 °C for highest carbon quality. This is important, as it shows that the ironsands and control behave very differently at different temperatures.

Breaking down the mean by flow rate also yields interesting results. At 0.013 L/min, all four metrics favour 950 °C. At 0.067 L/min, TGA favoured 950 °C, but the three other metrics favoured 850 °C. At 0.67 L/min, TGA, GD, and Avg PD favoured 950 °C, but Raman strongly favoured 900 °C (0.31 at 950 °C to 0.70 at 900 °C). Figure 29 shows the trends in all carbon quality metrics with temperature for H and IP at 0.067 L/min. It should be noted that the decrease in hematite GD at 900 °C on this graph was the mean of two duplicates with an extremely large difference between them. One of the two runs had a GD of 0.36, while the other had a GD of 0.88. If the low value is removed, the temperature trend of H GD matches that of IP under the same conditions.

Figure 30 shows how the control-relative carbon characterisation data changes with temperature. At 800 °C, there was only a single sample, which had less graphitic carbon than the control according to the Raman I_D/I_G ratio and PXRD Graphitic Degree. The PXRD Avg PD value was slightly positive, and the TGA half-temperature was significantly increased relative

to the control, both of which provide a contrary indication to the other two metrics, although the importance of the TGA value is uncertain. In all, the characterisation data seems to suggest poorer quality carbon than the control at this temperature.

At 850 °C, all metrics except TGA showed less graphitic carbon than the control, although the Raman and PXRD GD values showed some improvement from 800 °C. At 900 °C, TGA and GD were worse than the control, but Avg PD and Raman were better. At 950 °C, TGA improved, GD remained slightly negative, and Avg PD and Raman were better than the control. Across all temperatures, a decreasing Raman I_D/I_G trend, coupled with an increasing PXRD Graphitic Degree trend, suggests that ironsand-produced carbon improves in quality more than the control does with increasing temperature. The largest positive difference between the ironsand and control was at 950 °C for all metrics except TGA.

A brief summary of the effects of temperature on carbon quality is given here.

- Absolute mean TGA increased with increasing temperature.
- On average, PXRD graphitic degree was highest at 950 °C and lowest at 900 °C.
- On average, PXRD Avg PD was highest at 950 °C and lowest at 900 °C.
- On average, Raman I_D/I_G ratio worsened (increased) with increasing temperature.
- I and IP produced high quality carbon at 950 °C according to all measures except Raman.
- For H, TGA favoured 950 °C, while the other three metrics favoured 850 °C for best carbon quality.
- At 0.013 L/min, all metrics favoured 950 °C.
- At 0.067 L/min, TGA favoured 950 °C, while the other three metrics

favoured 850 °C.

- At 0.67 L/min, TGA, GD, and Avg PD favoured 950 °C, but Raman favoured 900 °C strongly.
- At 850 °C all metrics except TGA were worse on average than the control.
- At 900 °C, TGA and GD means were worse than the control, but Avg PD and Raman means were better than the control.
- At 950 °C, TGA, Avg PD, and Raman were all better than control, but GD was slightly negative.
- The largest positive control-relative difference for each metric was at 950 °C.

4.2.1.2 Discussion

In several cases, the different metrics of carbon quality give conflicting indications of optimum temperature. TGA and Raman indicate that 850 °C is the least favourable temperature, while PXRD GD and Avg PD point to 900 °C. According to TGA, GD, and Avg PD, the most favourable temperature was 950 °C, but the Raman data mean indicates that it produces the highest level of disorder. One possible reason for this is that due to the high visible light absorbance of carbon, Raman spectroscopy only characterised the surface of the carbon sample. As discussed in Section 2.3, at high temperatures, non-catalytic methane pyrolysis causes amorphous carbon to deposit on the surface of the catalyst, sometimes deactivating it prematurely. In that case, the amorphous carbon would make up the outer layers of the carbon shell, resulting in higher Raman I_D/I_G estimates of disorder.

The hematite and ironsand showed different trends in carbon quality with temperature. Figures 27 and 28 show that for PXRD Avg PD and Raman, some IP runs showed an increase in carbon quality at 950 °C, but H showed a decrease. Figure 26 shows that for H, the PXRD graphitic degree of carbon

was higher at 850 °C than 950 °C. Lower quality carbon was observed at higher temperatures for hematite, but not for IP.

Figure 29 shows the trends in 0.067 L/min H and IP carbon quality with temperature. The Raman data from these runs suggests that amorphous carbon appeared at lower temperatures for H than for IP. This suggests that the production of this type of carbon is not independent of the presence of a catalyst, as would be the case for methane pyrolysis. One possibility is that the carbon produced by the catalytic reaction was itself acting as a catalyst for further methane decomposition. Carbon catalysts for TCMD are well-represented in the literature, and were discussed briefly in Section 2.2.1. They have an activation energy higher than metal catalysts but lower than pyrolysis. Figure 7 shows that in a review of the literature, carbon catalysts produced both turbostratic carbon and carbon filaments. Amorphous carbon is more catalytically active than highly structured carbon [42]. If the carbon produced by the hematite runs at 900 °C and 0.067 L/min was of a type that was catalytically active for TCMD, it would explain the sudden spike in Raman-observed disorder at that temperature. There is no sign of this process occurring for IP, which could mean that the carbon produced was of a less catalytically active morphology. For IP at 0.067 L/min, all metrics of carbon quality showed similar or better quality with increasing temperature. H showed either a smilar or worse quality according to Avg PD and GD with increasing temperature (taking into account the duplicate error mentioned in the previous section).

The fact that TGA increased with temperature across all catalyst types and reaction conditions conflicts with the observed trends in all other metrics of carbon quality. The reason for this is not known, but it is possible that higher temperatures affected the carbon in some way that caused higher carbon burn-off temperatures, but did not reflect the graphitisation of the sample. TGA was found to be a poor predictor of carbon quality, due to its

low correlation with other techniques. The literature reports broad threshold TGA half-temperatures which were indicative of changes in carbon quality, but no examples of comparative TGA use of the kind carried out in this research have been found.

Overall, it is clear that the ironsand produces the highest quality carbon at high temperatures. This is not the case for the hematite control, which decreased in carbon quality at high temperatures.

4.2.2 Flow Rate Effects

4.2.2.1 Results

Flow rate experiments were an important contributor to understanding how the catalysts might behave in a larger scale system. The methane flow rate caused significant changes in produced carbon quality for all catalyst types, but particularly for purified Patea ironsand.

In terms of global means, TGA favoured 0.067 L/min for best carbon quality, while GD, Avg PD, and Raman favoured 0.013 L/min. The worst carbon quality was produced at 0.013 L/min according to TGA, 0.034 L/min according to GD (although N = 1 for this flow rate), and 0.067 L/min according to Avg PD and Raman.

Next, and more usefully, these means are broken down by reaction temperature. At 850 °C, 0.067 L/min had the highest TGA half-temp, but the other three metrics favoured 0.013 L/min. At 900 °C, only 0.067 and 0.67 L/min were measured, and N = 2 for each flow rate. TGA and GD were highest at 0.067 L/min, but Avg PD and Raman were best at 0.67 L/min. At 950 °C, TGA was highest at 0.067 L/min, but the remaining three metrics were best at 0.013 L/min.

Next, these means are broken down by catalyst type. Only H and IP were run at multiple flow rates under comparable conditions. For H, TGA

was highest at 0.067 L/min, and the other three were best at 0.013 L/min. The worst flow rate for H was 0.013 L/min according to TGA, but the other three performed worst at 0.067. For IP, identical results were observed: all but TGA favoured 0.013 L/min. The worst flow rate for IP was 0.013 L/min according to TGA, 0.34 L/min for GD and Avg PD (although N = 1), and 0.067 L/min for Raman.

When specific runs are compared, 0.067 L/min produced the lowest GD, Avg PD and Raman values for hematite across all temperatures. This was also true for IP at 950 °C, but at 850 °C, IP showed increasing carbon quality with decreasing flow rate across all metrics.

On average and relative to the control, TGA performed best at 0.013 L/min, and worst at 0.067 L/min. GD was highest at 0.067 L/min relative to the control, and lowest at 0.67 L/min. Avg PD was highest at 0.067 L/min and lowest at 0.013 L/min. Raman performed the best relative to the control at 0.067 L/min, and worst at 0.013 L/min.

Next, the overall control-relative mean was broken down by temperature and catalyst type. At 850 °C, TGA was highest relative to the control at 0.67 L/min. GD was negative at all flow rates, but was the best at 0.067 L/min. Avg PD and Raman were also most favourable at 0.067 L/min. At 900 °C, TGA was highest at 0.67 L/min, but the remaining metrics were all best relative to the control at 0.067 L/min (0.013 L/min was only sampled at 850 °C). The same trend was found at 950 °C, and for the means of runs using G and IP ironsand.

A brief summary of the effects of flow rate on carbon quality is given here:

- On average, TGA indicated that 0.067 L/min produced the highest quality carbon, while the other three metrics favoured 0.013 L/min.
- On average, the lowest quality carbon was produced at 0.013 L/min for TGA data, 0.034 L/min for GD, and 0.067 L/min for Avg PD and Raman.

- At 850 °C, 0.067 L/min was best for TGA, the other three metrics favoured 0.013 L/min.
- At 900 °C, 0.067 L/min had the highest carbon quality for TGA and GD, while 0.67 L/min was best for Avg PD and Raman (0.013 L/min was not measured).
- At 950 °C, 0.067 L/min had the highest carbon quality for TGA, while the other three metrics favoured 0.013 L/min.
- For IP and H, 0.067 L/min had the highest carbon quality for TGA, while 0.013 L/min was best for the other three metrics.
- For H, the lowest carbon quality was at 0.013 L/min for TGA, while the other three metrics were worst at 0.067 L/min.
- For IP, the lowest carbon quality was at 0.013 L/min for TGA, 0.34 L/min for GD and Avg PD (this had an N of only 2), and 0.067 L/min for Raman.
- Relative to the control, the largest positive value was at 0.067 L/min for all metrics except TGA, which was best at 0.013 L/min.
- Relative to the control, TGA was worst at 0.067 L/min, GD was worst at 0.67 L/min, and Avg PD and Raman were worst at 0.013 L/min.
- At all temperatures and for all catalyst types, TGA was best relative to the control at 0.67 L/min, while the other three metrics of carbon quality were best relative to the control at 0.067 L/min (0.013 L/min was not measured).

4.2.2.2 Discussion

It is clear that 0.013 L/min produced the highest quality carbon overall. However, there was no clear linear trend in the carbon quality data, meaning that higher flow rates did not necessarily produce carbon of the lowest quality. Interestingly, 0.067 L/min was the worst flow rate for hematite carbon quality across all temperatures, and for IP at 950 °C, but IP at 850 °C had 0.67

L/min as its worst flow rate.

One possible explanation for this is the longer duration of 0.067 L/min runs. Runs at this flow rate had an average duration of over 18.5 hours, compared with 8.3 hrs for 0.013 L/min and 4.3 hrs for 0.67 L/min. The reason this may be important is that if more amorphous forms of carbon were produced later in the run, this would artificially lower the observed carbon quality relative to the other flow rates. However, it is unknown whether the quality of carbon does in fact decrease with experimental runtime, and there is no other reason to suspect that it does. Amorphous carbon produced by secondary catalytic processes would continue depositing after the catalyst itself had deactivated, so superfluous runtime would have the effect of artificially reducing carbon quality measurements in this case. However, such processes only occur at high temperatures, and the 0.067 L/min minimum was observed for hematite even at 850 °C, where rates of carbon self-catalysis and methane pyrolysis are very low.

Alternatively, the differences in behaviour at different flow rates may be due to factors intrinsic to the TCMD reaction and catalyst composition themselves. The expected trend was that lower flow rates, and thus higher methane residence times, would better promote metal dusting and thus produce higher quantities of graphite flakes and carbon fibers. The fact that this was not observed for hematite at 0.067 L/min means that this specific residence time resulted in less graphitic carbon. The mechanism by which the rates of the TCMD reaction and the metal dusting process specifically affect carbon quality is not well understood. It is possible that at this flow rate, only partial metal dusting occurred for hematite, reducing the production of carbon fibers from single crystals of the catalyst, and increasing the relative proportion of encapsulating forms of carbon.

The reason why carbon quality was higher for hematite at 0.67 L/min is also uncertain. One possible explanation has to do with the reduction of the

catalyst. At high flow rates, the reduction of the catalyst was likely to be incomplete, because the catalyst was coated in carbon and deactivates too soon. This is supported by the lower conversion ratios and rapid deactivation times observed at 0.67 L/min. The reduction of the catalyst is known to improve carbon quality through the production of small quantities of water vapour, as discussed in Section 2.3. If this is the case, then once reduction was complete, the carbon quality would decrease. At 0.067 L/min, the overall carbon quality may have been lower because the reduction process went to completion, and subsequent carbon production was of a lower quality. At 0.67 L/min, of the small amount of carbon that was produced, a higher proportion was produced in conjunction with the reduction reaction, so proportionally more high quality carbon was produced.

Overall, 0.013 L/min was the optimum flow rate for carbon quality. It is clear however that the flow rate has different effects on hematite and IP carbon production.

4.2.3 Catalyst Composition and Particle Size Effects

For carbon characterisation data, at 0.67 L/min and 850 °C, the Glenbrook sand's TGA half-temp, graphitic degree, and average particle diameter were all slightly lower than the mean of all comparable IP runs (-3 °C, -0.03, and -7.9 nm respectively). Raman I_D/I_G ratio was lower (-0.035, less disordered) than IP. At 0.013 L/min and 850 °C, mean TGA for G was higher than for IP, GD and Avg PD means were lower, and mean Raman I_D/I_G ratio was higher. However, there were considerable differences in carbon characterisation values between replicates for runs at 0.013 L/min, as shown in Table 8. This means that, while the Glenbrook carbon appears on average to be less graphitic than the IP-produced carbon at 0.013 L/min, more replicates are needed to confirm this.

At 0.67 L/min and 850 °C, the carbon produced by unpurified Patea

ironsand (I) had lower TGA than G and IP, a higher GD, and a similar Avg PD (Raman not measured). At 0.67 L/min and 950 °C, the TGA value for I was higher than IP, but all other metrics showed that the carbon quality of I was lower than that of IP.

Absolute data means show only very small differences in carbon quality between the sieved, <100 μm IP sand and the normal IP sand for all metrics. The largest difference was a -0.10 improvement in Raman I_D/I_G ratio at the lower sand size. At 850 °C and 0.013 L/min, TGA half-temp was higher for the <100 μm sand, GD was slightly higher (0.02), Avg PD was lower, and Raman was higher (more disordered) than the normal IP. At 850 °C and 0.67 L/min, <100 μm IP had a lower TGA value, the same GD, almost the same Avg PD (+1.4 nm), and a similar Raman value (+0.025) when compared with the normal IP sand. There was a possibility of larger particle sizes producing higher amounts of graphite flakes by increasing the number of metal dusting cycles a given particle can sustain. However, these results suggest that at low flow rates, reducing the aggregate particle size was detrimental to the quality of carbon produced.

A brief summary of the effects of catalyst type and aggregate particle size on carbon quality is given here. Overall, IP produced carbon of a similar quality to G and a higher quality than I, and reducing the aggregate particle size did not help.

- At 850 °C and 0.013 L/min, <100 μm IP had higher TGA, slightly higher GD, lower Avg PD, and higher (more disordered) Raman values than normal IP.
- At 0.67 L/min and 850 °C, <100 μm IP had lower TGA than IP, while the other three metrics were similar to the IP values.
- At 0.67 L/min and 850 °C, G was worse than IP for all metrics of carbon quality except Raman, although the differences were only slight.
- At 0.013 L/min and 850 °C, G was worse than IP for all metrics except

TGA.

- For G runs, N = 3, and differences between duplicate values were high.
- At 0.67 L/min and 850 °C, carbon quality produced by I was worse than IP for TGA, better for GD, and the same for Avg PD (Raman not measured).
- At 0.67 L/min and 950 °C, I was worse than IP for all metrics except TGA.

4.3 Combined Effects

This section considers the combined effects of all variables and process conditions on the activity, decay, and lifetime of the ironsands catalyst, and the quality of the carbon it produced.

4.3.1 Absolute Conditions

This section summarises the conditions in which the ironsand produced the highest catalyst activity, longest lifetimes, and highest quality carbon. The discussion of these results is in Section 4.3.3.

The highest maximum conversion ratios were observed with purified Patea ironsand (IP) at 850 °C and 0.013 L/min, with a highest value of 80.1%. Glenbrook sand also had similarly high maximum conversion ratios. At this low flow rate, reducing the aggregate particle size was detrimental to the conversion ratio. The fact that the maximum conversion ratio was highest at low flow rates is intuitive, because the higher residence times of the CH_4 allowed a higher volume percentage of it to diffuse into contact with the iron catalyst. However, the fact that for IP, lower temperatures were favoured at low flow rates is not intuitive. Only a single run was carried out at 0.013 L/min and 950 °C, but higher conversion ratios were also observed for IP at lower temperatures in the 0.067 L/min runs (averaged across 2 runs per

temperature). The hematite control did not follow this trend at 0.067 L/min, instead showing max conversion ratios that were highest at 950 °C.

The single highest carbon yield per unit of catalyst and per weight of iron was produced with IP at 950 °C and 0.067 L/min, with 11.9 g_C/g_{Fe} (18.5 hrs, complete deactivation). This was in contrast to the decrease in max conversion ratio seen at high temperatures. Reducing the aggregate particle size slightly reduced these yields. The single highest hematite yield was 6.4 g_C/g_{Fe}, under the same conditons.

The lowest t_{max} values signalled the quickest activation period and thus the shortest reduction time of the ironsand. This was the case at 950 °C and 0.67 L/min. This was expected, as the highest kinetics and concentrations of reductant (CH_4) were available at these conditions. There was some evidence that lowering the aggregate particle size resulted in lower t_{max} values.

The highest SCA_1 values were produced at 850 °C and 0.013 L/min. Reducing the aggregate particle size negatively affected the decay of the catalyst at this flow rate, so larger particles were preferred. Glenbrook ironsand was the catalyst type that decayed the slowest, but only by a very small margin (+3% SCA_1) that is likely to be insignificant relative to the measurement error.

The longest time to half-max occurred at 0.013 L/min, because many runs at that flow rate did not decay to half their maximum value within the duration of the experiment, and those that did decayed much slower than other flow rates. The temperature dependence of $t_{\frac{1}{2}max}-t_{max}$ varied widely with catalyst type and flow rate, and there was not enough data to confirm the optimum temperature for this metric.

TGA half-temperature values were highest at 950 °C and 0.067 L/min. At low flow rates, using G as the catalyst and reducing the aggregate particle size produced slightly higher TGA values.

On average, PXRD graphitic degree was highest at 950 °C and 0.013

L/min, with H as the catalyst. The ironsand that performed the best was IP. However the single highest GD values were from hematite runs at 850 °C, at two flow rates: 0.67 and 0.013 L/min.

PXRD Average Particle Size was also highest on average at 950 °C and 0.013 L/min, but IP had the highest values. Lowering the aggregate particle size did not increase the average particle size.

The Raman I_D/I_G ratio was lowest at 0.013 L/min. At this flow rate, 950 °C produced the carbon with the lowest disorder. IP was the best catalyst type.

Overall, the highest yields of carbon with the highest carbon quality were produced by IP at 950 °C and 0.013 L/min, with an unchanged aggregate particle size distribution.

4.3.2 Control-Relative Conditions

This section summarises the conditions under which the ironsand activity and lifetime was highest compared to the hematite control. This information is useful to better understand the differences in their behaviour under the same conditions. Possible reasons for the differences are discussed in Section 4.3.3.

The maximum conversion ratios of purified Patea and Glenbrook ironsand were higher than the control under almost all conditions. The magnitude of this difference was highest on average at 0.013 L/min. Temperature studies at this flow rate were not carried out, but the largest control-relative max conversion ratio value from another flow rate was at 850 °C and 0.067 L/min.

Carbon yield per weight of catalyst ($g_C/g_{catalyst}$) was highest relative to the control at 0.013 L/min and 950 °C, on average. It was lowest at 0.67 L/min and 850 °C. Carbon yield per weight of iron (g_C/g_{Fe}) was higher than the control under all conditions measured in this research. This relative difference was highest at 0.067 L/min and 950 °C.

The global mean of time to maximum conversion ratio (t_{max}) was lowest relative to the control at 850 °C and 0.013 L/min. Control-relative t_{max} was highest at 0.67 L/min. This was because of the differences in reduction rates between the control and the ironsand.

The decay of the catalyst from maximum to half maximum conversion ratio was faster relative to the control for most conditions. Runs with I and IP at 950 °C were the only ones that decayed to half-maximum more slowly than the control.

The SCA_1 of all types of ironsand was often lower than that of the control, indicating a shorter catalyst lifetime. However, at 950 °C and 0.013 L/min, ironsand SCA_1 values were, on average, largest relative to the control. 0.067 L/min and 900 °C had the worst control-relative SCA_1 values.

TGA half-temperature values were higher than the control in all but two cases, but were highest on average at 850 and 950 °C. Control-relative TGA half-temp was highest at 0.67 L/min for every temperature and ironsand type.

Mean PXRD Graphitic Degree was highest relative to the control at 900 °C and 950 °C, and 0.067 L/min.

Mean PXRD Avg Particle Diameter was highest relative to the control at 900 °C and 950 °C, and 0.067 L/min.

Mean Raman I_D/I_G ratio was lowest (least disordered) relative to the control at 900 °C and 950 °C, and 0.067 L/min.

4.3.3 Discussion of Optimal Conditions

Ironsand consistently produced higher carbon yields than hematite under almost all conditions, which is a positive indication of the viability of TCMD in New Zealand. The fact that the ironsand ($Fe_{3-x}Ti_xO_4$, $0 \leq x \leq 1$) and hematite (Fe_2O_3) had different oxidation states, and thus different weight percentages of iron, meant that the higher yields of carbon by catalyst weight

that ironsand produced became even higher when the weight percentage of iron was adjusted for. It was clear that ironsand catalytic activity and lifetime was significantly higher than the hematite.

The fact that the activity of ironsand was higher than hematite may be due to differences in their reduction times [30]. The reduction of hematite by methane within the experiment itself was shown to produce better conversion ratios than pre-reduction with hydrogen, as discussed in Section 2.3. This is thought to be due to synergy between the reduction process and the decomposition of methane. A longer reduction time would prolong this process for the ironsand, therefore increasing the activity of the iron above that observed for hematite.

The higher lifetime of ironsand may be due to differences in the stability of cementite formed within the catalyst particle. Cementite stability affects the rate of the carbide cycle, because it determines the rate of decomposition of cementite into graphite and ferrite. As discussed in Section 2.4, titanomagnetite has a higher cementite stability than hematite [31], and thus is likely to have a slower carbide cycle rate. This was initially expected to be detrimental, because it would slow the production of graphite layers by single crystals of iron. However, in a polycrystalline particle, a high stability of cementite appears to be beneficial to the promotion of metal dusting [10]. The more stable the cementite, the slower the rate of surface carbide deposition, which both slows the growth of the external graphite layer and maintains a higher carbon concentration gradient within the iron crystal. This promotes the diffusion of carbon deeper into the crystal. As discussed earlier, deep carbon diffusion leads to saturation of the entire iron crystal, internal graphite precipitation, and resultant metal dusting.

At 0.067 L/min, IP had carbon yields that were increasingly larger than those of hematite as the temperature was raised, despite IP showing a reduction in maximum conversion values. This suggests that increasing the

temperature extended the lifetime of the IP catalyst to a greater extent than it did the hematite. Because the increases in yield were substantially different, amorphous carbon from methane pyrolysis cannot be solely responsible for the increase in carbon yields at high temperatures. This supports the theory that the differences in composition of the two catalysts fundamentally affects their metal dusting behaviour.

In addition, mean control-relative carbon quality values differed with temperature, and were highest at 950 °C. As discussed in Section 4.2.1.2, this was in large part due to the differing trends of H and IP with temperature. The quality of carbon produced by hematite decreased at higher temperatures, while in several cases the opposite is true of IP. Both H and IP had substantially higher Raman I_D/I_G ratios at higher temperatures, but at 0.067 L/min, H showed a dramatic increase in disorder at 900 °C, while IP only showed a corresponding increase at 950 °C. This could be due to secondary catalysis of methane decomposition by the carbon formed earlier in the run. The activation energy and activity of such a process would be dependent on the morphology of carbon produced by the iron catalyst, so if hematite produced a morphology that was considerably more active than the morphology produced by ironsand, this could account for the difference in carbon disorder at 900 °C.

At 0.013 L/min, the decay of the catalyst was slowest and maximum conversion ratios were highest. The quality of carbon produced by IP was also highest at this flow rate. This was due to the promotion of metal dusting by higher methane residence times.

While unpurified ironsand showed the highest g_C/g_{Fe} at 0.67 L/min, its carbon quality was lower than IP. In future, it would be worth testing this sand at low flow rates to see what effects the high levels of impurities have.

Overall, the optimum conditions for use of New Zealand ironsands as a TCMD catalyst are 0.013 L/min, 950 °C, magnetically purified, and an

unchanged particle size distribution. Ironsand is unquestionably suitable for the TCMD process, as shown by its good performance relative to the hematite control. Ironsand's activity was in many cases higher than hematite's, its lifetime longer, and its yields higher. While the graphitic nature of the carbon produced by ironsands was sometimes lower than that produced by hematite, this was improved by raising the temperature.

4.4 Investigation Into Errors

4.4.1 Gas Chromatography Error

Gas chromatography measurements of exit stream gas samples provided all methane conversion ratio data in this research. As discussed in Section 3.2.1, the integrals of the CH_4 and H_2 peaks on the chromatogram were used to calculate the vol% of each gas in the sample, which were in turn used to calculate the methane conversion ratio.

It was expected that the vol% of CH_4 and H_2 would add to 100% for a given sample. However, in many experimental runs, this was not the case. Figure 31 shows the difference between the expected value of 100%, and the total vol% ($vol\%_{CH_4}$ + $vol\%_{H_2}$) for all runs at a given flow rate. Each data point on the graph represents the mean of all values at that time point in the experiment. For example, at 30 minutes from the beginning of the experiment, at 0.067 L/min, the total volume % of both gases was on average 15% lower than 100%. A high value represents a high error.

It is clear that as the flow rate decreases, the discrepancy increases between the vol% totals and the expected value of 100%. On average, runs at 0.013 L/min had a vol% error of 25.5, with a standard deviation of 26.7. At 0.067 L/min, the mean vol% error was 18.3, with a SD of 19.8. At 0.67 L/min, the mean vol% error was 2.4, with a SD of 1.4. These discrepancies are very large, particularly at low flow rates, and it is difficult to know to

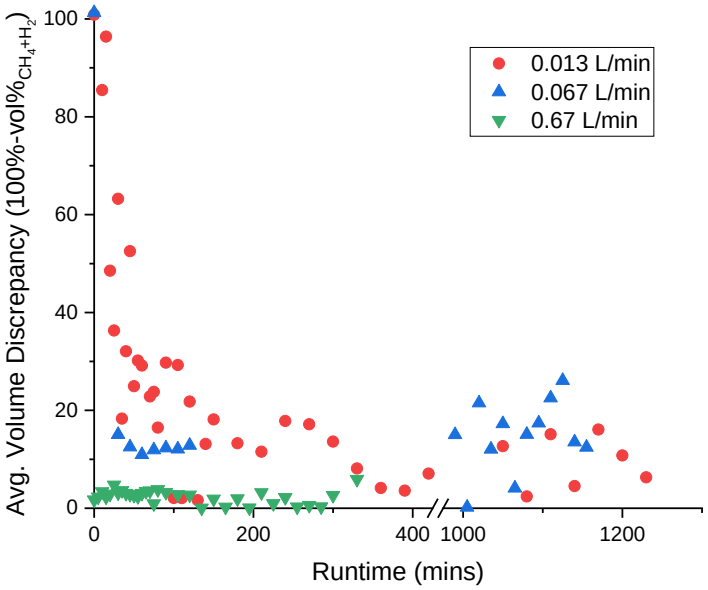

Figure 31: For runs of the same flow rate, the total CH_4 and H_2 vol% values were averaged across each time point. These values were then subtracted from the expected value of 100% to give the mean discrepancy at each time, by flow rate.

what extent they affected the conclusions drawn in this research.

There are several possible causes of the discrepancy between observed and expected total vol%. One possibility is that there was gas contamination in the sample. Some GC chromatograms showed signs of contamination, with the presence of additional peaks in the chromatogram. There were two peaks that most commonly appeared: air, and an unidentifiable negative peak. The air may have entered the syringe during transfer from the experimental setup to the GC instrument. Extensive measures were taken to remove air from within the experimental setup, including purging with argon for an hour before run start, and clearing the septum headspace with the syringe repeatedly before taking the first sample of a run, so it is unlikely that the air came from the sample itself. Either way, air peaks were present too infrequently to explain the observed discrepancies.

The negative peak occurred in every 0.013 L/min run, and in two 0.067 L/min runs. A negative peak from a thermal conductivity detector in this case means that the thermal conductivity of the contaminant was lower than the instrument carrier gas, in this case, nitrogen. It was always largest at the beginning of an experimental run, and always disappeared gradually until it was no longer present at 30 to 60 minutes into the run. As the negative peak disappeared, the intensities of both methane and hydrogen peaks increased. These things suggest that the contaminant was water vapour, CO_2, or CO produced from the reduction of the iron oxide with methane, at the beginning of the experiment. All of these gases have lower thermal conductivity than nitrogen, which is consistent with observations. This contamination was on two occasions observed afterwards as condensation on the interior of the sampling syringes. Water is known to interfere with the sensitivity of thermal conductivity detectors, so this is almost certainly the cause of some of the discrepancies.

The presence of contaminant gases explains the large vol% discrepancy in the first 30-60 minutes of 0.013 L/min runs, but it does not explain the remaining discrepancies shown on Figure 31. The second possibility is the the standard curves used to calculate the vol% of gas from the GC integrals were inaccurate due to a change in detector sensitivity. The original standard curve was run in April, and then several replicate standards were run 6 months later in November, once all other data collection was complete. These replicates showed that the sensitivity of the detector to H_2 had in fact decreased, as the peak area for pure H_2 was lower. This, and the process used to generate the standard curves, is discussed in Appendix A.1. The new, lower standard curve was then applied to all previously recorded data before it was presented in this section. However, this only improved the vol% totals by about 5%. This means that even accounting for the decrease in detector sensitivity, the vol% discrepancy persists.

Overall, the reason the volumes of CH_4 and H_2 did not add to 100% for so many runs is not properly understood. Gas contamination was present, but only in 0.013 L/min runs at early time values, so only explains a small segment of the problem. Gas contamination would always produce a peak in thermal conductivity detection unless the conductivity of the contaminant was the same as that of nitrogen. Any error due to loss of sensitivity in the detector would have been compensated for by rerunning the standards, so this does not help. Any problems with the GC column would have manifested differently and would have been easily identifiable as peak deformities. Manual loading of the GC from the syringe was protected from error by an automatic injection unit, which loaded a 1 mL aliquot of gas into the headspace of the column before each GC run. This meant that the volume of GC sample could not have affected the observed peaks. Running samples before the GC detector had stabilised (insufficient warm-up) would cause error at the beginning of the run, but this would disappear after about an hour. None of these things explain the observed discrepancies, particularly not the trend of increasing error with decreasing flow rate.

4.4.2 Replication Error

Table 8 lists all runs where duplicates were carried out, and the differences between them for key dependent variables used in this research. The mean and standard deviation of those differences are shown for each variable. Due to the time constraints of the project, replicates of only ten runs were performed. This number is insufficient to allow robust conclusions to be drawn from the data generated in this research. The duplicates of complete deactivation runs at 0.067 L/min were prioritised, as they provided the best indication of the total carbon and hydrogen yields the catalyst could produce.

With limited replicates, it is difficult to create an estimate of confidence that can be applied widely to the results of this research, especially given the

Table 8: Absolute differences between replicate runs. Missing values are due to missing values from either half of the duplicate (see Table 5). A: Max Conversion Ratio (%); B: t_{max} (min); C: SCA_1(%); D: $t_{\frac{1}{2}max} - t_{max}$ (min); E: Mass carbon (g); F: TGA Half-temp; G: PXRD Graphitic Degree; H: PXRD Avg Particle Size (nm); I: Raman I_D/I_G Ratio. Carbon yield is not included because it is derived from the mass of carbon. *Three experiments were run under these conditions, producing two difference rows here.

Table 8: Duplicate Differences														
Catalyst Type	Tube Type	Temp. (°C)	t_{total} (hrs)	Flow (L/min)	Size (nm)	A	B	C	D	E	F	G	H	I
G	Q	850	5	0.013	Normal	5.8	30	4.1		0.01	6.8	0.000	5.3	0.166
IP	Q	850	5	0.013	<100 μm	12.2	30	15.2		0.09	8.1	0.043	0.3	0.219
H	Q	850	18.5	0.067	Normal	4.0	45			0.18	2.8	0.044	5.0	0.130
IP*	Q	850	18.5	0.067	Normal					0.04	0.9	0.102	44.4	0.003
IP*	Q	850	18.5	0.067	Normal	7.4	0	14.1		0.47	3.5	0.087	38.8	0.002
H	Q	900	19	0.067	Normal	16.8	15	14.2		0.07	25.8	0.515	48.2	0.267
IP	Q	900	18.5	0.067	Normal	30.7	0	39.4		2.07	7.2	0.073	30.6	0.045
H	Q	950	18.5	0.067	Normal	5.7	0	5.0	0	2.58	10.9	0.000	4.3	0.086
IP	Q	950	18.5	0.067	Normal	6.2	0	17.5	45	0.96	1.0	0.044	27.9	0.037
I	S	950	4	0.67	Normal	6.4	5	25.3	30	0.16				
					Standard Deviation:	8.0	16.1	10.6	18.7	0.9	7.2	0.150	18.0	0.090
					Mean:	10.6	13.9	16.9	25.0	0.7	7.4	0.101	22.8	0.106
					N:	9	9	8	3	10	9	9	9	9

unquantified gas chromatography error discussed in the previous section. In some cases, the difference between duplicates was very large. For example, the IPQ900_0.067 pair of runs had a 30.7% difference in maximum conversion ratio, where the max conversion ratio of the smaller run in the pair was 29.08%, and the higher run was 59.74%. However, the GC vol% total at max conversion for the smaller run was only 65%, while for the larger run it was 92%. This may be an example of an outlier created by GC measurement error.

To test the effects of the GC vol% total error on the agreement between duplicate max conversion ratio values, the CH_4 and H_2 integrals of each duplicate run's max conversion ratio value were corrected using the following formula:

$$\text{Corrected Peak Integral} = \frac{\text{GC Peak Integral}}{vol\%_{\text{CH}_4+\text{H}_2} \cdot 0.01}$$

This scaled the integral values so the the vol% of the two gases added to 100%. In eight out of nine cases, this improved the agreement between the max conversion ratio values of duplicate runs, while the remaining case showed a greater difference between duplicates. The mean error in max conversion ratio decreased from 10.6% to 6.9%. The validity of this scaling is uncertain, but it suggests that the GC error affected the data in a consistent way.

Another factor that may have affected max conversion ratio error is sample rates. Because sampling was done manually, the frequency of samples was between 5 and 30 minutes, depending on the type of run. Because the key purpose of the 0.067 L/min runs was on full deactivation carbon yields, sampling intervals were lower at the beginning of the run. This means that if the maximum conversion ratio occurred at different times in a pair of replicates, the observed value of that maximum may sometimes have been lower. The sampling interval also limited the precision of t_{max}.

The magnitude of differences in SCA_1 between duplicates was often tied to the error in max conversion ratio, and so the factors affecting that variable also affected this one. For example, the large difference in SCA_1 for the IPQ900_0.067 duplicates was caused by a correspondingly large difference in max conversion ratio. However, the large SCA_1 difference in the I950_0.067 runs was caused by one run having a sampling interval of 5 minutes, and the other 15 minutes. It should be noted that for all other duplicate pairs, the sampling interval was the same for both runs.

Out of all variables, the mass of carbon produced was the least susceptible to external sources of error, as the carbon was simply weighed at the end of the run. Two pairs of duplicates had differences in carbon mass greater than 2 g, which in each case was almost a third of the total carbon produced by these runs. When these runs were excluded, the mean difference in carbon mass between duplicates dropped from 0.7 g to 0.3 g.

Possible causes of replication error for the mass of carbon are few. The initial mass of catalyst was always 1.85 g, correct to two decimal places. The loading of the catalyst may not have placed the catalyst powder exactly in the centre of the reaction zone. Mass transfer issues within the catalyst bed may have restricted the flow of methane in some cases. The methane flow rate might have been slightly off, although this was checked when each sample was taken. The temperature of the reaction zone stabilised during the argon purging period, so was the same between experiments within $\pm 2°C$. None of these things could have caused a 30% difference in carbon production between duplicates.

Duplicate differences in TGA half-temperature, graphitic degree, average particle size, and Raman I_D/I_G ratio were on average 6%, 15%, 17%, and 9% of their respective observed value ranges. This was calculated using the

following formula:

$$\% \text{ of range} = \left(\frac{Max - Min}{\text{Mean duplicate difference}} \right) \cdot 100$$

These percentages provides an indication of how the values displayed in Table 8 relate to the range of possible values. Each characterisation technique has its own inherent sources of error which are considered in the descriptions of each technique found in Section 3.2.3.

In future work, there are several things that could be changed to reduce error. A dedicated gas chromatograph connected to the exit gas stream of the experimental setup would have been hugely beneficial, (although expensive), as it would have eliminated all manual sampling, and thus higher sampling intervals and overnight sampling for complete deactivation runs would have been possible. A mass-metering automatic flow controller would also increase confidence in the results. However, even simply running additional replicates would be extremely beneficial to this research.

5 Conclusion

This research investigated the effects of temperature, flow rate, catalyst composition, and aggregate particle size on the performance of New Zealand ironsands as a catalyst for thermo-catalytic methane decomposition.

It was found that purified Patea ironsands (IP) had higher carbon and hydrogen yields per weight of catalyst than the hematite control under almost all conditions, and higher yields per weight of elemental iron (ferrite) than hematite under all conditions. These yields were highest for purified ironsand at low flow rates and high temperatures. The single highest yield of carbon per weight of iron was 11.9 g_C/g_{Fe} obtained at 0.067 L/min and 950 °C after 18.5 hours. The single highest yield for hematite was 6.4 g_C/g_{Fe}, obtained under the same conditions.

The higher carbon yields of ironsand were a result of increased catalytic activity and lifetime. Gas chromatography measurements showed that the highest conversion of methane to hydrogen occurred at low flow rates, due to the increased CH_4 residence times. The single highest conversion ratio was 80.1% at 0.013 L/min and 850 °C. Ironsand maximum conversion ratios were higher than those of hematite under almost all conditions, and particularly in the early stages of an experimental run. This higher activity at the beginning of an experiment was thought to be due to slower ironsand reduction times causing the production of less encapsulating forms of carbon. The difference in lifetime and therefore overall carbon yield was attributed to the presence of titanium in the sand stabilising the cementite phase and promoting metal dusting.

Increasing the temperature from 850 to 950 °C was found to improve the carbon and hydrogen yields of the ironsand significantly more than it improved the yields of hematite. This supported the finding that differences in the composition of the two catalysts fundamentally affected their metal

dusting behaviour, although the reason for this is not fully understood.

The graphitisation of the carbon produced by reactions with each catalyst was was highest for both catalysts at 0.013 L/min. It was highest for hematite at 850 °C, but highest for ironsand at 950 °C. A possible explanation for this is that at higher temperatures, the reaction produced carbon that itself acted as a catalyst for further methane decomposition. If this process occurred more for hematite than ironsands, and the carbon produced by this secondary process was less graphitic, it would explain the observed data, although a specific investigation is needed to empirically confirm this. Once again, it is clear that the different composition of the ironsand significantly affected its behaviour with changing temperature.

Reducing the aggregate particle size was shown to be ineffectual at improving catalyst activity or carbon quality, and in some cases it had a negative effect. Glenbrook ironsand showed similar catalytic activity and had similar carbon yields to the purified Patea ironsand, suggesting that sand from different locations in New Zealand would behave equivalently in a commercial process. Unpurified Patea ironsand (50% iron oxide) in some cases had higher carbon yields per weight of iron than the other catalysts, but it produced poorly graphitic carbon.

Overall, this research found that the use of New Zealand ironsands as a catalyst for TCMD is not only equivalent to the hematite control, but had higher carbon yields and catalytic activity under almost all measured conditions, and produced more graphitic carbon at high temperatures. Low flow rates, high temperatures, and standard particle sizes were favoured.

In future work, more replicate runs of the experiments carried out in this research, along with the elimination of GC error and baseline conversion problems, would be required if the data in this research is to be used to draw stronger or more specific conclusions. In addition, there are several investigations of varying size that would complement the results of this re-

search. Firstly, performing XRD studies of how the titanomagnetite structure changes with temperature would be beneficial to understanding the effects of ironsand cementite stability on metal dusting. Secondly, additional runs of unpurified ironsand at low flow rates would provide more insight into the effects of impurities on carbon quality and catalytic activity. Thirdly, further investigation into the poor correlation of TGA data with other metrics of carbon quality would be useful. And lastly: A study of the metal dusting behaviour of ironsand under pressure was originally within the scope of this project, but was removed due to time limitations. It would be beneficial to conduct this if there is continued interest in the commercial prospects of this process.

References

[1] A. Abánades, C. Rubbia, and D. Salmieri. "Technological challenges for industrial development of hydrogen production based on methane cracking". In: *Energy*. Energy and Exergy Modelling of Advance Energy Systems 46.1 (Oct. 1, 2012), pp. 359–363. ISSN: 0360-5442. DOI: 10.1016/j.energy.2012.08.015.

[2] A. Abánades et al. "Experimental analysis of direct thermal methane cracking". In: *International Journal of Hydrogen Energy*. 3rd Iranian Fuel Cell Seminar 36.20 (Oct. 1, 2011), pp. 12877–12886. ISSN: 0360-3199. DOI: 10.1016/j.ijhydene.2011.07.081.

[3] Hazzim F. Abbas and W. M. A. Wan Daud. "Hydrogen production by methane decomposition: A review". In: *International Journal of Hydrogen Energy* 35.3 (Feb. 1, 2010), pp. 1160–1190. ISSN: 0360-3199. DOI: 10.1016/j.ijhydene.2009.11.036.

[4] von Anders Ödahl. *Sweden to ban sales of fossil-fuel powered cars by 2030*. electrive.com. Jan. 22, 2019. URL: https://www.electrive.com/2019/01/22/sweden-joins-nations-dropping-combustion-engines-target-2030/ (visited on 02/13/2019).

[5] Carole E. Baddour, D. Chester Upham, and Jean-Luc Meunier. "Direct and repetitive growth cycles of carbon nanotubes on stainless steel particles by chemical vapor deposition in a fluidized bed". In: *Carbon* 48.9 (Aug. 1, 2010), pp. 2652–2656. ISSN: 0008-6223. DOI: 10.1016/j.carbon.2010.03.031.

[6] Zongqing Bai et al. "Methane decomposition over Ni loaded activated carbon for hydrogen production and the formation of filamentous carbon". In: *International Journal of Hydrogen Energy* 32.1 (Jan. 1, 2007), pp. 32–37. ISSN: 0360-3199. DOI: 10.1016/j.ijhydene.2006.06.030.

[7] Ch N. Barnakov et al. "XRD Characterization of the Structure of Graphites and Carbon Materials Obtained by the Low-Temperature Graphitization of Coal Tar Pitch". In: *Eurasian Chemico-Technological Journal* 17.2 (Mar. 11, 2015), pp. 87–93. ISSN: 2522-4867. DOI: 10.18321/ectj198.

[8] R. H. Brownlee and R. H. Uhlinger. "Process for the manufacture of hydrogen and carbon black." Pat. Aug. 20, 1918.

[9] Wei-Hsin Chen and Shih-Cheng Lin. "Characterization of catalytic partial oxidation of methane with carbon dioxide utilization and excess enthalpy recovery". In: *Applied Energy* 162 (Jan. 15, 2016), pp. 1141–1152. ISSN: 0306-2619. DOI: 10.1016/j.apenergy.2015.01.056.

[10] C. M. Chun, J. D. Mumford, and T. A. Ramanarayanan. "Mechanisms of Metal Dusting Corrosion of Iron". In: *Journal of The Electrochemical Society* 149.7 (July 1, 2002), B348–B355. ISSN: 0013-4651, 1945-7111. DOI: 10.1149/1.1483099.

[11] Climate Action Tracker. *New Zealand*. Dec. 4, 2018. URL: https://climateactiontracker.org/countries/new-zealand/ (visited on 03/06/2019).

[12] Concept Consulting Group. *Long term gas supply and demand scenarios – 2019 update*. Sept. 16, 2019.

[13] Andrew Cornejo. "The thermo-catalytic decomposition of methane for economical and emission-free hydrogen production". PhD thesis. University of Western Australia, 2013.

[14] Andrew Cornejo et al. "Generating Hydrogen Gas from Methane with Carbon Captured as Pure Spheroidal Nanomaterials". In: *Chemistry - A European Journal* 17.33 (Aug. 8, 2011), pp. 9188–9192. ISSN: 09476539. DOI: 10.1002/chem.201100532.

[15] David Brennan. *Hazer Group Ltd (HZR): Path to commercialising technology in place*. State One Stockbroking, Nov. 17, 2017.

[16] A. Domínguez et al. "Microwave-assisted catalytic decomposition of methane over activated carbon for CO2-free hydrogen production". In: *International Journal of Hydrogen Energy* 32.18 (Dec. 1, 2007), pp. 4792–4799. ISSN: 0360-3199. DOI: 10.1016/j.ijhydene.2007.07.041.

[17] P. P. Edwards et al. "Hydrogen and fuel cells: Towards a sustainable energy future". In: *Energy Policy*. Foresight Sustainable Energy Management and the Built Environment Project 36.12 (Dec. 1, 2008), pp. 4356–4362. ISSN: 0301-4215. DOI: 10.1016/j.enpol.2008.09.036.

[18] W. H. Bragg F. R. S. Cavendish. "The structure of the spinel group of crystals". In: *The London, Edinburgh, and Dublin Philosophical Magazine and Journal of Science* 30.176 (Aug. 1, 1915). Publisher: Taylor & Francis _eprint: https://doi.org/10.1080/14786440808635400, pp. 305–315. ISSN: 1941-5982. DOI: 10.1080/14786440808635400.

[19] H. J. Grabke. "Metal dusting". In: *Materials and Corrosion* 54.10 (2003), pp. 736–746. ISSN: 1521-4176. DOI: 10.1002/maco.200303729.

[20] H21. *H21 Leeds City Gate Project*. July 2016.

[21] Niina Halonen et al. "Controlled CCVD Synthesis of Robust Multiwalled Carbon Nanotube Films". In: *The Journal of Physical Chemistry C* 112.17 (May 1, 2008), pp. 6723–6728. ISSN: 1932-7447. DOI: 10.1021/jp7110617.

[22] D. Harbec et al. "A parametric study of carbon nanotubes production from tetrachloroethylene using a supersonic thermal plasma jet". In: *Carbon* 45.10 (Sept. 1, 2007), pp. 2054–2064. ISSN: 0008-6223. DOI: 10.1016/j.carbon.2007.05.025.

[23] *Hazer Group technology could position it to enter global industrial hydrogen market*. Proactiveinvestors UK. Feb. 28, 2018. URL: http://www.proactiveinvestors.com.au/companies/news/192304/hazer-group-technology-could-position-it-to-enter-global-industrial-hydrogen-market-192304.html (visited on 03/10/2018).

[24] HazerGroup. *Preliminary Conceptual Modelling & Economic Analysis of the Hazer Process*. Feb. 28, 2018.

[25] Stephan Hofmann et al. "In situ Observations of Catalyst Dynamics during Surface-Bound Carbon Nanotube Nucleation". In: *Nano Letters* 7.3 (Mar. 1, 2007), pp. 602–608. ISSN: 1530-6984. DOI: 10.1021/nl0624824.

[26] Intergovernmental Panel of Climate Change. *Global Warming of 1.5 ^{o}C*. 2018.

[27] Muhammet Kayfeci, Ali Keçebaş, and Mutlucan Bayat. "Chapter 3 - Hydrogen production". In: *Solar Hydrogen Production*. Ed. by Francesco Calise et al. Academic Press, Jan. 1, 2019, pp. 45–83. ISBN: 978-0-12-814853-2. DOI: 10.1016/B978-0-12-814853-2.00003-5.

[28] Yongdan Li, Jiuling Chen, and Liu Chang. "Catalytic growth of carbon fibers from methane on a nickel-alumina composite catalyst prepared from Feitknecht compound precursor". In: *Applied Catalysis A: General* 163.1 (Dec. 1997), pp. 45–57. ISSN: 0926860X. DOI: 10.1016/S0926-860X(97)00116-6.

[29] Yongdan Li, Douxing Li, and Gaowei Wang. "Methane decomposition to COx-free hydrogen and nano-carbon material on group 8–10 base metal catalysts: A review". In: *Catalysis Today*. Methane decomposition to COx-free hydrogen and nano-carbon material on group 8-10 base metal catalysts: A review 162.1 (Mar. 29, 2011), pp. 1–48. ISSN: 0920-5861. DOI: 10.1016/j.cattod.2010.12.042.

[30] Raymond James Longbottom, Oleg Ostrovski, and Eungyeul Park. "Formation of cementite from titanomagnetite ore". In: *ISIJ international* 46.5 (2006), pp. 641–646.

[31] Raymond James Longbottom et al. "Stability of cementite formed from hematite and titanomagnetite ore". In: *Metallurgical and Materials Transactions B* 38.2 (2007), pp. 175–184.

[32] L. M. Malard et al. "Raman spectroscopy in graphene". In: *Physics Reports* 473.5 (Apr. 1, 2009), pp. 51–87. ISSN: 0370-1573. DOI: 10.1016/j.physrep.2009.02.003.

[33] J. P. Martins and F. Margarido. "The cracking shrinking model for solid-fluid reactions". In: *Materials Chemistry and Physics* 44.2 (May 1, 1996), pp. 156–169. ISSN: 0254-0584. DOI: 10.1016/0254-0584(95)01670-P.

[34] Ministry for the Environment. *National GHG Inventory Report 1990-2016*. ME 1351. Ministry for the Environment, Apr. 12, 2018.

[35] Ministry of Business, Innovation and Employment. *A Vision for Hydrogen in New Zealand*. Sept. 2019.

[36] Ministry of Transport. *Annual Fleet Statistics 2017*. 2017.

[37] R. Moliner et al. "Thermocatalytic decomposition of methane over activated carbons: influence of textural properties and surface chemistry". In: *International Journal of Hydrogen Energy* 30.3 (Mar. 1, 2005), pp. 293–300. ISSN: 0360-3199. DOI: 10.1016/j.ijhydene.2004.03.035.

[38] B.M. Moskowitz, M. Jackson, and V. Chandler. "Geophysical Properties of the Near-Surface Earth: Magnetic Properties". In: *Treatise on Geophysics*. Elsevier, 2015, pp. 139–174. ISBN: 978-0-444-53803-1. DOI: 10.1016/B978-0-444-53802-4.00191-3.

[39] N. Z. Muradov and T. N. Veziroğlu. "From hydrocarbon to hydrogen–carbon to hydrogen economy". In: *International Journal of Hydrogen Energy* 30.3 (Mar. 1, 2005), pp. 225–237. ISSN: 0360-3199. DOI: 10.1016/j.ijhydene.2004.03.033.

[40] Nazim Muradov. "Hydrogen via methane decomposition: an application for decarbonization of fossil fuels". In: *International Journal of Hydrogen Energy* 26.11 (Nov. 1, 2001), pp. 1165–1175. ISSN: 0360-3199. DOI: 10.1016/S0360-3199(01)00073-8.

[41] Nazim Muradov. "Thermocatalytic CO2-Free Production of Hydrogen from Hydrocarbon Fuels". In: *Proceedings of the 2000 Hydrogen Program Review*. 2000, pp. 570–28890.

[42] Nazim Muradov, Franklyn Smith, and Ali T-Raissi. "Catalytic activity of carbons for methane decomposition reaction". In: *Catalysis Today*. 1st International Symposium on Carbon for Catalysis "CARBOCAT-1" 102-103 (May 15, 2005), pp. 225–233. ISSN: 0920-5861. DOI: 10.1016/j.cattod.2005.02.018.

[43] Nazim Muradov et al. "Autothermal catalytic pyrolysis of methane as a new route to hydrogen production with reduced CO2 emissions". In: *Catalysis Today*. 2nd European Hydrogen Energy Conference 116.3 (Aug. 15, 2006), pp. 281–288. ISSN: 0920-5861. DOI: 10.1016/j.cattod.2006.05.070.

[44] Pavlos Nikolaidis and Andreas Poullikkas. "A comparative overview of hydrogen production processes". In: *Renewable and Sustainable Energy Reviews* 67 (Jan. 1, 2017), pp. 597–611. ISSN: 1364-0321. DOI: 10.1016/j.rser.2016.09.044.

[45] NZ Steel. *The Mining Operation*. URL: https://www.nzsteel.co.nz/sustainability/the-mining-operation/ (visited on 11/05/2018).

[46] Office of Transportation and Air Quality and US Environmental Protection Agency. *Greenhouse Gas Emissions from a Typical Passenger Vehicle*. Overviews and Factsheets. Mar. 2018.

[47] Hitoshi Ogihara et al. "Formation of highly concentrated hydrogen through methane decomposition over Pd-based alloy catalysts". In: *Journal of Catalysis* 238.2 (Mar. 10, 2006), pp. 353–360. ISSN: 0021-9517. DOI: 10.1016/j.jcat.2005.12.024.

[48] J. Y. Park and Octave Levenspiel. "The crackling core model for the reaction of solid particles". In: *Chemical Engineering Science* 30.10 (Oct. 1, 1975), pp. 1207–1214. ISSN: 0009-2509. DOI: 10.1016/0009-2509(75)85041-X.

[49] A. L. Patterson. "The Scherrer Formula for X-Ray Particle Size Determination". In: *Physical Review* 56.10 (Nov. 15, 1939), pp. 978–982. DOI: 10.1103/PhysRev.56.978.

[50] E. Pippel, J. Woltersdorf, and R. Schneider. "Micromechanisms of metal dusting on Fe-base and Ni-base alloys". In: *Materials and Corrosion* 49.5 (1998), pp. 309–316. ISSN: 1521-4176. DOI: 10.1002/(SICI)1521-4176(199805)49:5<309::AID-MACO309>3.0.CO;2-1.

[51] Sigit W. Prabowo et al. "Sticking-Free Reduction of Titanomagnetite Ironsand in a Fluidized Bed Reactor". In: *Metallurgical and Materials Transactions B* 50.4 (Aug. 2019), pp. 1729–1744. ISSN: 1073-5615, 1543-1916. DOI: 10.1007/s11663-019-01625-w.

[52] D Roy et al. "Characterisation of carbon nano-onions using Raman spectroscopy". In: *Chemical Physics Letters* 373.1 (May 13, 2003), pp. 52–56. ISSN: 0009-2614. DOI: 10.1016/S0009-2614(03)00523-2.

[53] J. -W. Snoeck, G. F. Froment, and M. Fowles. "Filamentous Carbon Formation and Gasification: Thermodynamics, Driving Force, Nucleation, and Steady-State Growth". In: *Journal of Catalysis* 169.1 (July 1, 1997), pp. 240–249. ISSN: 0021-9517. DOI: 10.1006/jcat.1997.1634.

[54] Stuff. "PGF boost for 'game changing' energy initiatives". In: *Stuff* (July 8, 2019).

[55] Stuff. "Prime Minister says offshore oil permit ban legislation offers 'complete certainty' to industry". In: *Stuff* (Oct. 29, 2018).

[56] Sakae Takenaka et al. "Formation of Carbon Nanofibers and Carbon Nanotubes through Methane Decomposition over Supported Cobalt Catalysts". In: *The Journal of Physical Chemistry B* 108.31 (Aug. 5, 2004), pp. 11464–11472. ISSN: 1520-6106. DOI: 10.1021/jp048827t.

[57] Tharun George. *Hazer Group independent testing validates technology*. Proactiveinvestors Australia. 2018. URL: https://www.proactiveinvestors.com.au/companies/news/205069/hazer-group-independent-testing-validates-technology-205069.html (visited on 11/02/2018).

[58] Trevor Hoey. *Hazer Group technology could position it to enter global industrial hydrogen market*. Proactiveinvestors UK. Feb. 28, 2018. URL: https://www.proactiveinvestors.com.au/companies/news/192304/hazer-group-technology-could-position-it-to-enter-global-industrial-hydrogen-market-192304.html. (visited on 11/02/2018).

[59] C. Y. Wen and S. C. Wang. "Thermal and diffusional effects in noncatalytic solid gas reactions". In: *Industrial & Engineering Chemistry* 62.8 (1970), pp. 30–51.

[60] Takeo Yamada et al. “Revealing the Secret of Water-Assisted Carbon Nanotube Synthesis by Microscopic Observation of the Interaction of Water on the Catalysts”. In: *Nano Letters* 8.12 (Dec. 10, 2008), pp. 4288–4292. ISSN: 1530-6984. DOI: 10.1021/nl801981m.

[61] R. T. Yang and J. P. Chen. “Mechanism of carbon filament growth on metal catalysts”. In: *Journal of Catalysis* 115.1 (Jan. 1, 1989), pp. 52–64. ISSN: 0021-9517. DOI: 10.1016/0021-9517(89)90006-7.

A Standards and Baselines

This appendix contains information on the standard curves used to calculate methane conversion ratios from gas chromatography data. It also describes the baselining process used to correct for the catalytic activity of the empty reaction tubes.

A.1 Standards

The standard curves for the gas chromatography measurements are shown in Figures 32 and 33. Syringes were filled with a mix of H_2 and CH_4 in the required volume ratio via septums on the gas cylinders. The injection head on the GC instrument took 1 mL aliquots of the gas mixture, so as long as the ratio of gases within the syringe was accurate, volume variation in the syringe or in manual injection could not have an affect. Standard curves were initially run in April, and then rerun in November. In November, the GC integral value at 100% H_2 was initially only 3483000 (averaged across two similar replicates), which was significantly lower than the maximum integral of 5182000 recorded in April. The November samples were rerun twice, and increased first to 4345000, and then to 4524000. It was realised afterwards that the GC instrument had not been given sufficient time to stabilise in the November sampling session, despite having warmed to the correct operating temperature. In April, the GC instrument was given more time to stabilise first ($\approx$ 30 mins).

However, even later in the November sampling session, when the GC had been running for $\approx$ 1 hour, the 100% H_2 value was still lower than the value recorded in April. An additional complication was presented by the fact that all CH_4 standard measurements taken in November, even the 100% CH_4 measurements, correlated well with those taken in April. As a result,

values from both April and November were used in the linear fit for the CH_4 standard curve. This means that the discrepancy in H_2 values cannot be explained entirely by a lack of GC warm-up period. Instead, it is likely that there was a problem with the thermal conductivity detector. It is possible that the detector was swamped by the high concentrations of analyte.

To remedy this, the detector needed to be baked at a high temperature for several hours. However, by the time this error was discovered, it was too late, as all experimental work was complete. It is difficult to quantify the effect this issue may have had on the experimental data prior to discovering the issue. As most of the experimental work in this research was performed closer to November than April, the November values were used for the H_2 standards. This was done so that the condition of the detector and the GC warm-up period of the standards was as closely matched to the experimental conditions as possible.

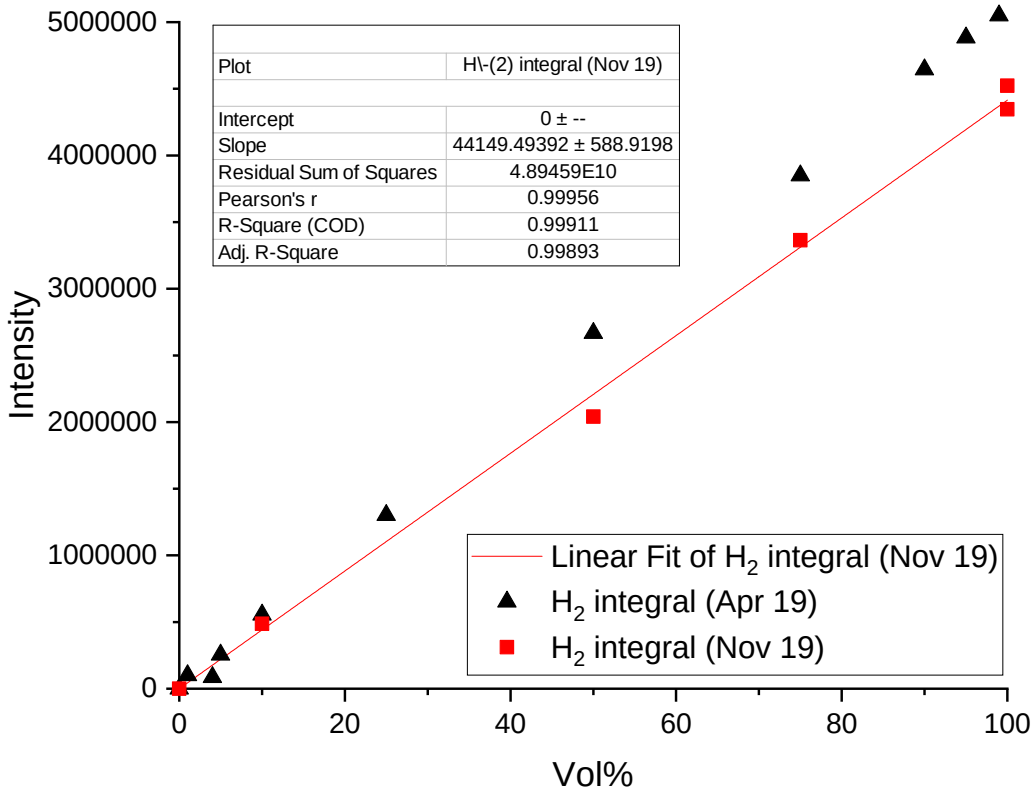

Figure 32: H_2 standard curve. Each value used in the linear fit is an average of two replicate runs performed in November 2019. The April standard curve did not agree with the two replicates run later in the year, so was not included in the final linear fit.

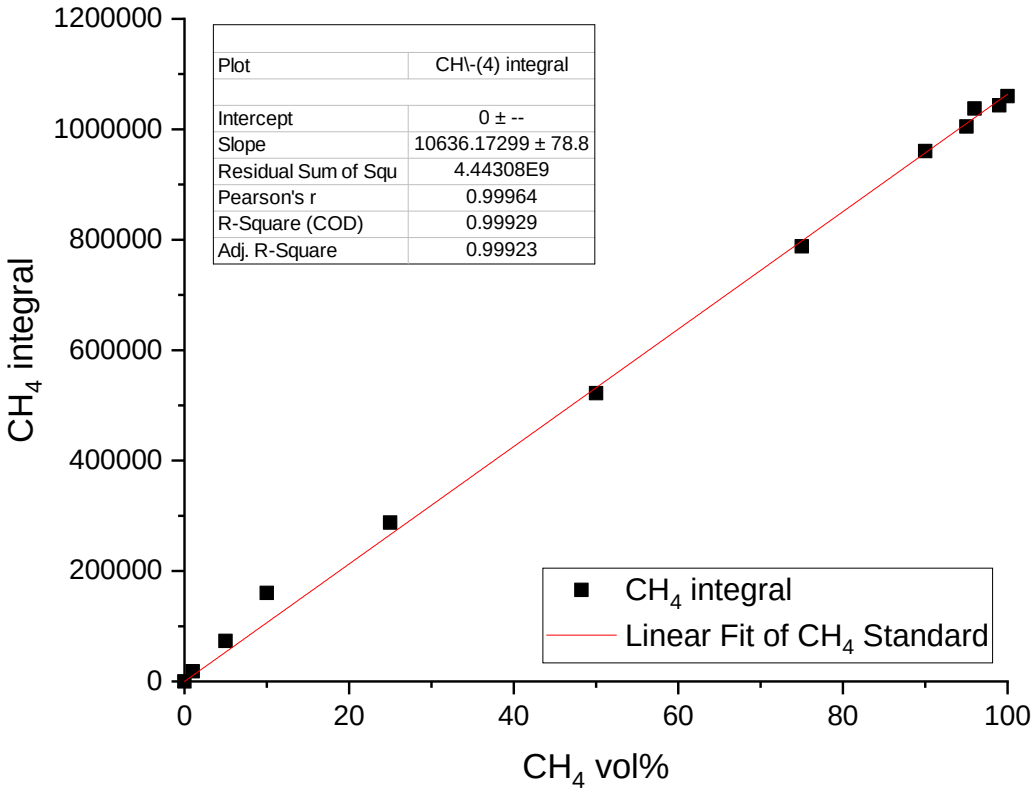

Figure 33: CH_4 standard curve. Each value is an average of one April value and two November values.

A.2 Baselines

Table 9 shows the methane conversion rates for the blank steel and quartz tubes at each temperature and flow rate. The relevant values are subtracted from the results of each experiment. Baselines for the steel tube included the thermocouple. All baseline conversion ratios are averaged across at least four values from at least two replicate runs. The quartz tube baseline value for 0.067 L/min at 950°C was unexpectedly high, but had a standard deviation of 1.8% across replicates. This high baseline was a problem, and had the potential to significantly affect the conclusions of this reserach. Un-

fortunately, it was not possible to use the less catalytically active stainless steel tube for high temperature, low flow rate runs, as the tightest seals for it did not cope well above 900 °C. Additionally, some carburisation of the outside of the stainless steel tube was observed after high temperature runs. In future work, a stainless steel tube with improved seals would be used to eliminate the high baseline and confirm the validity of the high temperature quartz tube data collected in this research, and the carburisation would be monitored.

Quartz tube baselines produced carbon in the form of a reflective foil coating the inside of the tube, despite the fact that quartz is not considered catalytically active for TCMD. When this foil was characterised, it was found to have poor graphitisation. High temperatures are known to cause non-catalytic pyrolysis of methane, which produces amorphous carbon. However, if this was responsible for the high conversion in the quartz tube, similar conversion ratios should have been observed in the steel tube as well, but they were not. It is possible that scratches or other defects in the quartz tube provided sites for the decomposition of methane. Once some carbon is present in the tube, it catalyses further decomposition, which may explain the high conversion ratios at high temperatures [13].

Foil was also obtained from several experimental runs, but was corrected for when calculating yields. The carbon foil was removed at the end of each run.

B Raw Data

This appendix provides examples of raw spectra from each type of analysis used in this research are displayed in this section, along with a summary table of raw results.

Table 9: Empty Tube Baseline Conversion Values			
Tube Type	Temperature (°C)	CH_4 Flow Rate (L/min)	Conversion (%)
S	800	0.67	0.13
S	850	0.013	8.29
S	850	0.67	0.22
S	900	0.67	0.70
S	950	0.67	2.08
Q	850	0.067	0.24
Q	850	0.013	4.64
Q	900	0.067	7.49
Q	950	0.067	23.74

Table 9: Empty tube baseline values, used to correct experimental data for the catalytic activity of the tube material. S refers to the stainless steel tube, Q refers to the quartz tube.

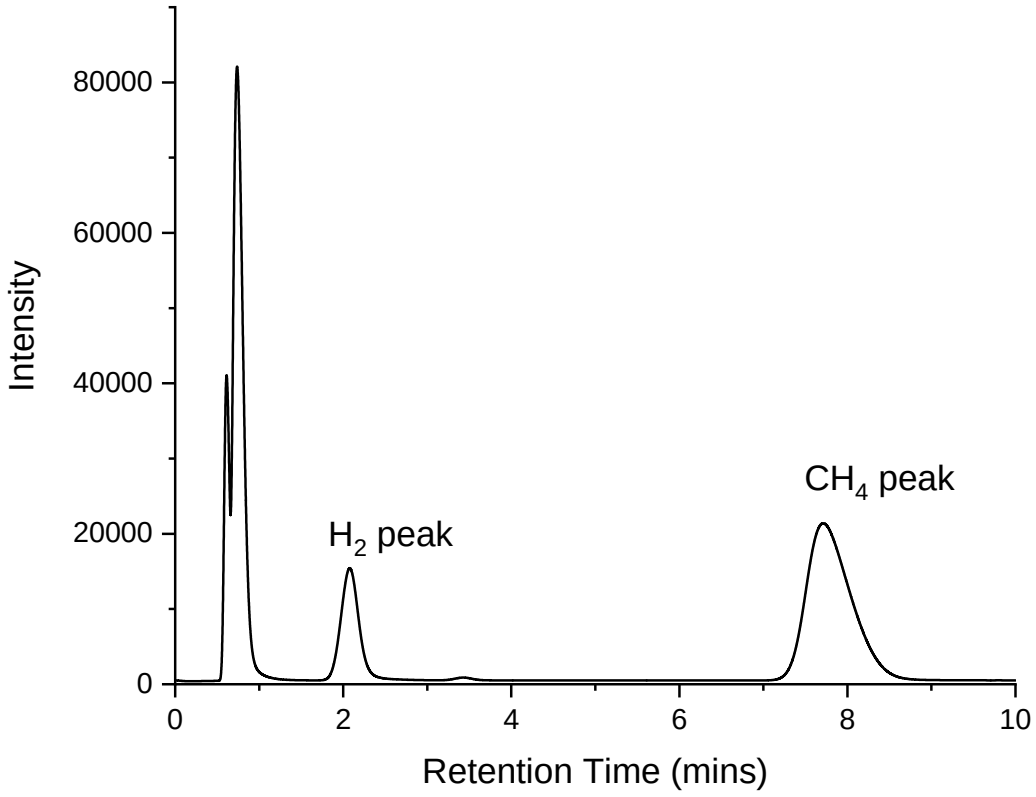

Figure 34: Example of a gas chromatogram obtained in this research. The integrals of the H_2 and CH_4 peaks were used to calculate the vol% of the gases in the sample. This spectrum is from the HQ850_0.067 run, sample 1.7.

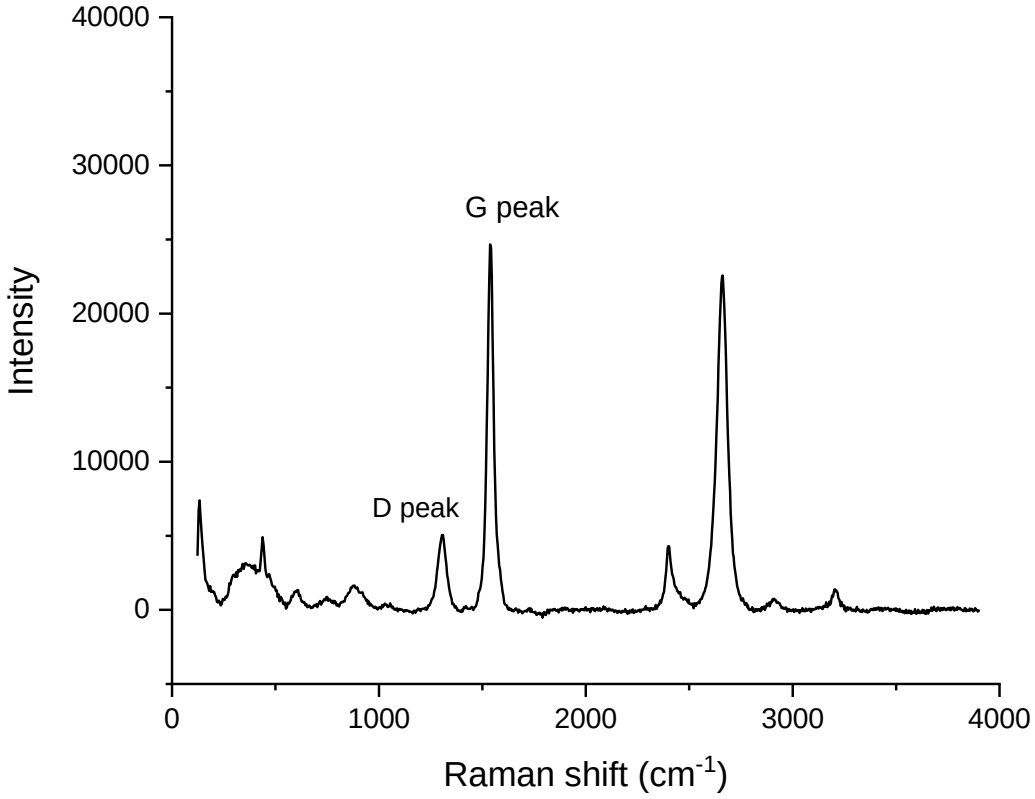

Figure 35: Example of a Raman spectrum obtained in this research. The ratio of the D and G peak intensities was used as a measure of carbon disorder. This spectrum is from the IPQ950_0.013 run. The peaks below 1000 cm^{-1} are due to scattering from the glass microscope slide.

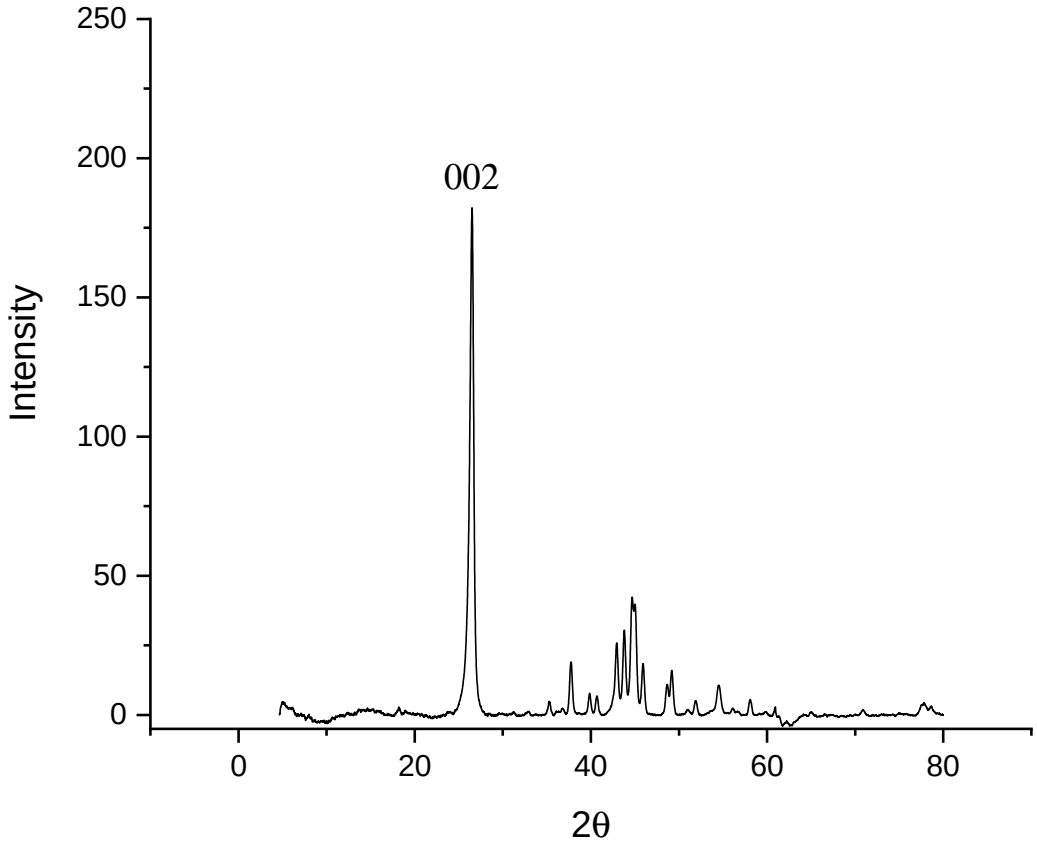

Figure 36: Example of a PXRD spectrum obtained in this research. The position of the graphite 002 peak was used to calculate the layer spacing of the graphite, while the FWHM of the 002 peak was used to calculate the Avg Particle Diameter. This spectrum is from the IPQ850_0.013_<100μm_2 run.

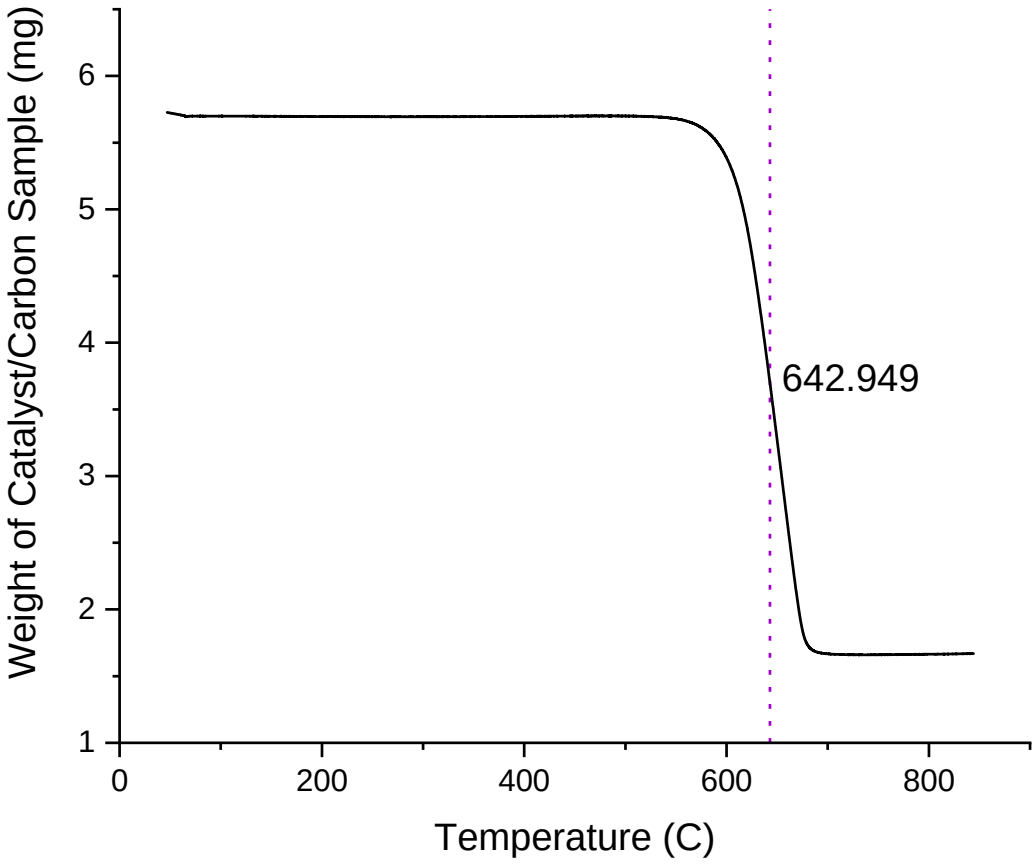

Figure 37: Example of a TGA spectrum obtained in this research. The temperature at which half the sample weight had burnt off was used as an indicator of carbon quality. This spectrum is from the HQ900_0.067_2 run. The temperature curve was a linear ramp at 10 °C/min.

C Methane Conversion Equation Validity

Two equations were used to calculate the percentage of methane converted to hydrogen from the vol% of methane and hydrogen in the exit gas stream.

The equations are as follows:

$$X_{CH_4} = \left(\frac{\%H_2}{200 - \%H_2} \right) \cdot 100$$

$$X_{CH_4} = \left(\frac{\frac{\%H_2}{2}}{\%CH_4 + \frac{\%H_2}{2}} \right) \cdot 100$$

Assuming that methane and hydrogen are the only two gases in the exit gas stream, these equations provide equivalent conversion ratios. This assumption is discussed in Section 4.4, but a mathematical proof is provided here.

Let the vol% of H_2 in the exit gas stream $\%H_2 = h$, and the vol% of CH_4 in the exit gas stream $\%CH_4 = x$. Setting the two equations equal to one another:

$$\frac{\frac{h}{2}}{x + \frac{h}{2}} = \frac{h}{200 - h}$$

$$\frac{h}{2}(200 - h) = h(x + \frac{h}{2})$$

$$\frac{100h - \frac{h^2}{2}}{h} = x + \frac{h}{2}$$

$$100 - \frac{h}{2} = x + \frac{h}{2}$$

$$100 - \frac{2h}{2} = x$$

$$x + h = 100$$

Every combination of x and h that sums to 100 is a valid solution under our assumption that the vol% of the two gases make up the entire exit gas stream.